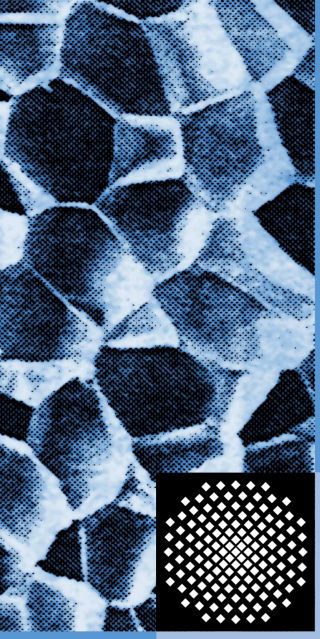

Universität Stuttgart
Germany

Institut für Mechanik (Bauwesen)
Lehrstuhl für Kontinuumsmechanik
Prof. Dr.-Ing. W. Ehlers

Growth, Modelling and Remodelling of Biological Tissue

Robert Friedrich Krause

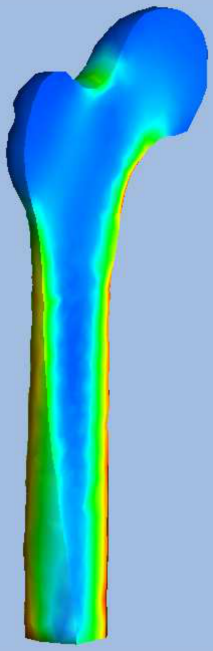

Report No.: II-29 (2014)

Growth, Modelling and Remodelling of Biological Tissue

Von der Fakultät Bau- und Umweltingenieurwissenschaften und
dem Stuttgart Research Centre for Simulation Technology
der Universität Stuttgart zur Erlangung der Würde
eines Doktor-Ingenieurs (Dr.-Ing.)
genehmigte Abhandlung

vorgelegt von

Dipl.-Ing. Robert Friedrich Krause

aus
Bietigheim-Bissingen

Hauptberichter:	Prof. Dr.-Ing. Wolfgang Ehlers
1. Mitberichter:	Prof. Dr.-Ing. Bernd Markert
2. Mitberichter:	Prof. Dr.-Ing. Tim Ricken

Tag der mündlichen Prüfung: 10. November 2014

Institut für Mechanik (Bauwesen) der Universität Stuttgart
Lehrstuhl für Kontinuumsmechanik
Prof. Dr.-Ing. W. Ehlers
2014

Report No. II-29
Institut für Mechanik (Bauwesen)
Lehrstuhl für Kontinuumsmechanik
Universität Stuttgart, Germany, 2014

Editor:
Prof. Dr.-Ing. W. Ehlers

© Robert Friedrich Krause
Institut für Mechanik (Bauwesen)
Lehrstuhl für Kontinuumsmechanik
Universität Stuttgart
Pfaffenwaldring 7
70569 Stuttgart, Germany

ISBN 978–3–937399–29–1
(D 93 - Dissertation, Universität Stuttgart)

Tradition ist Schlamperei
Gustav Mahler (1860–1911)

Danksagung

Neues zu entdecken und dabei das Bestehende nicht ungeprüft über Bord zu werfen, das ist der Kern der Wissenschaft. Um neue Lösungswege zu finden, müssen bestehende Lösungsansätze kritisch hinterfragt und ihre Grundlagen auf Basis der grundsätzlichen Prinzipien und Theoreme der modernen Wissenschaft überprüft werden. Wenn jedoch grundlegende Theorien und Vorgehensweisen neu entwickelt und überprüft werden, dann lässt sich auch der wissenschaftliche Erfolg nur noch begrenzt mit herkömmlichen Methoden überprüfen. Aus diesem Grund erfordert es auch immer Mut den herkömmlichen Weg zu verlassen, ohne dabei den eigenen Erfolg abschließend Bewerten zu können.

Durch die Einrichtung des SRC SimTech haben die Universität Stuttgart und alle Beteiligten diesen Mut bewiesen und sich auf das Terrain der interdisziplinären Forschung begeben. Wo früher einzelne Wissenschaftler die Grenzen ihrer Disziplinen immer weiter getrieben haben, arbeiten heute interdisziplinäre Forschungsteams an der Überschreitung dieser Grenzen. Dabei ist der Erfolg des Einzelnen auch immer der Erfolg des Teams und der Erfolg des Teams ist immer ach der Erfolg seiner Mitglieder. Es freut mich daher umso mehr, dass ich als Wissenschaftler zum Erfolg des Exzellenzclusters beitragen konnte, und damit auch selbst Teil seines Erfolgs sein durfte. Für diese Möglichkeit möchte ich mich bei meinen Betreuern Wolfgang Ehlers und Bernd Markert bedanken.

Gemeinsam mit Michael Reiter, Peter Reimann und Daniella Schittler konnten wir Biomechanik und System-Biologie ein Stückchen näher zusammen bringen. Für die konstruktive und interessante Zusammenarbeit bedanke ich mich bei allen Beteiligten.

Meinen Freunden und meiner Familie, insbesondere meiner Frau Margarita, danke ich für ihren Rückhalt und ihre Unterstützung während dieser Zeit.

Robert Krause

Stuttgart, November 2014

Contents

Deutsche Zusammenfassung

Es ist das Ziel dieser Arbeit, die Wachstums- und Strukturänderungsprozesse in biologischen Geweben im Rahmen der Kontinuumsbiomechanik möglichst genau abzubilden. Zur Beschreibung des Materialverhaltens wird ein zweiphasiges Kontinuumsmodell verwendet. Dabei repräsentiert die feste Phase Zellen und extrazelluläre Matrix, und die extrazellulären Flüssigkeiten werden in einer flüssigen Phase zusammengefasst. Darüber hinaus wird berücksichtigt, dass biologische Prozesse nur stattfinden, wenn die verantwortlichen Zellen ausreichend mit den für ihren Stoffwechsel notwendigen Nährstoffen versorgt sind. Um die gelösten Nährstoffe zu berücksichtigen, wird die Wachstumsenergie als eine gemittelte, nicht-mechanische Größe eingeführt, die die für den Zellstoffwechsel zur Verfügung stehende chemische Energie angibt. Durch dieses Konzept reduziert sich die Anzahl der zu berücksichtigenden Feldgrößen. Das ermöglicht eine vereinfachte Auswertung der Entropieungleichung. Gekoppelte drei-dimensionale Finite-Elemente-Simulationen von avaskulärem Tumorwachstum und durch Belastung verursachter Knochenumbau demonstrieren die Leistungsfähigkeit dieser Herangehensweise.

In zunehmendem Umfang werden die Methoden der Kontinuumsmechanik für die Modellierung von biologischen Geweben, wie Knochen, Knorpel oder Muskeln, verwendet. Dabei stellen insbesondere die nichtlinearen und anisotropen Eigenschaften sowie die durch Wachstum und Strukturumbau hervorgerufenen Veränderungen dieser Materialien eine Herausforderung dar. Allgemeine Übersichtsartikel über die Modellierung biologischer Gewebe werden durch Taber (1995) und Humphrey (2003) gegeben. In dieser Arbeit liegt der Fokus auf der Beschreibung biologischer Wachstumsprozesse. Dabei ist zu berücksichtigen, dass diese nicht nur die Form und Größe des wachsenden Gewebes verändern, sondern auch die innere Struktur und die damit zusammenhängenden Eigenschaften beeinflussen. Das makroskopische Verhalten eines Gewebes resultiert aus der Interaktion seiner Komponenten auf einer Mikroskala. In der Regel enthalten biologische Gewebe hauptsächlich Wasser, verschiedene Zellarten und eine extrazelluläre Matrix, (vgl. z. B. Cowin, 2000). Die relativen Anteile dieser Komponenten und ihre Eigenschaften werden durch Wachstumsprozesse beeinflusst. Diese können eine makroskopische Veränderung des Gewebes hervorrufen. Beispielsweise wird die Knochenmatrix ununterbrochen durch Knochenzellen auf- und abgebaut. Dabei passt sich die Struktur der Matrix an die lokale Belastungssituation an. Dies führt zu einer höheren Knochendichte in Regionen mit hohen Belastungen und verursacht den Abbau von unbelasteter Knochenmatrix, z. B. bei bettlägerigen Patienten oder längeren Aufenthalten in der Schwerelosigkeit. Diese Beobachtung, die auch Wolffsches Gesetz genannt wird, geht zurück auf Wolff (1892), der damit die Orthopädie begründete.

Obwohl biologische Materialien aus mehreren Phasen bestehen, verwenden einfache Modelle nur ein einphasiges Materialmodel. Die dabei verwendete Theorie der offenen Systeme geht zurück auf Cowin & Hegedus (1976), die damit die durch Spannung verursachten Strukturänderung von Knochen beschreiben. Dabei gehen sie davon aus, dass Einflüsse durch Fluide auf das mechanische Verhalten von Knochen vernachlässigbar sind und

dieses hauptsächlich durch die Eigenschaften der Knochenmatrix bestimmt ist. Ähnliche Arbeiten wurden von Beaupré *et al.* (1990), Weinans *et al.* (1994) und Lutz & Nackenhorst (2010) verfasst. Sie unterscheiden sich im wesentlichen in der Wahl der mechanischen Größe, die die Strukturänderung stimuliert. Das Hauptziel dieser Arbeiten ist die möglichst exakte Reproduktion der durch die Belastung verursachten drei-dimensionalen Dichteverteilung im Knochen und nicht die exakte Abbildung des Strukturänderungsprozesses selbst. Einen aktuellen Überblick über unterschiedliche Knochenmodell geben Mellon & Tanner (2012) und Webster & Müller (2011).

Auch andere wachsende biologische Gewebe lassen sich mit dieser Theorie beschreiben. Ambrosi & Mollica (2002, 2004) wenden sie bei Modellierung von Tumorspheroiden an. Dazu erweitern sie das einphasige Materialmodell um eine Nährstoffkonzentration, die den Wachstumsprozess steuert. Ein Überblick über unterschiedliche Tumormodelle geben Unnikrishnan *et al.* (2010). Ein mehrphasiges Modell, das auch die extrazellulären Fluide berücksichtigen, beschreiben Ricken & Bluhm (2009) für spannungsabhängige Umbausprozesse sowie Ambrosi & Preziosi (2002) und Byrne & Preziosi (2003) für avasculäre Tumore. Darüberhinaus führen Preziosi & Tosin (2009) ein dreiphasiges Modell ein, um gesundes Gewebe und Tumorgewebe zu beschreiben. Dabei berücksichtigen sie Zellen und Matrix als individuell Phasen.

Um die thermodynamische Konsistenz der Wachstums und Umbaualgorithmen zu gewährleisten, werden die Konstitutivgleichungen thermodynamisch ausgewertet. Im Rahmen der Theorie offener Systeme ermöglichen Kuhl & Steinmann (2003) die thermodynamische Auswertung, indem sie, zusätzlich zur Massenproduktion, Produktionsterme für Impuls, Energie und Entropie einführen. Diese müssen konstitutiv bestimmt werden. Ohne auf die biologischen Prozesse, die Wachstum und Umbau verursachen, einzugehen, fordern Steeb & Diebels (2003) die Gültigkeit ihrer für Erosion bestimmten thermodynamischen Einschränkungen auch in biologischen Geweben. Die thermodynamische Konsistenz ihres einphasigen Wachstumsmodells gewährleisten Ambrosi & Guillou (2007), indem sie eine zusätzliche Nährstoffgröße einführen, die durch den Wachstumsprozess verbraucht wird.

Um die Wachstums- und Strukturänderungsmechanismen und ihre Auswirkungen zu verstehen, müssen neben den mechanischen Eigenschaften auch das Zellverhalten, das diese hervorruft, berücksichtigt werden. Das Ziel der Systembiologie ist es, dieses Verhalten mit Hilfe von Modellen, die die intra- und extrazellulären Signalpfade abbilden, zu beschreiben.

Auf zellulärer Ebene sind Wachstum und Strukturänderung das Resultat von chemischen Interaktionen zwischen unterschiedlichen Zellarten. Während des Umbaus der Knochenmatrix wird zunächst die bestehende Knochenmatrix durch Osteoklasten entfernt, bevor sie durch Osteoblasten wiederaufgebaut wird (Frost, 1969). Es ist das Ziel der systembiologischen Zellpopulationsmodelle von Lemaire *et al.* (2004) und Peterson & Riggs (2010), diese Mechanismen, die sich auch in Experimenten beobachten lassen, möglichst genau zu reproduzieren. Ihre Modelle berücksichtigen nicht die mechanische Belastung der Knochenmatrix. Durch Erweiterung des Modells um Osteozyten und Signalpfade für die Mechanotransduction gelingt es Maldonado *et al.* (2006, 2007), auch diese zu berücksichtigen.

Durch das Zusammenführen eines biomechanischen Modells mit einem systembiologischen Zellpopulationsmodell können Hazelwood *et al.* (2001) einen Algorithmus entwickeln, der

die wesentlichen Eigenschaften der inneren Knochenstruktur abbilden kann. Das von ihnen entwickelte Modell wird von Nyman *et al.* (2004a) verwendet, um die Form und Befestigung von Endoprothesen zu bewerten. Darüber hinaus ist das Modell in der Lage, auch den Einfluss von Hormonänderungen oder Auswirkungen von Medikamenten zu berücksichtigen (Nyman *et al.*, 2004b; Wang *et al.*, 2009).

Im Rahmen dieser Arbeit werden mit Hilfe moderner Berechnungsverfahren Methoden entwickelt, die das Zusammenfügen von biomechanischen Simulationen und system-biologischen Berechnungen zu einem gemeinsamen Programm erleichtern. Durch den Einsatz von Workflow-Technik im wissenschaftlichen Umfeld lassen sich existierende Anwendungen unterschiedlicher Software-Hersteller zu einer gemeinsamen Simulation zusammenfassen. Zur Steuerung des Programms durch den Workflow muss für jede Anwendungen ein Web-Service-Interface zur Verfügung stehen. Durch dieses flexible Interface lassen sich neue Programme beliebig aus bestehenden Programmen zusammensetzen, wobei das Workflow-Management-System die Steuerung und Koordination übernimmt. Die Vorteile dieser Methode werden gezeigt, indem der phenomenologische Knochenumbau-Algorithmus durch ein biologisch motiviertes Zellpopulationsmodell ersetzt wird.

Gliederung der Arbeit

Zunächst gibt Kapitel 2 einen Überblick über die chemischen und biologischen Grundlagen dieser Arbeit. Es beinhaltet chemische Reaktionen, Membran-Transport-Mechanismen und den Energiestoffwechsel von Zellen.

Anschließend werden in Kapitel 3 die kontinuumsmechanischen Grundlagen eingeführt, die für die Modellierung biologischer Gewebe verwendet werden. Biologische Gewebe werden dabei als mehrphasige, poröse Materialien mit mehreren interagierenden Komponenten modelliert. Das dazu verwendete mehrphasige Materialmodell besteht aus überlagerten fluiden und festen Phasen, die miteinander interagieren, wobei die extrazelluläre Matrix und die Zellen durch die feste Phase beschrieben werden. Das extrazelluläre Fluid, das diese umgibt, wird in der fluiden Phase zusammengefasst. Diese besteht aus einem flüssigen Lösungsmittel und mehreren gelösten Komponenten. Dem Konzept der superponierten Kontinua folgend wird für jede Konstituierende eine eigene Bewegungsfunktion eingeführt. Mit Hilfe allgemeiner Bilanzrelationen werden die Bilanzen für den Gesamtkörper und die Konstituierenden axiomatisch eingeführt, wobei die Interaktion zwischen den Konstituierenden über Produktionsterme berücksichtigt wird.

Die nächsten zwei Kapitel beschäftigen sich mit der thermodynamisch konsistenten Materialmodellierung. Zunächst werden in Kapitel 4 die allgemeinen Bilanzgleichungen aus Kapitel 3 an das tatsächliche Materialverhalten angepasst. Dazu werden zunächst zusätzliche Annahmen und Bedingungen eingeführt. Zur weiteren Vereinfachung werden die gelösten Stoffe in Kapitel 5 mit dem Wachstumsenergieprinzip zu einer einzelnen, nicht-mechanischen Größe zusammengefasst. Dadurch wird die Anzahl an unbekannten Feldgrößen reduziert. Mit dem reduzierten Gleichungssatz werden äquivalente thermodynamische Einschränkungen ermittelt und thermodynamisch konsistente Materialgesetze für das extrazelluläre Fluid und die enthaltene Wachstumsenergie gegeben.

Die numerische Umsetzung des Modells wird in Kapitel 6 beschrieben. In Abschnitt 6.1 wird zunächst eine herkömmliche Implementierungsstrategie erläutert. Dabei wird das gesamte Modell mit Hilfe eines einzelnen Programms als Ganzes gelöst. Dazu wird die schwache Formulierung der zugrundeliegenden partiellen Differentialgleichungen implementiert und mit Hilfe eines Standard-Galerkin-Verfahrens (Bubnov-Galerkin) in Raum und Zeit diskretisiert und mit einem impliziten Zeitintegrationsverfahren gelöst. Ein alternatives, entkoppeltes Lösungsverfahren ist in Abschnitt 6.2 beschrieben. Dabei werden die zugrundeliegenden Gleichungen aufgeteilt und von eigenen spezialisierten Programmen gelöst. Der Kontroll- und Datenfluss zwischen den Programmen erfolgt über Webservice- und Datenbankschnittstellen und wird durch einen übergeordneten Workflow kontrolliert.

In Kapitel 7 wird das Modell auf unterschiedliche Gewebe angewendet, und es werden die Simulationergebnisse präsentiert. Dazu werden zunächst die gewebespezifischen Konstitutivgleichungen eingeführt und in drei-dimensionalen Simulationen angewendet. Im Einzelnen wird in Abschnitt 7.1 das Wachstum von avaskulären Tumoren beschrieben. Abschnitt 7.2 beschäftigt sich mit dem Umbauprozess in Knochen. Der dabei verwendete phänomenologische Umbau-Algorithmus wird in Abschnitt 7.3 durch ein biologisch motiviertes Zellpopulationsmodell ersetzt.

Eine abschließende Disskussion der Ergebnisse sowie den Ausblick auf zukünftige Arbeiten enthält Kapitel 8.

List of Figures

List of Tables

Nomenclature

Acronyms

Abbreviation	Description
ADP	adenosine diphosphate
AMP	adenosine monophosphate
ATP	adonsine triphosphate
DAE	differential algebraic equation
DIRK	diagonal implicit *Runge-Kutta*
$FADH_2$	falvin adenine dinucleotide
FAD	falvin adenine dinucleotide (reduced form)
FE	finite element
FEM	finite-element method
GTP	guanin triphosphate
LBB	*Ladyzhenskaya-Babuška-Brezzi*
NAD^+	nicotinamide adenine dinucleotide
NADH	nicotinamide adenine dinucleotide (reduced form)
ODE	ordinary differential equation
OPG	osteoprotegerin
PGE_2	prostagladine E_2
RANK	receptor activator of nuclear factor kappa
RANKL	receptor activator of nuclear factor kappa ligand
REV	representative elementary volume
WSDL	Web Service Description Language
SOA	service-oriented architecture
SOAP	formally know as Simple Object Access Protocol
TGF-β	transforming growth factor beta
WS-BPEL	Web-Service Business Process Execution Language
TPM	Theory of Porous Media
XML	Extensible Markup Language

Conventions

Symbol	Description
Basic conventions	
$(\cdot)$	an arbitrary quantity
$(\bar{\cdot})$	boundary terms
$(\tilde{\cdot})$	boundary terms
$(\hat{\cdot})$	production terms
$(\tilde{\cdot})$	Growth-energy quantity that differs from its exact value
$\mathrm{d}(\cdot)$	differential element of a quantity
$\delta(\cdot)$	test function
$(\dot{\cdot})_\alpha$	first material time derivative with respect to constituent α
$(\ddot{\cdot})_\alpha$	second material time derivative with respect to constituent α
$(\dot{\cdot})$	time derivative with respect to the overall mixture
Superscripts	
$(\cdot)^\alpha$	quantity of a constituents
$(\cdot)^\beta$	quantity of a fluid constituents
$(\cdot)^\gamma$	quantity of a solutes
$(\cdot)^\delta$	quantity of a cell population
$(\cdot)^\zeta$	quantity of a signalling molecules
$(\cdot)^B$	quantity of the osteoblast population
$(\cdot)^\mathcal{C}$	quantity of the growth energy
$(\cdot)^C$	quantity of the osteoclast population
$(\cdot)^F$	quantity of the fluid phase
$(\cdot)^L$	quantity of the liquid solvent
$(\cdot)^R$	quantity of the pre-osteoblast population
$(\cdot)^Y$	quantity of the osteocyte population
$(\cdot)^S$	quantity of the solid matrix
$(\cdot)^h$	quantity in the discrete space
$(\cdot)^{\cdot R}$	effective (or realistic) quantity
Subscripts	
$(\cdot)_\alpha$	kinematic quantity of a constituents
$(\cdot)_\beta$	kinematic quantity of a fluid constituents
$(\cdot)_\gamma$	kinematic quantity of a solutes
$(\cdot)_S$	kinematic quantity of the solid matrix

Symbol	Description
$(\cdot)_F$	kinematic quantity of the fluid phase
$(\cdot)_L$	kinematic quantity of the liquid solvent
$(\cdot)_{\mathcal{C}}$	kinematic quantity of the growth energy
$(\cdot)_{\cdot F}$	quantity with respect to the overall fluid volume
$(\cdot)_{\cdot\theta}$	quantity of the temperature-equivalent growth energy
$(\cdot)_E$	effective (or extra) quantity
$(\cdot)_{0S}$	quantity of the solid reference configuration
$(\cdot)_{tS}$	quantity of the solid accompanying configuration
$(\cdot)_{E/\mathrm{mech}}$	mechanical part of an effective quantity
$(\cdot)_{\mathrm{mech}}$	mechanical part of a quantity
$(\cdot)_0$	quantity at standard state or initial values

Symbols

Symbol	Unit	Description
Calligraphic letters		
$\mathcal{C}^F$	$[\mathrm{J/m^3}]$	concentration-equivalent growth energy
$\hat{\mathcal{C}}^F$	$[\mathrm{J/m^3\,s}]$	growth-energy production
$\mathcal{C}_\theta^\alpha$	$[\mathrm{J/m^3}]$	temperature-equivalent growth energy
$\mathcal{D}$, $\mathcal{D}_{(\cdot)}$	$[\mathrm{J/K\,m^3\,s}]$	internal dissipation
$\boldsymbol{\mathcal{G}_u}$		function vector of all weak formulations (global residuum)
$\mathcal{P}$	$[\mathrm{N/m^2}]$	pressure-equivalent *Lagrange*an multiplier
$\mathcal{S}_{\boldsymbol{u}}$		trial space
$\mathcal{T}_{\boldsymbol{u}}$		test space
Latin letters		
A^S	$[\mathrm{m^2/m^3}]$	volume-specific surface area
A^δ	$[1/\mathrm{s}]$	apoptosis rate coefficient
$\boldsymbol{A}$		local mass matrix of the space-discrete coupled system
$\mathbf{b}$, $\mathbf{b}^\alpha$	$[\mathrm{m/s^2}]$	mass-specific volume-force vector
$\mathbf{b}_c$		space-discrete growth-energy production
$\mathbf{c}$		nodal values of the growth energy
$\mathbf{c}_c$		numerical coupling term
$\boldsymbol{C}$		interpolation functions of the FE mesh for $\mathbf{c}$
c_m^β	$[\mathrm{mol/m^3}]$	molar concentration
$\mathbf{d}_{\beta F}$	$[\mathrm{m/s}]$	mixture-component diffusion vector

Symbol	Unit	Description
D_θ^α $D^{\mathcal{C}}$	[m/s]	growth-energy diffusion coefficient
D^δ	variant	development rate coefficient
$\hat{e}^\alpha$	[J/m^3 s]	total energy production
$\mathbf{f}$		global force vector of the space-discrete system
$\mathbf{f}_u$, $\mathbf{f}_p$, $\mathbf{f}_c$		space-discrete *Neumann* boundary conditions
f^γ	[J/kg]	energy value
$f^{\mathcal{C}}$	[J/kg]	average energy value
$\mathbf{F}_\alpha$	[–]	deformation gradient
$\hat{\mathbf{h}}^\alpha$	[N/m^2]	total production of moment of momentum
$\mathbf{j}_\theta^\alpha$	[J/m^2 s]	growth-energy influx vector
k^F	[m/s]	conventional hydraulic conductivity(*Darcy* permeability)
$\mathbf{K}^\beta$	[J/kg]	chemical potential tensor
$\boldsymbol{K}$		global stiffness matrix of the space-discrete coupled system
$\boldsymbol{K}_{ij}$		submatrix of the global stiffness matrix
K^S	[–]	intrinsic skeleton permeability
$K_M^{(\cdot)}$	variant	*Michaelis* constant
$\mathbf{L}_\alpha$	[–]	spatial velocity gradient
$\mathbf{n}$	[–]	outward-oriented normal vector
n^α	[–]	volume fraction
n_m^β	[–]	number of moles
m^α	[kg]	constituent mass
$\boldsymbol{M}$		global mass matrix of the space-discrete coupled system
$\boldsymbol{M}_{ij}$		submatrix of the global mass matrix
$\boldsymbol{M}_{\boldsymbol{u}(i)}$		global basis functions of the trail functions
$\hat{\mathbf{m}}^\alpha$	[N/m^2]	direct production of moment of momentum
$\boldsymbol{N}_{\boldsymbol{u}(i)}$		global basis functions of the test functions
$\mathbf{p}$		nodal values of the fluid pressure
$\boldsymbol{P}$		interpolation functions of the FE mesh for $\mathbf{p}$
p_0	[N/m^2]	hydraulic pressure
p^{FR}	[N/m^2]	effective fluid pressure
P		product species of a chemical reaction
$\hat{\mathbf{p}}^\alpha$	[N/m^3]	direct momentum-production vector
P^α		material point
$\mathbf{q}$, $\mathbf{q}^\alpha$	[J/m^2 s]	heat influx vector
$\boldsymbol{q}$		vector of internal variables

Symbol	Unit	Description
$\mathbf{q}$		all internal variables of the FE mesh
$\boldsymbol{r}$		local stiffness vector
r, r^α	[J/kg s]	external heat supply
R		reactant species of a chemical reaction
R	[J/K mol]	universal gas constant
R^β	[J/K mol]	specific gas constant
$\hat{\mathbf{s}}^\alpha$	[N/m^3]	total momentum-production vector
t	[s]	time
t_0	[s]	initial time
$\mathbf{t}$, $\mathbf{t}^\alpha$	[N/m^2]	external contact-force vector
$\mathbf{T}$, $\mathbf{T}^\alpha$	[N/m^2]	*Cauchy* stress tensor
$\boldsymbol{u}$		vector of unknowns
$\mathbf{u}$		all nodal degrees of freedom of the FE mesh
$\mathbf{u}_S$		nodal values of the solid displacement
$\boldsymbol{U}$		interpolation functions of the FE mesh for $\mathbf{u}_S$
$\mathbf{u}_S$	[m]	solid displacement vector
$\mathbf{w}_\beta$	[m/s]	seepage velocity vector
v	[m^3]	bulk volume
v^α	[m^3]	partial volume of constituent α
$\mathbf{v}_\alpha$	[m/s]	current velocity vector
W^S		solid strain energy
$\mathbf{x}$	[m]	current position vector
$\mathbf{X}_\alpha$	[m]	referential position vector
Greek letters		
α	[N/m^2]	growth stress constant
γ	[m^3/J s]	tumour proliferation coefficient
γ^{FR}	[N/m^3]	effective fluid weight
Γ		overall boundary
$\Gamma_{(\cdot)}$		*Neumann* or *Dirichlet* boundary
δ	[1/s]	tumour necrosis coefficient
$\Delta_r G$	[J/mol]	reaction *Gibbs* enthalpy
$\Delta_r G_0$	[J/mol]	standard reaction *Gibbs* enthalpy
ε, ε^α	[J/kg]	internal energy
$\hat{\varepsilon}^\alpha$	[J/m^3 s]	direct energy production
$\hat{\zeta}$, $\hat{\zeta}^\alpha$	[J/K m^3 s]	direct entropy production

Symbol	Unit	Description
η, η^α	$[\mathrm{J/K\,kg}]$	mass specific entropy
η_θ^α	$[\mathrm{m^3/kg}]$	configurational growth entropy
$\hat{\eta}$, $\hat{\eta}^\alpha$	$[\mathrm{J/K\,m^3\,s}]$	total entropy production
θ, θ^α	$[\mathrm{K}]$	temperature
λ^S	$[\mathrm{N/m^2}]$	1st *Lamé* constant
μ^S	$[\mathrm{N/m^2}]$	2nd *Lamé* constant
μ_m^γ	$[\mathrm{J/mol}]$	molar chemical potential
μ^β	$[\mathrm{J/kg}]$	mass-specific chemical potential
μ_0^β	$[\mathrm{J/kg}]$	standard chemical potential
μ^{FR}	$[\mathrm{N\,s/m^2}]$	effective fluid shear viscosity
ν^γ		stoichiometric coefficient
ξ^α	$[\mathrm{J/kg}]$	*Gibbs* free enthalpy
π, π^β	$[\mathrm{N/m^2}]$	osmotic pressure
ρ	$[\mathrm{kg/m^3}]$	mixture density
ρ^α	$[\mathrm{kg/m^3}]$	partial density
$\hat{\rho}^\alpha$	$[\mathrm{kg/m^3\,s}]$	mass production
$\rho^{\alpha R}$	$[\mathrm{kg/m^3}]$	material or realistic density
ρ_F^β	$[\mathrm{kg/m^3}]$	partial pore density
σ_η, σ_η^α	$[\mathrm{J/K\,kg\,s}]$	entropy supply
τ_θ^S	$[\mathrm{1/s}]$	growth-energy absorption rate
$\boldsymbol{\phi}_\eta$, $\boldsymbol{\phi}_\eta^\alpha$	$[\mathrm{J/K\,m^2\,s}]$	entropy efflux vector
φ		overall aggregate
φ^α		constituent α
ψ^α	$[\mathrm{J/kg}]$	mass-specific *Helmholtz* free energy
Ψ_F^α	$[\mathrm{J/m^3}]$	volume-specific *Helmholtz* free energy
Ω		spatial domain

Further, example-specific material parameters are found in chapter 7 in Table 7.1, Table 7.2 and Table 7.4.

Chapter 1: Introduction and overview

It is the aim of this work to present an accurate way of modelling, growth and remodelling processes within the framework of continuum biomechanics. Therefore, a multiphase continuum approach is used for the material modelling, where the cells and the extracellular matrix are represented by the solid constituent, and the extracellular liquids are summarised as the fluid constituents. Furthermore, biological processes only occur if the involved cells are sufficiently supported by metabolites (oxygen, vitamins, nutrients, etc.), which are needed for cell metabolic processes. Therefore, following the ideas of Markert & Ehlers (2007) as well as of Ambrosi & Guillou (2007), a single, non-mechanical quantity is introduced to summarise the metabolites inside the extracellular liquids. This approach provides the necessary thermodynamic restrictions which are evaluated for avascular tumour growth and bone remodelling.

To understand the mechanism of growth and remodelling and its consequences, the mechanics as well as the cell dynamics must be considered. In this regard, the Systems Biology aims at investigating the intra- and extracellular signalling pathways, which are involved in the mechanotransduction and trigger the metabolic processes. Using modern computational methods allows for the combination of systems-biological and biomechanical methods within an integrated approach. In this context, Scientific Workflow technology provides an excellent platform to allow for the integration of existing legacy applications from different vendors into an integrative simulation workflow. Therefore, the existing applications are extended or wrapped by a webservice interface, which is then invoked by the workflow instances. This radically new approach allows for a straight-forward merging of computational models from different scales and provides the possibility to further expand each model individually. To reveal the capability of the multi-field growth model, three-dimensional (3-d) simulation examples of both phenomena are presented. This allows the integrated use of separated numerical applications as webservices for each simulation part, which are controlled by a workflow management system. By replacing the phenomenological bone remodelling algorithm with a biologically motivated cell population model, the benefits of this method are demonstrated.

1.1. Introduction

In the last decades, continuum mechanics was extensively applied in the context of material modelling of hard and soft biological tissues, such as bone, cartilage or muscle, where nonlinear, inelastic and anisotropic properties have been addressed. Reviews of achievements in biomechanics of biological tissues including growth and remodelling are given by Taber (1995) and Humphrey (2003). Here, particularly focussing on biological growth processes, it is apparent that growing tissues not only undergo changes in size and shape but also in their inner structure and inherent properties. Real biological tissues are composed of many constituents like various cell types, abundant water, extracellu-

lar matrix (ECM), etc., cf. Cowin (2000) for details. Thus, growth processes may cause changes in the relative amount of these components as well as their mechanical properties. Thereby, the macroscopic mechanical behaviour is primarily governed by the interaction among cells of different types on the microstructure. For example, bone cells permanently synthesise and resorbe the bone matrix within living bones. This process is summarised as bone remodelling. Thereby, the bone matrix is adapted to the local loading situation. In regions with a high mechanical stress, the mass of bone matrix increases, while in regions with a low mechanical stress, the mass of bone matrix decreases.This fundamental principle of orthopaedics, called *Wolff*'s[1] law, goes back to Wolff (1892) and is the basis for all modern bone remodelling simulations.

To describe the growth and remodelling in the context of continuum mechanics, different methods have been developed and applied. Cowin & Hegedus (1976) introduced the open-system theory as a general framework for the description of stress-induced remodelling of bones by a single-phase model. Thereby, only the bone matrix is assumed to influence the overall mechanical behaviour, and the fluid constituents are neglected. Several researchers applied this framework to bone remodelling using phenomenological remodelling algorithms, where the strain energy triggers the changes of the bone matrix density (cf., e. g., Beaupré *et al.*, 1990; Lutz & Nackenhorst, 2010; Weinans *et al.*, 1994). Without consideration of the underlying biological processes, these models focus on the 3-d reproduction of the bone density distribution as result of the applied mechanical loads rather than on accurately describing the remodelling process itself. Recent reviews on bone remodelling models and simulations are given by Mellon & Tanner (2012); Webster & Müller (2011).

The open-system theory has also been applied to other growing biological tissues. For example, growth of tumour spheroids was described by Ambrosi & Mollica (2002, 2004) by employing an open single-phase material model with an additional nutrient concentration that triggers the growth process. A recent overview of different tumour models is given by Unnikrishnan *et al.* (2010).

Multiphasic models, which also include extracellular fluids, are proposed by Ricken & Bluhm (2009) for stress-dependent remodelling processes as well as by Ambrosi & Preziosi (2002) and by Byrne & Preziosi (2003) for the description of avascular tumours. Moreover, Preziosi & Tosin (2009) describe tumorous and healthy tissue using a triphase material description, where they consider cells and matrix as individual phases.

To verify the thermodynamic consistency, the constitutive laws that describe growth and remodelling processes are thermodynamically evaluated. Krstin *et al.* (2000) provide an entropy evaluation, where they claim the bone remodelling process to be a reversible process at thermodynamic equilibrium. Kuhl & Steinmann (2003) developed a general framework for the open-systems theory. Furthermore, they introduced additional momentum, energy and external entropy productions, which represent the amount of the respective quantity carried by the newly created mass and which have to be determined constitutively. Moreover, Steeb & Diebels (2003) claim that the thermodynamic restric-

[1] *Julius Wolff* (1836–1902): German anatomist and surgeon, who was the first professor of orthopaedics at the Charité (Berlin) and founder and director of the Department of Orthopaedics at the Charité.

tions derived for erosive processes also hold for the description of growth and remodelling. However, they did not take into account that growth and atrophy (negative growth) follow individual biochemical pathways, which have to be evaluated individually. Ambrosi & Guillou (2007) provide a general framework for the description of growth and remodelling processes in a single-phase material model by employing an additional biochemical growth energy, which is consumed during growth and remodelling.

On the cellular scale, growth and remodelling are the result of chemical interactions among cells of different types. Regarding bones, initially the bone matrix is removed by osteoclasts followed by osteoblasts, which form a new bone matrix (Frost, 1969). The systems-biological cell population models introduced by Lemaire *et al.* (2004) and Peterson & Riggs (2010) aim to accurately reproduce these mechanisms observed in experiments. Nevertheless, these models exclude the influence of osteocyctes, which act as mechanical sensors inside the bone matrix and are therefore unable to reproduce effects of mechanical stimulation. These were included into the model proposed by Maldonado *et al.* (2006, 2007), which extends the work of Lemaire *et al.* (2004) by introducing osteocytes and signalling pathways for mechanotransduction.

By combining a biomechanical model with a systems-biological cell population model, Hazelwood *et al.* (2001) provide a finite-element algorithm that predicts important features of the internal bone structure, which also can be observed in experiments. This model was used to evaluate the design and fixation techniques of implants (Nyman *et al.*, 2004a) and, in addition, it is also capable to predict the influence of postmenopausal hormonal changes and long-term effects of medical treatments (Nyman *et al.*, 2004b; Wang *et al.*, 2009). For the numerical solution of the aforementioned models, the systems-biological model as well as the mechanical model were integrated into a single finite-element framework.

Here, modern numerical methods are introduced that allow for the solution of combined biomechanical and systems-biological models in a decoupled fashion. Using a service-oriented architecture, the solution of each submodel is provided as a service, which is accumulated to the solution of the whole problem. More precisely, each subproblem is solved by a tailored program, which is controlled via a standardised webservice interface.

1.2. Outline of the Thesis

Starting with chapter 2, the chemical and biological fundamentals of this thesis are briefly reviewed. Thereby, the major focus lies on the cellular energy metabolism. In particular, chemical reactions, membrane transport mechanisms and the cellular energy metabolism are introduced.

In chapter 3, the continuum-mechanical fundamentals used to model biological tissues are introduced. Thereby, biological tissues are treated as multiphase, porous materials, which are formed by several interacting components. To describe the mechanical behaviour of the overall biological material, living tissues are modelled as multiphase continua, which basically consist of superimposed and interacting solid and fluid phases, where the extracellular matrix and the cells that adhere to it are summarised within the solid phase.

These are surrounded by the extracellular fluid, which is subsumed in the fluid phase. It is itself a homogeneous, dilute solution, which contains a liquid solvent and several solutes. Thereby, following the concept of superimposed continua, the kinematics of the constituents are described by individual motion functions. Using the concept of master balances, the overall and constituent balance equations are axiomatically introduced. Therein, production terms account for the interactions among the constituents.

The following two chapters focus on the thermodynamic restrictions imposed on the material under consideration. In particular, chapter 4 is concerned with tailoring the general balance equations obtained in chapter 3 to the specific material under consideration. To this end, additional modelling assumptions and restrictions are introduced. Instead of evaluating the entropy inequality directly, a general concept that reduces the number of solutes to a single non-mechanical quantity, and therewith the set of equations, is introduced in chapter 5. Employing the reduced set of equations, equivalent thermodynamic restrictions are determined and thermodynamically consistent material laws are introduced for the extracellular fluid and the growth energy.

The main focus of chapter 6 is on the numerical treatment. First, a traditional solution strategy is summarised in Section 6.1, where the whole problem is included into a single application and solved at once. In particular, the weak variational formulation of the governing partial differential equations is implemented and numerically discretised in space and time by employing a standard Galerkin method (Bubnov-Galerkin) with a mixed finite-element method for the discretisation and an implicit time integration scheme for its solution. In contrast to that, in Section 6.2, a decoupled, service-oriented solution strategy is introduced. To this end, the governing equations are separated from each other and solved by individual tailored programs. Using web-service interfaces for the communication, an overall workflow controls the program execution and manages the data exchange.

In chapter 7, the presented model is applied to different biological tissues. The constitutive equations that provide the tissue-specific material laws for the specimen under consideration are introduced. Coupled, 3-d numerical simulations reveal the full capacity of the described modelling approach. In particular, in Section 7.1, the description of avascular tumour growth is provided, Section 7.2 focuses on a phenomenological bone remodelling description, which is extended in Section 7.3 by a biologically motivated cell-population model for bone remodelling.

A final discussion and an outlook on future work is given in chapter 8.

Chapter 2: Chemical and biological fundamentals

On a cellular and subcellular level, growth and remodelling can be seen as the result of multiple chemical reactions, following complex metabolic pathways. This chapter aims at describing the fundamentals of chemical and biological processes. It lays the basis for the continuum-mechanical consideration that follows in the next chapters. This chapter is by no means complete, it rather provides a brief overview on the basic principles that can be found in textbooks on chemistry, biology and physics (cf. Adam *et al.*, 2009; Atkins & de Paula, 2006; Baehr & Kabelac, 2012; Junqueira & Carneiro, 2005; Klotz & Rosenberg, 2000; Löffler, 2008). In particular, chemical reactions, membrane transport mechanisms and the cellular energy metabolism are introduced.

2.1. Chemical reactions

Chemical reactions are processes, which transform a set of chemical substances into another. Thereby, chemical bonds between atoms are formed and broken. Chemical reaction equations are graphical representations of chemical reactions. Consider a general chemical reaction of the form

$$\sum_{\mathrm{R}} \nu^{\mathrm{R}} \mathrm{R} \longrightarrow \sum_{\mathrm{P}} \nu^{\mathrm{P}} \mathrm{P} \,. \tag{2.1}$$

Therein, R denotes the reactant species and P denotes product species, where the stoichiometric coefficients ν^{R} and ν^{P} give the relative amount of the corresponding species and the arrow indicates the direction of the reaction. The direction of the reaction is governed by the change of the *Gibbs*[1] enthalpy during the reaction, which can be determined as the difference of the molar chemical potentials μ_m^{γ}:

$$\Delta_r G = \sum_{R} \nu^{\mathrm{R}} \mu_m^{\mathrm{R}} - \sum_{\mathrm{P}} \nu^{\mathrm{P}} \mu_m^{\mathrm{P}} \,. \tag{2.2}$$

Therein the chemical potential, is an intensive thermodynamic quantity that characterises the ability of a species to react with other species. Furthermore, the change of the *Gibbs* free enthalpy depends on the conditions under which the reaction occurs. The standard reaction *Gibbs* free enthalpy $\Delta_r G_0$ (with subscript 0) is determined under standard conditions, which are a temperature of 25°C (298.16 K), a pressure of 101.325 Pa and the reactants and products in their standard states. $\Delta_r G$ (without subscript 0) indicates that the reaction *Gibbs* enthalpy is determined under conditions that differ from the standard conditions. In addition, for reactions that take place in solutes, the products and reactants are present at 1.0 molal activity, i. e., 1.0 mole solute is dissolved in 1.0 kg solvent.

[1] *Josiah Willard Gibbs* (1839–1903): American scientist, who contributed to physics, chemistry and mathematics. In 1901, he received the *Copley* Medal of the Royal Society London "for his contributions to mathematical physics".

Concerning the spontaneity of the above equilibrium reaction at constant temperature and pressure, the following relations hold:

- If $\Delta_r G < 0$, the forward reaction is spontaneous and thermodynamically favourable
- If $\Delta_r G > 0$, the reverse reaction is spontaneous and the forward reaction thermodynamically unfavourable.
- If $\Delta_r G = 0$, the reaction is at equilibrium.

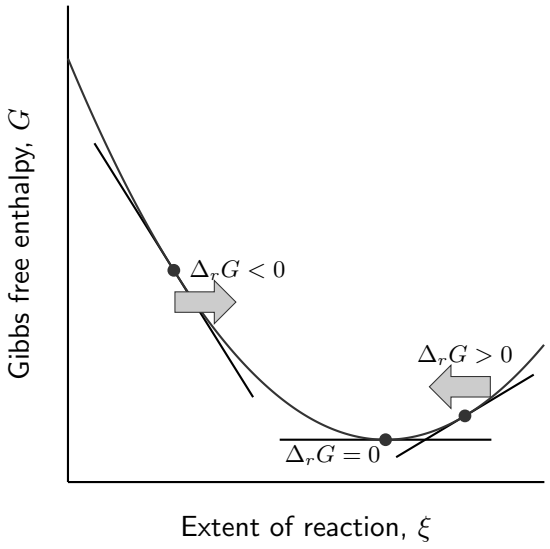

Figure 2.1.: Spontaneous reactions yield towards the minimum of the *Gibbs* enthalpy, which marks the equilibrium (Figure adopted from Atkins & de Paula, 2006, p. 201).

As can be seen in Figure 2.1, reactions always tent towards the local minimum of the *Gibbs* enthalpy, which marks the chemical equilibrium. At equilibrium, $\Delta_r G = 0$, a reaction is not spontaneous in neither direction. The actual position of the equilibrium depends on the composition of the mixture, temperature and pressure. In any case, the equilibrium is determined by setting (2.2) equal to zero. The chemical equilibrium is a dynamic equilibrium, where forward and backward reaction are balanced. This is indicated by a double arrow in an equilibrium reaction equation $\mathrm{R} \rightleftharpoons \mathrm{P}$, where $\mathrm{R} \longrightarrow \mathrm{P}$ is the forward reaction and $\mathrm{R} \longleftarrow \mathrm{P}$ is the reverse reaction. Reactions with $\Delta_r G < 0$ are exergonic, i. e., they proceed spontaneous without needing an external supply of energy and might be used as sources of energy. In contrast, reactions with $\Delta_r G > 0$ are endergonic, these occur only if they are coupled to an exergonic reaction. Giving an example, during the phosphorylation of adenosine diphosphate (ADP) a phosphate group is added to ADP yielding adenosine triphosphate (ATP). This reaction is, under standard conditions, an endergonic reaction of the form

$$\begin{aligned} &\mathrm{ADP} + \mathrm{HPO_4^{2-}} \longrightarrow \ldots \longrightarrow \mathrm{H_2O} + \mathrm{ATP} \\ &\Delta_r G_0 = +31.4\,\mathrm{kJ/mol}\,. \end{aligned} \tag{2.3}$$

This is a simplified reaction equation of a complex reaction, that requires several intermediate steps. In humans, this reaction occurs in the respiratory chain of the mitochondria (subsection 2.3.1) as well as during glycolysis (subsection 2.3.2) and fatty-acid oxidation (subsection 2.3.3). As well, at standard conditions, the synthesis of two molecules lactate from one molecule glucose is an exergonic reaction, which is known as lactic fermentation, which is required for the production of sauerkraut and yoghurt:

$$\begin{aligned} &\mathrm{C_6H_{12}O_6} \longrightarrow \ldots \longrightarrow 2\,\mathrm{CH_3CH(OH)COO^-} + 2\,\mathrm{H^+} \\ &\Delta_r G^0 = -198.3\,\mathrm{kJ/mol}\,. \end{aligned} \tag{2.4}$$

To make the phosphorylation of ADP possible both reactions are, in the cellular energy metabolism, enzymatically coupled yielding an overall chemical change of

$$\begin{aligned} &\mathrm{C_6H_{12}O_6} + 2\,\mathrm{ADP} + 2\,\mathrm{HPO_4^{2-}} \longrightarrow 2\,\mathrm{CH_3CH(OH)COO^-} + 2\,\mathrm{H^+} + \mathrm{H_2O} + 2\mathrm{ATP} \\ &\Delta_r G_0 = -135.6\,\mathrm{kJ/mol}\,. \end{aligned} \tag{2.5}$$

Therein, reaction *Gibbs* free enthalpy can be determined by adding the *Gibbs* free enthalpy needed for the phosphorylation of two ADP to the *Gibbs* free enthalpy in (2.4), yielding an exergonic reaction, which proceeds from left to right. Following this principle, many endergonic reactions that occur inside cells are enzymatically coupled to exergonic reactions, such as the hydrolysis of ATP, which is part of the cellular energy metabolism.

2.2. Cellular uptake mechanisms

The cytosol (intracellular fluid) and extracellular fluids are liquid solutions separated by a selectively permeable plasma membrane. Inside eucaryotic cells (cells with a nucleus) further selectively permeable membranes separate the content of the cell organelles from the cytosol. The cellular membranes consist of a lipid bilayer, and uncharged, nonpolar (hydrophobic) molecules, which readily dissolve in oil, such as O_2 and CO_2 rapidly diffuse through it. Also small uncharged, polar molecules such as water and urea pass through the bilayer however more slowly. By contrast, the cellular membranes are highly impermeable for charged molecules (ions) regardless of their size. The nutrients needed by the cells must pass the membrane either by diffusion through the membrane or via membrane transport molecules. Ions and large polar, hydrophilic molecules, like glucose, hardly enter the lipid bilayer and need special transport mechanisms to pass the membrane. These transport mechanisms can be further distinguished into passive transport mechanisms, where the solutes follow their electrochemical gradient, and active transport mechanisms, where the transport is coupled to an energy source.

2.2.1. Transport mechanisms

For ions and large molecules, which pass the cell membrane very slowly, special transport mechanisms are provided by membrane transport proteins. Thereby, carrier proteins and channel proteins are the major classes of membrane transport proteins. Channel proteins

form aqueous pores across the membrane. Specific molecules, usually inorganic ions with an appropriate size and charge, pass through the channel proteins, when it is opened. Carrier proteins bind the solute and transfer it across the lipid bilayer by undergoing a series of conformational changes.

Channel proteins and many carrier proteins provide only passive transport mechanisms, where the solutes are transported along the electrochemical gradient. In case of uncharged molecules, the transport direction is given by the difference in the chemical potential on both sides of the membrane (Baehr & Kabelac, 2012, subsec. 5.1.5). During a passive transport, molecules are transferred form the side with the higher chemical potential to the side with the lower chemical potential. It reaches its equilibrium when the chemical potentials on both sides are equal. Like the heat transfer among the phases, which is driven by the temperature, the chemical potential is the driving force of the passive mass exchange among the phases. For the transport of charged molecules also the electrical difference across the membrane must be considered. The combination of the chemical potential and the electrical gradients yields the electrochemical gradient, which drives the diffusion of charged molecules.

Some solutes are actively pumped across the membrane against the electrochemical gradient. These active transport mechanisms require an additional energy source and are therefore either coupled to an exergonic chemical reaction, or co-transported with another molecule, which follows the electro-chemical gradient. If the co-transported molecules move in the same direction, the carrier protein is also called symporter, whereas an antiporter transfers molecules in opposing direction.

2.3. Energy metabolism

In chapter 5, a new concept summarising the vast amount of disolved molecules by its metabolic energy content is introduced. This concept is closely related to the energy metabolism of the cell. Here, some basic knowledge concerning the human energy metabolisms including the glucose, the lipid and the protein metabolisms is shortly presented.

Living cells are complex and highly ordered chemical systems that must be permanently supported with energy. Vertebrates obtain energy by eating organic molecules, which are divided into carbohydrates, lipids and proteins. In the intestine, during digestion, the polymeric molecules are enzymatically broken down into their monomeric subunits, proteins into amino acids, polysaccharides into sugars, and fats into fatty acids and glycerol. After digestion, they are distributed in the whole organism via the extracellular fluids, e. g. blood, and enter the cytosol of the cells, where they are used to synthesis adenosine triphosphate (ATP, Figure 2.2) from adenosine diphosphate (ADP). Within cells, ATP acts as energy carrier, which is used to transfer the energy for the cellular reactions. The stored energy can be obtained by an exergonic hydrolysis to ADP, which is then available for another phosphorylation. Thereby, under the usual conditions within a cell, the $\Delta_r G$ of ATP hydrolysis is between -46 to $-54\,\mathrm{kJ/mol}$ and can be used to enable many endergonic reactions with a $\Delta_r G$ of perhaps $+41\,\mathrm{kJ/mol}$ (Alberts *et al.*, 2002, p. 89). Even more energy can be obtained by hydrolysing ATP to adenosine monophosphate (AMP),

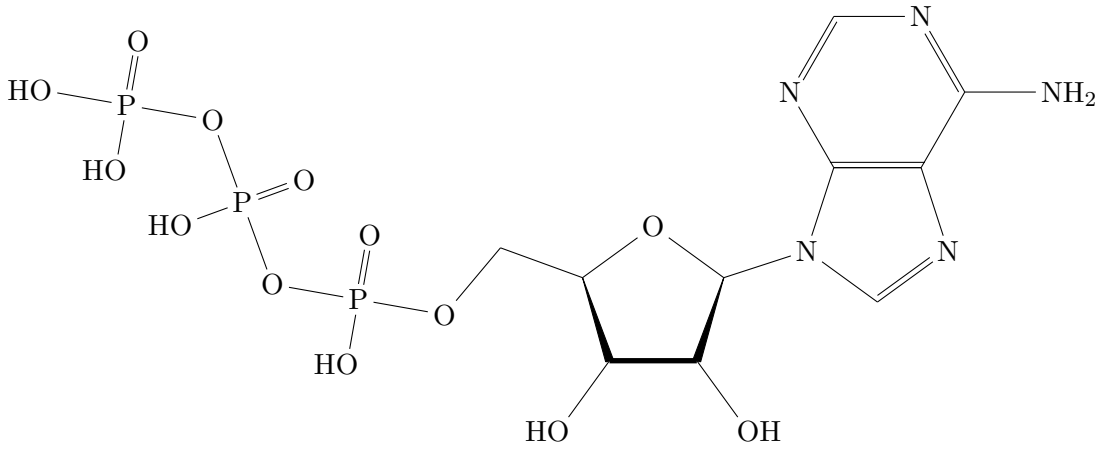

Figure 2.2.: Chemical structure of adenosine triphosphate (ATP).

which is equivalent to the hydrolisation of two ATP to ADP.

The phosphorylation of ADP is an endergonic reaction, which is, in the cellular energy metabolism, coupled to the exergonic break down of organic molecules. Thereby, it is distinguished between anaerobic (without oxygen) fermentation and aerobic (with oxygen) respiration, which is situated inside the mitochondria.

2.3.1. Respiratory chain

The respiratory chain, also known as electron transport chain, is formed by a series of enzymes, which pass electrons across the inner membrane of the mitochondria. In particular, the energy, which is released by electrons obtained from the electron carriers NADH (Nicotinamide adenine dinucleotide) and $FADH_2$ (Flavin adenine dinucleotide), is used to pump protons H^+ from the mitochondria matrix to the inter-membrane space. Therewith, an electrochemical proton gradient across the inner membrane is created. This gradient is then used to drive the ATP synthase to synthesis ATP from ADP and phosphate. It is responsible for the synthesis of most of the ATP used in aerobic cells.

The electron-transport chain is formed by four enzyme complexes in the inner membrane.

- The NADH dehydrogenase (complex I) transfers two protons and two electrons from the electron carrier NADH to the coenzyme ubiquinone (Q), a small hydrophobic molecule that is freely mobile in the lipid bilayer of the inner membrane. Thereby, ubiquinone is reduced to ubiquinol (QH_2), and four protons are transferred through the inner membrane.
- The succinate dehydrogenase (complex II) is a part of the citric acid cycle, where it catalyses the oxidation of succinate to fumerate. Thereby, it reduces FAD to $FADH_2$, which is located inside the protein complex. During the reoxidation of $FADH_2$, two electrons are transferred to ubiquinone forming ubiquinol.
- The cytochrome bc_1 complex (complex III) oxidises the ubiquinol formed by complex I and II to ubiquione. During the oxidation of one ubiquinol molecule, four

protons are released in the inter-membrane space and two electrons are transferred to cytochrome c, a small protein that transfers the electrons to complex IV.

- The cytochrome c oxidase (complex IV) is the only complex of the respiratory chain that reacts with oxygen, which is reduced to H_2O by transferring four electrons from cytochrome c. Thereby, four protons are consumed from the mitochondria and four protons are released in the inter-membrane space.

In summary, the oxidation of NADH yields a transfer of ten protons from the mitochondria matrix to the inter-membrane space, and the oxidation of $FADH_2$ yields a transfer of six protons.

In a second step, the protons flow back into mitochondria matrix following the electrochemical gradient. Thereby, approximately three protons need to pass the ATP synthase to synthesise one ATP molecule from ADP and phosphate (Blaxter, 1989, p. 73). Furthermore, it must be taken into account that the transport of one phosphate into the mitochondrial matrix via the phosphate carrier protein is catalysed by a cotransport of one proton. This yields a total output of 2.5 ATP for the oxidation of NADH and 1.5 ATP for the oxidation of $FADH_2$. Both electron carriers are obtained from the citric-acid cycle.

Citric-acid cycle

The citric-acid cycle, also known as tricarboxylic-acid cycle or *Krebs*[2] cycle, is an essential metabolic pathway, which is located inside the mitochondrial matrix. Within most aerobic organisms, the degradation of all nutrients converges onto the citric-acid cycle.

To enter the citric-acid cycle, acetyl-CoA, resulting from the catabolism of glucose, fatty acids and some amino acids react with oxaloacetate to form citrate (Figure 2.3). Then, following the reactions in Table 2.1, the acetyl group is completely oxidised to CO_2, which leaves the cells as waste product. Thereby, the *Gibbs* free enthalpy of the reaction is conserved by forming guanin triphosphate (GTP) and by converting the coenzymes NAD^+ and FAD to their reduced forms NADH and $FADH_2$, which are used in the respiratory chain at the inner membrane of the mitochondria to drive the phosphorylation of ADP (subsection 2.3.1).

[2] *Sir Hans Adolf Krebs* (1900–1981): German-born British physician and biochemist, who earned the Nobel Prize in Physiology or Medicine in 1953 together with *Fritz Albert Lipmann* for the identification of the citric-acid cycle (1937).

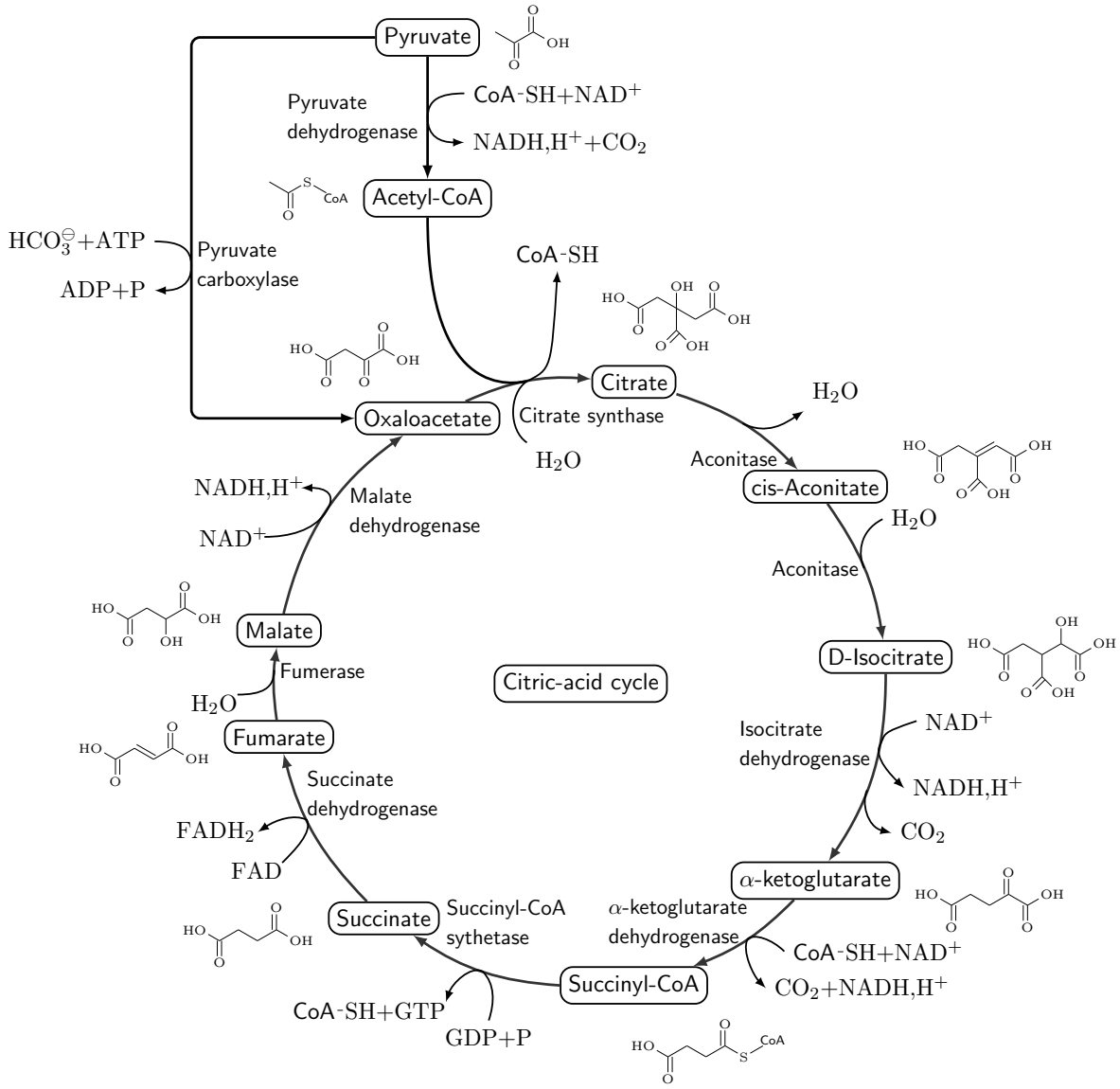

Figure 2.3.: Reactions of the citric-acid cycle.

2.3.2. Glycolysis

During glycolysis, glucose is converted in the cell cytoplasm into two molecules pyruvate following the *Embden*[3]-*Meyerhof*[4]-*Parnas*[5] pathway . It consists of a sequence of ten enzymatically catalysed reactions (Figure 2.4), which occur without the oxygen. During the

[3] *Gustav Georg Embden* (1874–1933): German biochemist, who laid the fundament for the understanding of diabetis mellitus.

[4] *Otto Fritz Meyerhof* (1884–1951) German-born physician and biochemist, who earned the Nobel Prize in Physiology or Medicine in 1922 with Archibald Vivian Hill for his work on muscle metabolism including glycolysis.

[5] *Jakub Karol Parnas* (1884–1949): Jewish-Polish–Soviet biochemist, known for his contribution to the discovery of the Embden-Meyerhof-Parnas pathway.

Table 2.1.: The individual steps of the citric-acid cycle and the ATP output of each step.

	Reaction	ATP (mol)
1	Acetyl-CoA + oxaloacetate ⟶ citrate	
2	Citrate ⟶ isocitrate	
3	Isocitrate ⟶ α-oxoglutarate, NADH	2.5
4	α-Oxoglutarate ⟶ succinyl-CoA, NADH	2.5
5	Succinyl-CoA ⟶ succinate, GTP	1
6	Succinate ⟶ fumerate, FADH	1.5
7	Fumerate ⟶ malate	
8	Malate ⟶ oxaloacetate, NADH	2.5
	Total ATP	10

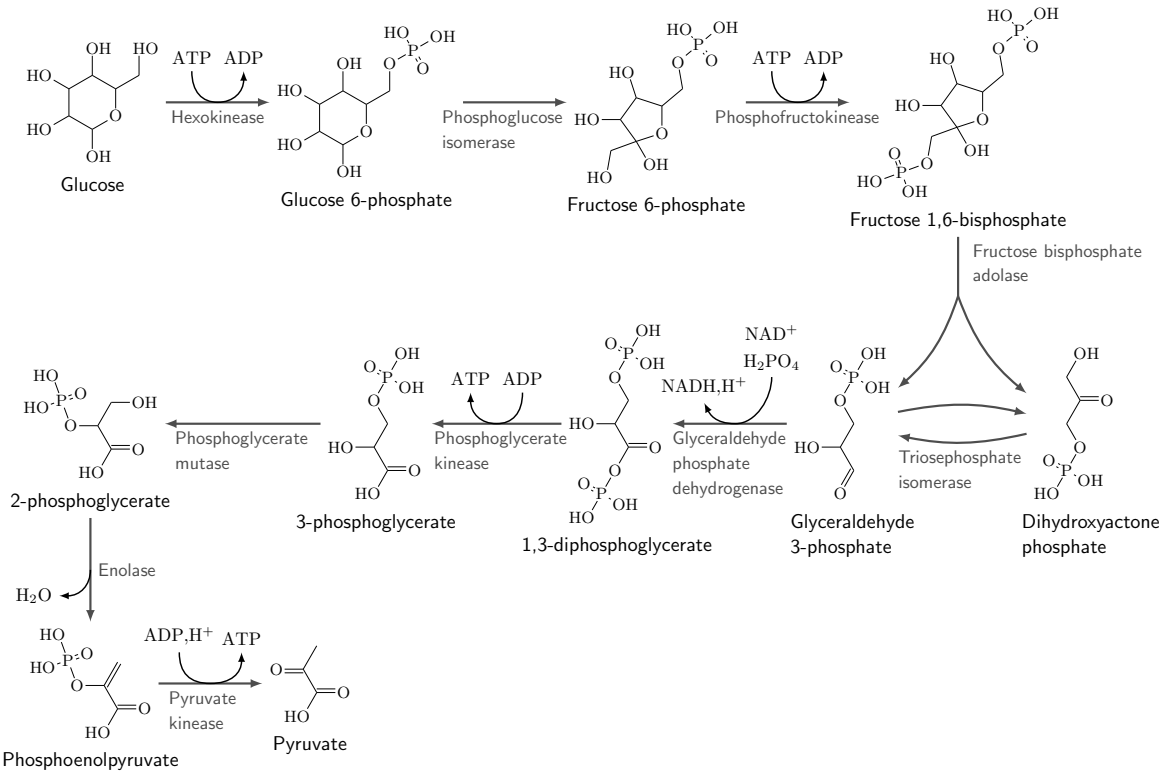

Figure 2.4.: Embden-Meyerhof-Parnas pathway.

first five reactions, glucose is split into two triosephosphate isomers, dihydroxyacetone and 3-phosphoglyceraldehyde. The phosphate groups needed for this reactions are obtained from two ATP molecules, which are hydrolysed to ADP. The resulting dihydroxyacetone phosphate are isomerised to 3-phosphoglyceraldehyde in a reversible reaction catalysed by the triosephosphate isomerase. In the following five reactions, the two triosephosphates are transformed to pyruvate. During glycolysis, in summary two ATP molecules and two

NADH molecules are synthesised per molecule glucose (Table 2.2).

Table 2.2.: The individual steps of the glycolysis and the ATP output of each step.

	Reaction	ATP (mol)
1	Glucose $\longrightarrow$ glucose 6-phosphate	-1.0
2	Glucose 6-phosphate $\longrightarrow$ fructose 6-phosphate	
3	Fructose 6-phosphate $\longrightarrow$ fructose 1,6-bisphosphate	-1.0
4	Fructose 1,6-bisphosphate $\longrightarrow$ 2(glyceraldehyde 3-phosphate)	
5	Glyceraldehyde 3-phosphate) $\longrightarrow$ 1,3-diphosphoglycerate, NADH	2×2.5 (2×1.5)
6	1,3-Diphosphoglycerate $\longrightarrow$ 3-phosphoglycerate, ATP	2×1
7	3-phosophglycerate $\longrightarrow$ 2-phosphoglycerate	
8	2-Phosphoglycerate $\longrightarrow$ phosphoenolpyruvate	
9	Phosphoenolpyruvate $\longrightarrow$ pyruvate, ATP	2×1
10	$\text{Pyruvate}_{\text{cyt}} \longrightarrow \text{Pyruvate}_{\text{mit}}$	-2×0.25
11	Pyruvate $\longrightarrow$ Acetyl-CoA, NADH	2×2.5
	Total ATP from Glycolysis	11.5 (9.5)
	ATP from citric-acid cycle	2×10
	Total ATP	31.5 (29.5)

If the aerobic pathway is taken, the electrons of the NADH molecules are transferred to the electron-transport chain at the inner membrane of the mitochondria, and thereby the NAD^+ needed for glycolysis is recovered. Therefore, the electrons must pass across the inner membrane. Depending on the cell type, the electrons are transferred either via the malate-aspartate shuttle or via the glycerol-phosphate shuttle. Using the malate-aspartate shuttle, the electrons are transferred into the mitochondria matrix by equilibrium reactions following the electro-chemical gradient across the membrane. In the inter-membrane space, NADH donates its electrons to malate, which passes the inner membrane via the malate-α-ketoglutarate antiporter and transfers the electrons to an NAD^+ molecule inside the mitochondria forming NADH. When transported with the glycerol-phosphate shuttle, the electrons are transferred to ubiquinone via FAD in an irreversible reaction. This results in a formation of only 1.5 ATP rather than 2.5 ATP.

Furthermore, the pyruvate molecules are transferred by a cotransport with one proton to the mitochondria matrix, where they are decarbonated to the acetyl-CoA and enter the citric-acid cycle. Following this, the oxidation of one glucose molecule leads to the synthesis of approximately 30 ATP.

In contrast to this, in anaerobic organisms and in the absence of oxygen, the NAD^+ needed to maintain the glycolysis are regenerated by transferring the electrons form NADH to pyruvate obtaining lactic acid or ethanol and CO_2. This anaerobic pathways are called fermentations and have an outcome of two ATP per glucose.

2.3.3. Fatty-acid oxidation

Fatty acids are carboxylic acids with an aliphatic, acyclic chain, i. e., the C atoms form a straight line without cycles. They are distinguished by the length of their chain, and the number and position of double bonds. Saturated fatty acids have no double bonds.

In the cytosol, the fatty acids form an acyl-CoA by reacting with coenzyme A. During this reaction ATP is hydrolysed to AMP. To pass the inner membrane, the coenzyme A is replaced by carnitine yielding an acyl-carnitine, which is shuttled by a transport protein. In the mitochondria matrix, the acyl-carnitine is reformed to the respective acyl-CoA, which is at the carboxyl end of the molecule progressively shortened by two carbon units, which are transferred to acetyl-CoA . This process consists of four reactions, which are repeated until the fatty acid is completely oxidised and produce one $FADH_2$ and one NADH. Both molecules enter the respiratory chain, which results in 5 ATP formed from ADP for every two-carbon unit removed as acetyl-CoA. Furthermore, the oxidation of each acetyl-CoA in the citric acid cycle yields 10 ATP. Following this, for every fatty acid a theoretical number of ATP synthesised from ADP during its degradation can be determined.

2.3.4. Amino-acid oxidation

Amino acids are characterised by an carboxylic acid and an amino group, linked to the α-carbon atom (Figure 2.5). At least twenty amino acids are found in proteins, each of them

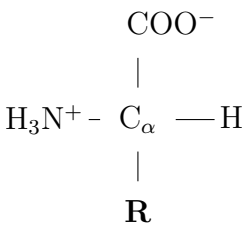

Figure 2.5.: General structure of an amino acid, characterised by amine H_3N^+ and a carboxylic acid COO^- linked to the same carbon atom (C_α). Each amino acid has an individual side chain **R**, which specifies its chemical properties.

has an individual side chain specifying its chemical properties. During their degradation, each amino acid follows an individual pathway all of them converging in the citric-acid cycle. For details concerning the degradation pathways refer to standard textbooks (e. g. Löffler, 2008, chap. 7).

In general, the degradation of amino acids can be separated into two steps. First, the amino acids are converted to the respective α-keto acid. To this end, the amino group of the amino acid is removed, either by transferring it to another α-keto acid, or by converting it to ammonia, which is then converted into urea. The latter, is located inside the liver and requires the dephosphorylation of two ATP molecules per amino group. In extrahepatic tissues (outside the liver), the amino groups are commonly transferred to

α-keto gluterate to form glutamate, which acts as main amino-group carrier in blood. Then, in a second step, the remaining keto acids are transferred to components that are able to enter the citric-acid cycle, either as intermediates of the cycle or as reactant. The ATP output of the oxidation of proteins is obtained by adding up the ATP obtained from the oxidation of its constituent amino acids as given in Table 2.3.

Table 2.3.: The yield of ATP on oxidation of amino acids to urea, carbon dioxide and water.

Amino acid	Molecular weight	Intermediary	ATP
Alanine	89.1	Pyruvate	15.5
Arginine	174.2	α-Oxoglutarate	28
Aspartate	133.1	α-Oxoglutarate	15.5
Aspargine	132.1	Oxaloacetate	13
Cysteine	121.1	Pyruvate	12.5
Glutamate	147.1	α-Oxoglutarate	24.5
Glutamine	146.2	α-Oxoglutarate	22
Glycine	75.1	(Serine) pyruvate	6
Histidine	155.2	α-Oxoglutarate	22.5
Isoleucine	131.2	Succinate & acetate	40.5
Leucin	131.2	Succinate & acetate	39.5
Lysine	146.2	(Crotonate) acetate	36
Methionine	149.2	Succinate	21.5
Phenylalanine	165.2	Fumarate	37.5
Proline	115.1	α-Oxoglutarate	29.5
Hydroxyproline	131.1	α-Oxoglutarate	26.5
Serine	105.1	Pyruvate	12.5
Threonine	119.1	Succinate	20.5
Tryptophan	204.2	(Crotonate) pyruvate	42
Tyrosine	181.2	Fumarate	41.5
Valine	117.1	Succinate	31.5

2.3.5. Further comments on the cellular metabolism

The metabolisation of glucose, fatty acids and amino acids follows strict metabolic pathways, which yield a specific number of ATP depending on the cell type and environmental conditions. For example, nervous tissue totally depends on the oxidation of glucoses. Moreover, red blood cells have no mitochondria. Hence, they can only use the anaerobic fermentation of glucoses for their ATP synthesis. Depending on the availability of oxygen, muscle cells switch between oxidation and fermentation. Also the outcome of the respiratory chain differs among the cells. Within brown adipose tissue, the protons return to the mitochondria matrix on an alternative route without synthesising ATP and

releasing the stored energy as heat. Following this, it is possible to determine energy amount synthesised by an individual cell type under specific conditions. However, the energy amount synthesised by another cell type under the same conditions might significantly differ. Moreover, also the energy amount synthesised by the same type but under differing conditions, might differ. Hence, if the digestible energy amount of a solute is to be determined on the organ or tissue scale, it is necessary to specify the considered cell types and conditions.

Chapter 3: Multiphasic materials, mixtures and solutions

By their nature, biological tissues are multiphasic porous materials, which are formed by several interacting components. To describe the mechanical behaviour of the overall biological material, it is necessary to consider its individual constituents. In this thesis, living tissues are modelled as multiphasic continua φ, which basically consist of superposed and interacting solid and fluid phases φ^α ($\alpha \in \{S, F\}$). In particular, the extracellular matrix and the adhering cells are summarised within the solid phase φ^S. These are surrounded by the extracellular liquids, which are subsumed in the fluid phase φ^F. However, the extracellular liquids are themselves homogeneous solutions, which contain several mixture components, i. e., $\varphi^F = \cup_\beta \varphi^\beta$ with $\beta \in \{L, \gamma\}$. In detail, these mixture components are divided into a solvent φ^L (liquid water) and several solutes φ^γ (nutrients, glucose, cell and matrix precursors, cell debris, etc.).

The immiscible solid and fluid phases yield a coupled fluid-structure interaction, which can be macroscopically described by using the framework of the Theory of Porous Media (TPM), as described by de Boer & Ehlers (1986), Bowen (1980, 1982) or Ehlers (1989, 2002, 2009). Thereby, the general thermodynamic framework of the Theory of Mixtures, developed by Truesdell & Toupin (1960) and Bowen (1976), is extended by the Concept of Volume Fractions.

3.1. Immiscible phases and volume fractions

Employing the TPM, it is not necessary to know the exact microstructure of biological tissue. Instead, the immiscible phases φ^α are described by their volume fractions $n^\alpha = \mathrm{d}v^\alpha/\mathrm{d}v$ (partial volume $\mathrm{d}v^\alpha$ per bulk volume $\mathrm{d}v$), which must fulfil the saturation constraint

$$\sum_\alpha n^\alpha = n^S + n^F = 1\,. \tag{3.1}$$

Therein, n^S is the solidity, and n^F is the porosity. Furthermore, the partial density $\rho^\alpha = \mathrm{d}m^\alpha/\mathrm{d}v$ (constituent mass element $\mathrm{d}m^\alpha$) and the material or realistic density $\rho^{\alpha R} = \mathrm{d}m^\alpha/\mathrm{d}v^\alpha$ are related to each other via the volume fraction n^α:

$$\rho^\alpha = n^\alpha \rho^{\alpha R}\,. \tag{3.2}$$

Summation over the partial densities ρ^α yields the density ρ of the overall aggregate:

$$\rho = \sum_\alpha \rho^\alpha = \rho^S + \rho^F\,. \tag{3.3}$$

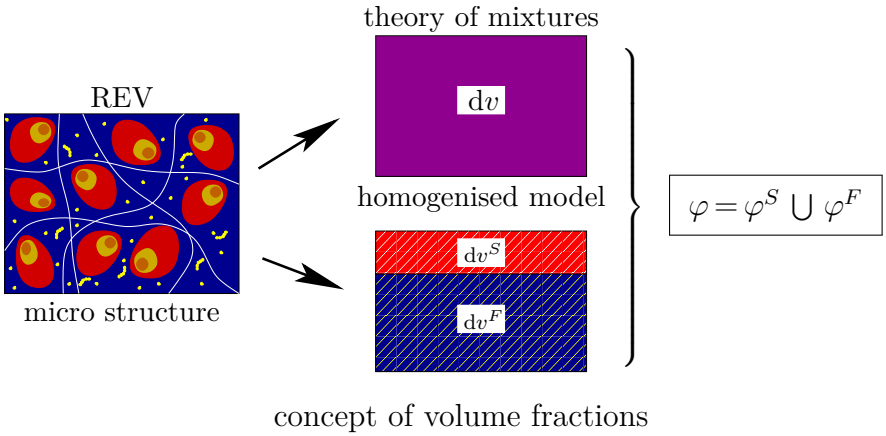

Figure 3.1.: Representative elementary volume (REV) of the biological microstructure and biphasic macro model.

3.2. Miscible components and concentration

The fluid phase is an ideal mixture that contains several miscible components φ^β. These are rather described by employing the molar concentrations c_m^β than their volume fractions, since they occupy the whole volume of the fluid phase φ^F. The molar concentrations relate the corresponding local number of moles $\mathrm{d}n_m^\beta$ to the local bulk fluid volume, i. e.,

$$c_m^\beta = \frac{\mathrm{d}n_m^\beta}{\mathrm{d}v^F} \,. \tag{3.4}$$

In addition, the corresponding partial densities of the fluid mixture components φ^β are defined via

$$\rho^\beta = n^F \rho_F^\beta \quad \text{with} \quad \rho_F^\beta = M_m^\beta \, c_m^\beta \,, \tag{3.5}$$

where ρ_F^β is the partial pore density, which relates the constituents' mass to the fluid volume, and M_m^β represents the constant molar mass of φ^β.

Summation over the partial densities ρ_F^β of the fluid mixture components yields the material density ρ^{FR} of the fluid phase, which, in the context of the Theory of Mixtures, can be interpreted as the fluid mixture density:

$$\rho^{FR} = \sum_\beta \rho_F^\beta \,. \tag{3.6}$$

3.3. Kinematic relations

The kinematics is based on the concept of superimposed continua (cf., e. g., Ehlers, 2002, 2009). Within this framework, each material point P^α is characterised by its position $\mathbf{X}_\alpha$ in the reference configuration at time $t = t_0$ and follows its individual motion function

$\mathbf{x} = \boldsymbol{\chi}_\alpha(\mathbf{X}_\alpha, t)$. Hence, each spatial point $\mathbf{x}$ is occupied at every time t by material points of all constituents, which have their own velocity fields

$$\mathbf{v}_\alpha = \overset{\prime}{\mathbf{x}}_\alpha = \frac{\mathrm{d}\,\boldsymbol{\chi}_\alpha(\mathbf{X}_\alpha, t)}{\mathrm{d}t} \quad \text{with} \quad (\cdot)'_\alpha = \frac{\mathrm{d}_\alpha}{\mathrm{d}t}(\cdot) = \frac{\partial\,(\cdot)}{\partial t} + \operatorname{grad}(\cdot)\cdot\mathbf{v}_\alpha\,, \tag{3.7}$$

where $\operatorname{grad}(\cdot) = \partial(\cdot)/\partial\mathbf{x}$. The motion of the solid constituent φ^S is given by the solid displacement vector $\mathbf{u}_S$, whereas the fluid motion is described relative to the deforming solid using the seepage velocity $\mathbf{w}_F$. Thus,

$$\mathbf{u}_S = \mathbf{x} - \mathbf{X}_S\,, \quad \mathbf{w}_F = \mathbf{v}_F - \mathbf{v}_S\,, \quad \text{where} \quad \mathbf{v}_S = (\mathbf{u}_S)'_S = \overset{\prime}{\mathbf{x}}_S\,. \tag{3.8}$$

Concerning the fluid components φ^β, the overall fluid velocity $\mathbf{v}_F$ as well as the mixture-component diffusion velocities $\mathbf{d}_{\beta F}$ and the corresponding seepage velocities $\mathbf{w}_\beta$ are given by

$$\mathbf{v}_F = \frac{1}{\rho^{FR}}\sum_\beta \rho_F^\beta \mathbf{v}_\beta\,, \quad \mathbf{d}_{\beta F} = \mathbf{v}_\beta - \mathbf{v}_F \quad \text{and} \quad \mathbf{w}_\beta = \mathbf{v}_\beta - \mathbf{v}_S\,. \tag{3.9}$$

Herein, $\mathbf{v}_\beta$ denotes the velocity of φ^β in analogy to (3.7). Moreover, the following relations hold:

$$(\,\cdot\,)'_F = (\,\cdot\,)'_S + \operatorname{grad}(\,\cdot\,)\cdot\mathbf{w}_F \quad \text{and} \quad (\,\cdot\,)'_\beta = (\,\cdot\,)'_S + \operatorname{grad}(\,\cdot\,)\cdot\mathbf{w}_\beta\,. \tag{3.10}$$

The deformation gradient $\mathbf{F}_\alpha$ and the spatial velocity gradient $\mathbf{L}_\alpha$ are introduced via

$$\mathbf{F}_\alpha = \frac{\partial\,\mathbf{x}}{\partial\mathbf{X}_\alpha} =: \operatorname{Grad}_\alpha\mathbf{x} \quad \text{and} \quad \mathbf{L}_\alpha = \frac{\partial\,\mathbf{v}}{\partial\mathbf{x}} = \operatorname{grad}\mathbf{v}_\alpha\,. \tag{3.11}$$

3.4. Balance equations

In this section, the constituent and overall balance equations of mass, momentum, moment of momentum (m. o. m.), energy and entropy are introduced. Following the "metaphysical principle" of the Theory of Mixtures formulated by Truesdell (1969, p. 83)[1] the balance equations of the overall medium and its constituents have the same structure as the balance equations of a single-phasic material. To describe each constituent by its own balance equations, the interaction among the constituents are included by additional production terms. Summing up the balance equations of the constituents yields the balance equation of the overall medium. The master-balance principle provides the general structure for all balance equations.

[1] *Clifford Ambrose Truesdell* (1919–2000): American mathematician, natural philosopher and historian of science. He was the founder and editor-in-chief of the journals Archive for Rational Mechanics and Analysis and Archive for History of Exact Sciences.

3.4.1. Master-balance equations

The global master balance equations of an arbitrary scalar- or vector-valued quantity Ψ or $\boldsymbol{\Psi}$ of the overall medium φ are introduced as

$$\begin{aligned} \frac{\mathrm{d}}{\mathrm{d}t}\int_{\mathcal{B}} \Psi \,\mathrm{d}v &= \int_{\mathcal{S}} (\boldsymbol{\phi}\cdot\mathbf{n})\,\mathrm{d}a + \int_{\mathcal{B}} \sigma \,\mathrm{d}v + \int_{\mathcal{B}} \hat{\Psi}\,\mathrm{d}v, \\ \frac{\mathrm{d}}{\mathrm{d}t}\int_{\mathcal{B}} \boldsymbol{\Psi} \,\mathrm{d}v &= \int_{\mathcal{S}} (\boldsymbol{\Phi}\mathbf{n})\,\mathrm{d}a + \int_{\mathcal{B}} \boldsymbol{\sigma} \,\mathrm{d}v + \int_{\mathcal{B}} \hat{\boldsymbol{\Psi}}\,\mathrm{d}v. \end{aligned} \tag{3.12}$$

Therein, the efflux of the physical quantity over the body's current surface $\mathcal{S}$ of $\mathcal{B}$ is denoted by $\boldsymbol{\phi}\cdot\mathbf{n}$ and $\boldsymbol{\Phi}\mathbf{n}$. The supply (external source) of the physical quantity per volume is described by σ and $\boldsymbol{\sigma}$. The terms $\hat{\Psi}$ and $\hat{\boldsymbol{\Psi}}$ represent the production of the quantity within the body $\mathcal{B}$.

Provided that all integrands in equation (3.12) are continuous and continuously differentiable, the local forms of the master balance equations are found by applying the divergence theorem (*Gauss*[2] theorem) on the surface integral and by differentiation of the left-hand side using the product rule (*Leibniz*'s[3] law),

$$\begin{aligned} \dot{\Psi} + \Psi \operatorname{div}\dot{\mathbf{x}} &= \operatorname{div}\boldsymbol{\phi} + \sigma + \hat{\Psi}, \\ \dot{\boldsymbol{\Psi}} + \boldsymbol{\Psi} \operatorname{div}\dot{\mathbf{x}} &= \operatorname{div}\boldsymbol{\Phi} + \boldsymbol{\sigma} + \hat{\boldsymbol{\Psi}}. \end{aligned} \tag{3.13}$$

For a detailed derivation of the local balance equations, refer to Ehlers (2002).

Analogously, the global master balance equations of an arbitrary scalar- or vector-valued quantity Ψ or $\boldsymbol{\Psi}$ of the constituent φ^α are introduced

$$\begin{aligned} \frac{\mathrm{d}_\alpha}{\mathrm{d}t}\int_{\mathcal{B}} \Psi^\alpha \,\mathrm{d}v &= \int_{\mathcal{S}} (\boldsymbol{\phi}^\alpha\cdot\mathbf{n})\,\mathrm{d}a + \int_{\mathcal{B}} \sigma^\alpha \,\mathrm{d}v + \int_{\mathcal{B}} \hat{\Psi}^\alpha\,\mathrm{d}v, \\ \frac{\mathrm{d}_\alpha}{\mathrm{d}t}\int_{\mathcal{B}} \boldsymbol{\Psi}^\alpha \,\mathrm{d}v &= \int_{\mathcal{S}} (\boldsymbol{\Phi}^\alpha\mathbf{n})\,\mathrm{d}a + \int_{\mathcal{B}} \boldsymbol{\sigma}^{\boldsymbol{\alpha}} \,\mathrm{d}v + \int_{\mathcal{B}} \hat{\boldsymbol{\Psi}}^{\alpha}\,\mathrm{d}v\,, \end{aligned} \tag{3.14}$$

where the quantities $(\cdot)^\alpha$ have the same physical meaning as the corresponding quantities $(\cdot)$ in (3.12). Then, employing the same algorithms as for the calculation of (3.13), the constituent local master balances can be found as

$$\begin{aligned} (\Psi^\alpha)'_\alpha + \Psi^\alpha \operatorname{div}\overset{\prime}{\mathbf{x}}_\alpha &= \operatorname{div}\boldsymbol{\phi}^\alpha + \sigma^\alpha + \hat{\Psi}^\alpha, \\ (\boldsymbol{\Psi}^\alpha)'_\alpha + \boldsymbol{\Psi}^\alpha \operatorname{div}\overset{\prime}{\mathbf{x}}_\alpha &= \operatorname{div}\boldsymbol{\Phi}^\alpha + \boldsymbol{\sigma}^\alpha + \hat{\boldsymbol{\Psi}}^{\alpha}. \end{aligned} \tag{3.15}$$

To guarantee that the overall balance equations (3.13) can be obtained by summation over all constituent balance equations, as postulated by Truesdell (1969, p. 83), the quantities of the balance relation are restricted by several summation constraints. For scalar-valued

[2] *Johann Carl Friedrich Gauss* (1777–1855): German mathematician and physical scientist, who contributed to many fields. Most of his work is about number theory and astronomy.

[3] *Gottfried Wilhelm von Leibniz* (1646–1716): German mathematician and philosopher, who contributed to many scientific fields. He is alleged to became a nobleman in 1711. However, no official document has been found that states this appointment.

quantities, these constraints are:

$$\Psi = \sum_{\alpha} \Psi^{\alpha}, \qquad \boldsymbol{\phi} \cdot \mathbf{n} = \sum_{\alpha} (\boldsymbol{\phi}_{\alpha} - \Psi^{\alpha} \mathbf{d}_{\alpha}) \cdot \mathbf{n}, \qquad \sigma = \sum_{\alpha} \sigma^{\alpha}, \qquad \hat{\Psi} = \sum_{\alpha} \hat{\Psi}_{\alpha} \,. \tag{3.16}$$

Analogous restrictions are obtained for the vector-valued quantities:

$$\boldsymbol{\Psi} = \sum_{\alpha} \boldsymbol{\Psi}^{\alpha}, \qquad \boldsymbol{\Phi}\mathbf{n} = \sum_{\alpha} (\boldsymbol{\Phi}_{\alpha} - \boldsymbol{\Psi}^{\alpha} \otimes \mathbf{d}_{\alpha})\mathbf{n}, \qquad \boldsymbol{\sigma} = \sum_{\alpha} \boldsymbol{\sigma}^{\alpha}, \qquad \hat{\boldsymbol{\Psi}} = \sum_{\alpha} \hat{\boldsymbol{\Psi}}_{\alpha}. \tag{3.17}$$

3.4.2. Balance equations of the overall medium

The balance equations of mass, momentum, moment of momentum, energy and entropy of the overall medium are axiomatically introduced. This results in the quantities summarised in Table 3.1. Therein, $\rho\dot{\mathbf{x}}$ is the momentum of the overall medium and $(\mathbf{x} \times \rho\dot{\mathbf{x}})$

Table 3.1.: Balance relations of the overall medium (Ehlers, 1996, 2002).

	$\Psi, \boldsymbol{\Psi}$	$\boldsymbol{\phi}, \boldsymbol{\Phi}$	$\sigma, \boldsymbol{\sigma}$	$\hat{\Psi}, \hat{\boldsymbol{\Psi}}$
mass	ρ	$\mathbf{0}$	0	0
momentum	$\rho\,\dot{\mathbf{x}}$	$\mathbf{T}$	$\rho\,\mathbf{b}$	$\mathbf{0}$
m. o. m.	$\mathbf{x} \times \rho\,\dot{\mathbf{x}}$	$\mathbf{x} \times \mathbf{T}$	$\mathbf{x} \times (\rho\,\mathbf{b})$	$\mathbf{0}$
energy	$\rho\,\varepsilon + \frac{1}{2}\rho\,\dot{\mathbf{x}} \cdot \dot{\mathbf{x}}$	$\mathbf{T}^T\dot{\mathbf{x}} - \mathbf{q}$	$\dot{\mathbf{x}} \cdot \rho\,\mathbf{b} + \rho r$	0
entropy	$\rho\,\eta$	$\boldsymbol{\phi}_{\eta}$	σ_{η}	$\hat{\eta}$

yields the moment of momentum. Furthermore, $\mathbf{T}$ denotes the *Cauchy*[4] stress tensor, which represents the external contact force $\mathbf{t} = \mathbf{T}\mathbf{n}$, and $\mathbf{b}$ represents the external mass-specific body forces, e. g., gravitation and electromagnetism. Within the balance of energy, ε is the mass-specific internal energy, the vector $\mathbf{q}$ denotes the heat influx, and r is the mass-specific external heat supply. The quantities within the balance of entropy are the mass-specific entropy η, the entropy efflux vector $\boldsymbol{\phi}_{\eta}$, the entropy supply σ_{η} and the entropy production $\hat{\eta}$, which must be greater or equal zero. Except for the entropy production, all production terms are equal to zero. Thus, the overall medium is regarded as a closed system.

By consecutively inserting the quantities given in Table 3.1 into the local master balance (3.13), starting with the mass balance and using the results obtained from lower balance

[4] *Baron Augustin-Louis Cauchy* (1789–1857): French mathematician and early pioneer of analysis. Sixteen concepts and theorems in elasticity are named after him.

equations, the specific local balance equations are obtained as

$$\begin{aligned} \dot{\rho} + \rho \operatorname{div} \dot{\mathbf{x}} &= 0, \\ \rho \ddot{\mathbf{x}} &= \operatorname{div} \mathbf{T} + \rho \mathbf{b}, \\ \mathbf{0} = \mathbf{I} \times \mathbf{T} \quad &\longrightarrow \quad \mathbf{T} = \mathbf{T}^T, \\ \rho \dot{\varepsilon} &= \mathbf{T} \cdot \mathbf{L} - \operatorname{div} \mathbf{q} + \rho r, \\ \rho \dot{\eta} &\geq \operatorname{div} \boldsymbol{\phi}_\eta + \sigma_\eta. \end{aligned} \tag{3.18}$$

The symmetry of the stress tensor $\mathbf{T}$ is a direct consequence of the local balance of moment of momentum.

3.4.3. Balance equations of the constituents

Following the metaphysical principles of Truesdell (1969), the local balance equations of the constituents are obtained analogously to those of the overall medium using the quantities summarised in Table 3.2. Therein, the quantities $(\cdot)^\alpha$ have the same physical meaning as the quantities $(\cdot)$ within Table 3.1. Moreover, the production terms allow for

Table 3.2.: Balance relations of the constituents (Ehlers, 1996, 2002).

	$\Psi^\alpha, \boldsymbol{\Psi}^\alpha$	$\boldsymbol{\phi}^\alpha, \boldsymbol{\Phi}^\alpha$	$\sigma^\alpha, \boldsymbol{\sigma}^\alpha$	$\hat{\Psi}^\alpha, \hat{\boldsymbol{\Psi}}^\alpha$
mass	ρ^α	$\mathbf{0}$	0	$\hat{\rho}^\alpha$
momentum	$\rho^\alpha \mathbf{v}_\alpha$	$\mathbf{T}^\alpha$	$\rho^\alpha \mathbf{b}^\alpha$	$\hat{\mathbf{s}}^\alpha$
m. o. m.	$\mathbf{x} \times \rho^\alpha \mathbf{v}_\alpha$	$\mathbf{x} \times \mathbf{T}^\alpha$	$\mathbf{x} \times (\rho^\alpha \mathbf{b}^\alpha)$	$\hat{\mathbf{h}}^\alpha$
energy	$\rho^\alpha \varepsilon^\alpha + \frac{1}{2}\rho^\alpha \mathbf{v}_\alpha \cdot \mathbf{v}_\alpha$	$(\mathbf{T}^\alpha)^T \mathbf{v}_\alpha - \mathbf{q}^\alpha$	$\mathbf{v}_\alpha \cdot \rho^\alpha \mathbf{b}^\alpha + \rho^\alpha r^\alpha$	$\hat{e}^\alpha$
entropy	$\rho^\alpha \eta^\alpha$	$\boldsymbol{\phi}_\eta^\alpha$	σ_η^α	$\hat{\eta}^\alpha$

an interaction among the constituents. In particular, $\hat{\rho}^\alpha$ denotes the mass production, $\hat{\mathbf{s}}^\alpha$ is the total momentum production, $\hat{\mathbf{h}}^\alpha$ represents the total angular momentum production, $\hat{e}^\alpha$ denotes the total energy production and $\hat{\eta}^\alpha$ is the total entropy production of φ^α.

Applying the same procedure as described in subsection 3.4.2, the local balance equations of the constituents are obtained by consecutively inserting the quantities given in Table 3.2

into the local master balance (3.15):

$$\begin{aligned}
(\rho^\alpha)'_\alpha + \rho \operatorname{div} \mathbf{v}_\alpha &= \hat{\rho}^\alpha, \\
\rho \overset{''}{\mathbf{x}}_\alpha &= \operatorname{div} \mathbf{T}^\alpha + \rho^\alpha \mathbf{b}^\alpha + \hat{\mathbf{p}}^\alpha, \\
\mathbf{0} &= \mathbf{I} \times \mathbf{T}^\alpha + \hat{\mathbf{m}}^\alpha, \\
\rho(\varepsilon^\alpha)'_\alpha &= \mathbf{T}^\alpha \cdot \mathbf{L}_\alpha - \operatorname{div} \mathbf{q}^\alpha + \rho^\alpha r^\alpha + \hat{\varepsilon}^\alpha, \\
\rho^\alpha(\eta^\alpha)'_\alpha &= \operatorname{div} \boldsymbol{\phi}_\eta^\alpha + \sigma_\eta^\alpha + \hat{\zeta}^\alpha.
\end{aligned} \tag{3.19}$$

In this equations, $\hat{\mathbf{p}}^\alpha$ and $\hat{\mathbf{m}}^\alpha$ are the direct production of momentum and angular momentum, while $\hat{\varepsilon}^\alpha$ and $\hat{\zeta}^\alpha$ are the direct production of energy and entropy. They describe the volume-specific local exchange of the correlated physical quantities among φ^α and the other constituents of φ and are obtained by dividing the respective total production terms into direct production terms and terms resulting from the production terms of the lower balance equations:

$$\begin{aligned}
\hat{\mathbf{s}}^\alpha &= \hat{\mathbf{p}}^\alpha + \hat{\rho}^\alpha \mathbf{v}_\alpha, \\
\hat{\mathbf{h}}^\alpha &= \hat{\mathbf{m}}^\alpha + \mathbf{x} \times (\hat{\mathbf{p}}^\alpha + \hat{\rho}^\alpha \mathbf{v}_\alpha), \\
\hat{e}^\alpha &= \hat{\varepsilon}^\alpha + \hat{\mathbf{p}}^\alpha \cdot \mathbf{v}_\alpha + \hat{\rho}^\alpha (\varepsilon^\alpha + \tfrac{1}{2} \mathbf{v}_\alpha \cdot \mathbf{v}_\alpha), \\
\hat{\eta}^\alpha &= \hat{\zeta}^\alpha + \hat{\rho}^\alpha \eta^\alpha.
\end{aligned} \tag{3.20}$$

Proceeding from a closed mixture system, the mass, moment, m. o. m. and energy of the overall aggregate are conserved and no material, moment or energy is generated or removed within the domain. Thus, the total productions must add up to zero, or to the overall entropy production, respectively. Therefore, the summation over the total production terms must satisfy the following summation constraints, which are obtained by inserting the respective quantities into $(3.16)_4$ or $(3.17)_{,4}$ respectively:

$$\sum_\alpha \hat{\rho}^\alpha = 0\,, \qquad \sum_\alpha \hat{\mathbf{s}}^\alpha = \mathbf{0}\,, \qquad \sum_\alpha \hat{\mathbf{h}}^\alpha = \mathbf{0}\,, \qquad \sum_\alpha \hat{e}^\alpha = 0\,, \qquad \sum_\alpha \hat{\eta}^\alpha \geq 0\,. \tag{3.21}$$

As mentioned before, the physical quantities of the overall aggregate are obtained by summation over the quantities of its constituents. Evaluation of (3.16) and (3.17) yields the relations among the overall quantities, given in Table 3.1, and the quantities of the

constituents, given in Table 3.2:

$$\begin{aligned}
\mathbf{T} &= \sum_\alpha (\mathbf{T}^\alpha - \rho^\alpha \mathbf{d}_\alpha \otimes \mathbf{d}_\alpha)\,, \\
\mathbf{b} &= \frac{1}{\rho}\sum_\alpha \rho^\alpha \mathbf{b}^\alpha\,, \\
\varepsilon &= \frac{1}{\rho}\sum_\alpha \rho^\alpha (\varepsilon^\alpha + \tfrac{1}{2}\mathbf{d}_\alpha \cdot \mathbf{d}_\alpha)\,, \\
\mathbf{q} &= \sum_\alpha [\mathbf{q}^\alpha - (\mathbf{T}^\alpha)^T \mathbf{d}_\alpha + \rho^\alpha \varepsilon^\alpha \mathbf{d}_\alpha + \tfrac{1}{2}\rho^\alpha (\mathbf{d}_\alpha \cdot \mathbf{d}_\alpha)\mathbf{d}_\alpha]\,, \\
r &= \frac{1}{\rho}\sum_\alpha \rho^\alpha (r^\alpha + \mathbf{b}^\alpha \cdot \mathbf{d}_\alpha)\,, \\
\eta &= \frac{1}{\rho}\sum_\alpha \rho^\alpha \eta^\alpha\,.
\end{aligned} \tag{3.22}$$

3.4.4. Entropy principle

The entropy inequality, also known as the second law of thermodynamics, is not required as a governing equation in a numerical scheme, but it provides the basis for the development of thermodynamical consistent material laws.

Here, the entropy efflux vector $\boldsymbol{\phi}_\eta^\alpha$ and the entropy supply σ_η^α of any constituent φ^α are introduced by the following a priori constitutive assumptions, (cf., e. g., Ehlers, 1996, 2002)

$$\boldsymbol{\phi}_\eta^\alpha = -\frac{1}{\theta^\alpha}\mathbf{q}^\alpha\,, \quad \sigma_\eta^\alpha = \frac{1}{\theta^\alpha}\rho^\alpha r^\alpha\,. \tag{3.23}$$

Therein, taking into consideration that any constituent could have its individual temperature, θ^α is the *Kelvin*'s[5] temperature of constituent φ^α. After inserting these assumptions together with relations (3.20) and (3.21) and summing up the constituent entropy balance $(3.19)_5$, the overall entropy inequality reads:

$$\sum_\alpha \Big[\rho^\alpha (\eta^\alpha)'_\alpha + \hat{\rho}^\alpha \eta^\alpha + \operatorname{div}\Big(\frac{1}{\theta^\alpha}\mathbf{q}^\alpha\Big) - \frac{1}{\theta^\alpha}\rho^\alpha r^\alpha\Big] \geq 0\,. \tag{3.24}$$

Reformulation of this inequality using the lower balance equations and the mass-specific *Helmholtz*[6] free energy, which results from a *Legendre*[7] transformation between the conjugated variables temperature θ^α and entropy η^α, via

$$\psi^\alpha = \varepsilon^\alpha - \theta^\alpha \eta^\alpha\,, \tag{3.25}$$

[5] *William Thomson, 1st Baron Kelvin* (1824–1907): British mathematical physicist and engineer, who became famous for correctly determining the correct value of absolute zero as approximately -273.15° *Celsius*.

[6] *Hermann Ludwig Ferdinand von Helmholtz* (1821–1894): German physician and physicist known for his theories on the conservation of energy, and works on a mechanical foundation of thermodynamics.

[7] *Adrien-Marie Legendre* (1752–1833): French mathematician known for the *Legendre* polynomial and the *Legendre* transformation, which are named after him.

yields the so-called *Clausius*[8]*-Duhem*[9] inequality

$$\sum_{\alpha} \frac{1}{\theta^{\alpha}} \Big[\mathbf{T}^{\alpha} \cdot \mathbf{L}_{\alpha} - \rho^{\alpha} [(\psi^{\alpha})_{\alpha} + (\theta^{\alpha})'_{\alpha} \eta^{\alpha}] - \hat{\mathbf{p}}^{\alpha} \cdot \mathbf{v}_{\alpha} - \\ - \hat{\rho}^{\alpha} (\psi^{\alpha} + \tfrac{1}{2} \mathbf{v}_{\alpha} \cdot \mathbf{v}_{\alpha}) - \frac{1}{\theta^{\alpha}} \mathbf{q}^{\alpha} \cdot \operatorname{grad} \theta^{\alpha} + \hat{e}^{\alpha} \Big] \geq 0 \,. \tag{3.26}$$

Proceeding from isothermal conditions, where all constituents have the same constant temperature θ, the entropy principle for mixtures yields (cf. Ehlers, 2002)

$$\sum_{\alpha} \Big[\mathbf{T}^{\alpha} \cdot \mathbf{L}_{\alpha} - \rho^{\alpha} (\psi^{\alpha})'_{\alpha} - \hat{\mathbf{p}}^{\alpha} \cdot \mathbf{v}_{\alpha} - \hat{\rho}^{\alpha} (\psi^{\alpha} + \tfrac{1}{2} \mathbf{v}_{\alpha} \cdot \mathbf{v}_{\alpha}) \Big] \geq 0 \,. \tag{3.27}$$

An alternative, more general evaluation procedure of the entropy principle is given by Müller (1985). Therein, the entropy inequality is used in its most general form $(3.18)_5$ and no a priori constitutive assumptions for the entropy flux and supply are introduced. Instead, since the entropy principle holds only for thermodynamic processes, the constituent balance equations act as additional constraints and are explicitly taken into account using *Lagrange*[10] multipliers (Müller, 1985, Section 6.3). Though this procedure provides a more general approach, it results in the same thermodynamic restrictions as the considered constitutive assumptions.

[8] *Rudolf Julius Emanuel Clausius* (1822–1888): German physicist and mathematician, who consider one of the central founders of thermodynamics.

[9] *Pierre Maurice Marie Duhem* (1861–1916) was a French physicist and philosopher of science, who contributed in the fields of hydrodynamics, elasticity, and thermodynamics.

[10] *Joseph-Louis Lagrange* (1736–1813): Italian mathematician and astronomer of the Enlightenment Era who founded analytical mechanics.

Chapter 4: Constitutive modelling

The framework introduced in the previous chapter is the theoretical basis for the description of various kinds of materials. Thereby, the diversity in the material behaviour is introduced via thermodynamically consistent constitutive assumptions for the partial *Cauchy* stress tensor $\mathbf{T}^\alpha$ as well as the volume production $\hat{n}^\alpha$ and the direct momentum production $\hat{\mathbf{p}}^\alpha$, which are necessary to close the continuum-mechanical problem. This allows for the consideration of multiphasic continua with an elastic (Eipper, 1998), a viscoelastic (Markert, 2005, 2008) or an elastoplastic (Blome, 2003; Mahnkopf, 2000) solid matrix with at least one compressible or incompressible interstitial fluid, which might have different temperatures (Graf, 2008). Furthermore, the inclusion of a charged solid and ionic fluids introduces swelling phenomena (Acartürk, 2009; Karajan, 2009).

The following two chapters focus on the thermodynamic restrictions imposed on the material under consideration. Thereby, it must be kept in mind that for specific applications only a small amount of relevant fluid components must be considered. In particular, this chapter is concerned with tailoring the general balance equations obtained in chapter 3 to the specific material under consideration. Additional modelling assumptions and restrictions are introduced. Instead of evaluating the entropy inequality directly, a general concept that reduces the number of solutes to a single non-mechanical quantity, and thereby also lowers the set of equations, is introduced in chapter 5. Employing the reduced set of equations, equivalent thermodynamic restrictions are determined and thermodynamically consistent material laws are introduced for the extracellular fluid φ^F and its components φ^β.

4.1. Modelling assumptions

The following considerations proceed from an isothermal ($\theta^\alpha \equiv \theta = \text{const.}$), biphasic material description under quasi-static conditions ($\overset{''}{\mathbf{x}}_\alpha = \ddot{\mathbf{x}} = \mathbf{0}$) with non-polar constituents ($\hat{\mathbf{m}}^\alpha \equiv \mathbf{0}$), where the fluid mixture φ^F and solid phase φ^S are both considered as materially incompressible ($\rho^{\alpha R} = \text{const.}$). Moreover, the fluid constituent is treated as a dilute solution that mainly consists of water with low concentrations of dissolved molecules. In particular, the mixture components are separated into the liquid solvent φ^L and several dissolved solutes φ^γ ($\gamma \in \{1, 2, \dots, N\}$ with N the number of considered solutes). Here, only those metabolites are considered explicitly which are contributing to the cellular energy metabolism. The remaining components of the extracellular fluid are assumed to be sufficiently available within the extracellular fluid solution such that they do not hinder the biological processes. They are considered implicitly as a part of the solvent φ^L. Moreover, it is assumed that the solute concentrations within the extracellular fluid

are marginal, such that their contribution to the fluid density is negligibly small[1]:

$$c_m^L \gg c_m^\gamma \quad \Longrightarrow \quad \rho^{FR} \approx \rho_F^L = \text{const.}\,, \quad \frac{\rho_F^\gamma}{\rho^{FR}} \approx 0 \quad \text{and} \quad \hat{\rho}^F \approx \hat{\rho}^L\,. \tag{4.1}$$

Inserting these assumptions into (3.9) and proceeding from moderate component velocities $\mathbf{v}_\gamma$ yields that the velocity of the solvent $\mathbf{v}_L$ is identical to the fluid velocity $\mathbf{v}_F$:

$$\mathbf{v}_L \approx \mathbf{v}_F \quad \Longrightarrow \quad \mathbf{d}_{LF} \approx \mathbf{0}\,. \tag{4.2}$$

Hence, the mechanical properties of the fluid mixture are assumed to be identical to those of the solvent.

4.2. Adaptation of the balance relations

The modelling assumptions introduced in the previous section are here incorporated into the balance equations introduced in Section 3.4. This adds additional restrictions, which must be obeyed by the model, and allows for rearrangements and further simplifications. To begin with, the assumption of non-polar materials ($\hat{\mathbf{m}}^\alpha \equiv \mathbf{0}$) reduces the constituent balance of moment of momentum $(3.19)_3$ to the statement that the partial *Cauchy* stress tensors must be symmetric, $\mathbf{T}^\alpha \equiv (\mathbf{T}^\alpha)^T$. Moreover, with the assumption of isothermal processes ($\theta^\alpha \equiv \theta = \text{const.}$), the balances of energy $(3.18)_4$ and $(3.19)_4$ loose their character as independent balance equations and are not used explicitly.

4.2.1. Volume balance and concentration balances

For materially incompressible phases, division of the mass balance $(3.19)_1$ by the constant material density $\rho^{\alpha R}$ leads to the constituent volume balance

$$(n^\alpha)'_\alpha + n^\alpha \operatorname{div} \mathbf{v}_\alpha = \hat{n}^\alpha \quad \text{with} \quad \hat{n}^\alpha \rho^{\alpha R} := \hat{\rho}^\alpha\,. \tag{4.3}$$

Therein, $\hat{n}^\alpha$ denotes the respective volume production, which in general does not add up to zero $\sum_\alpha \hat{n}^\alpha \neq 0$. Analytical integration of the solid volume balance leads to

$$n^S = \underbrace{n_{0S}^S \, \exp\Big(\int_{t_0}^t \frac{\hat{n}^S}{n^S} \mathrm{d}t\Big)}_{n_{tS}^S} (\det \mathbf{F}_S)^{-1} = n_{tS}^S (\det \mathbf{F}_S)^{-1}\,. \tag{4.4}$$

Therein, the solid volume fraction is multiplicatively split into a deformation-dependent part $(\det \mathbf{F}_S)^{-1}$ and a growth-dependent part n_{tS}^S. The quantity n_{0S}^S denotes the initial solid volume fraction at time $t = t_0$, while n_{tS}^S denotes the solid volume fraction at time $t \geq t_0$, associated with an accompanying reference configuration (cf. Humphrey &

[1] The extracellular fluid of a healthy person has a glucose concentration in the range of 4-6 mmol/l (cf. Löffler, 2008, p. 70), which is negligible compared to the molar concentration of the solvent water $c_m^L \approx 55$ mol/l.

Rajagopal, 2002) or an intermediate configuration (cf. Ambrosi & Guana, 2007; Ambrosi & Mollica, 2004). The time derivative of n_{tS}^{S} reads

$$(n_{tS}^{S})'_{S} = \hat{n}_{tS}^{S} := \hat{n}^{S} \det \mathbf{F}_{S} \,. \tag{4.5}$$

For a detailed derivation, please refer to Appendix A.

By adding the volume balances of the fluid and solid phases, the overall volume balance is obtained as

$$(n^{S})'_{S} + (n^{F})'_{S} + n^{S} \operatorname{div} \mathbf{v}_{S} + n^{F} \operatorname{div} \mathbf{v}_{F} + \operatorname{grad} n^{F} \cdot \mathbf{w}_{F} = \hat{n}^{S} + \hat{n}^{F} \,, \tag{4.6}$$

where $(3.10)_1$ was used to transfer the time derivative $(n^{F})'_{F}$ to a derivative with respect to the moving solid. By using the summation constraint $(3.21)_1$ and the time derivative of the saturation constraint (3.1),

$$n^{S} + n^{F} = 1 \quad \longrightarrow \quad (n^{S})'_{S} + (n^{F})'_{S} = 0 \,, \tag{4.7}$$

and inserting the divergence theorem

$$\operatorname{div}(\mathbf{v}_{S} + n^{F}\mathbf{w}_{F}) = n^{S} \operatorname{div} \mathbf{v}_{S} + n^{F} \operatorname{div} \mathbf{v}_{F} + \operatorname{grad} n^{F} \cdot \mathbf{w}_{F} \tag{4.8}$$

together with $(3.8)_3$, the final representation of the overall volume balance is obtained, viz:

$$\operatorname{div}[(\mathbf{u}_{S})'_{S} + n^{F}\mathbf{w}_{F}] = \hat{n}^{S}\Big(1 - \frac{\rho^{SR}}{\rho^{FR}}\Big) \,. \tag{4.9}$$

Concerning the constituents of the fluid phase, it is possible to rewrite the mass balance $(3.19)_1$ employing the partial density ρ_{F}^{β}:

$$(n^{F})'_{\beta}\rho_{F}^{\beta} + n^{F}(\rho_{F}^{\beta})'_{\beta} + n^{F}\rho_{F}^{\beta} \operatorname{div} \mathbf{v}_{\beta} = n^{F}\hat{\rho}_{F}^{\beta} \quad \text{with} \quad \hat{\rho}^{\beta} =: n^{F}\hat{\rho}_{F}^{\beta} \,. \tag{4.10}$$

4.2.2. Momentum balances

Proceeding from quasi-static conditions, the constituent momentum balance equation $(3.19)_2$ reads

$$\mathbf{0} = \operatorname{div} \mathbf{T}^{\alpha} + \rho^{\alpha}\mathbf{b} + \hat{\mathbf{p}}^{\alpha} \,, \tag{4.11}$$

where, in addition, the external mass-specific body forces are assumed to be identical for all constituents ($\mathbf{b}^{\alpha} = \mathbf{b}$). Summation yields the momentum balance of the overall aggregate:

$$\mathbf{0} = \operatorname{div} \mathbf{T}^{S} + \operatorname{div} \mathbf{T}^{F} + (\rho^{S} + \rho^{F})\mathbf{b} + \hat{n}^{S}\rho^{SR}\mathbf{w}_{F} \,. \tag{4.12}$$

Therein, the summation constrained $(3.21)_3$ was incorporated via

$$\hat{\mathbf{p}}^{S} + \hat{\mathbf{p}}^{F} = \hat{n}^{S}\rho^{SR}\mathbf{w}_{F} \,, \quad \text{with} \quad \hat{\rho}^{F} = -\hat{\rho}^{S} \,. \tag{4.13}$$

4.2.3. Entropy inequality

Reformulation of (3.27) by taking into account that the fluid phase consists of several components and consideration of the summation constraints $(3.21)_1$ and $(3.21)_2$ yields the entropy inequality ($\beta \in \{L, \gamma\}$) as

$$\mathbf{T}^S \cdot \mathbf{L}_S - \rho^S (\psi^S)'_S + \sum_\beta \Big[\mathbf{T}^\beta \cdot \mathbf{L}_\beta - n^F \rho_F^\beta (\psi^\beta)'_\beta - \hat{\mathbf{p}}^\beta \cdot \mathbf{w}_\beta \Big] + \\ + n^F \hat{\rho}_F^L (\psi^S - \psi^L - \tfrac{1}{2} \mathbf{w}_F \cdot \mathbf{w}_F) - \sum_\gamma n^F \hat{\rho}_F^\gamma (\psi^\gamma - \tfrac{1}{2} \mathbf{v}_\gamma \cdot \mathbf{v}_\gamma) \geq 0 \,. \quad (4.14)$$

Furthermore, to guarantee the saturation constraint (3.1), its time derivative $\sum_\alpha (n^\alpha)'_S = 0$ is included into the entropy inequality (4.14) by employing the *Lagrange*an multiplier method, using a pressure-equivalent *Lagrange*an multiplier $\mathcal{P}$. The volume balance (4.6) together with (3.10) yields the saturation constraint

$$-\mathcal{P}(n^S + n^F)'_S = -\mathcal{P}\Big(\hat{n}^S + \hat{n}^F - n^S \operatorname{div} \mathbf{v}_S - n^F \operatorname{div} \mathbf{v}_F - \operatorname{grad} n^F \cdot \mathbf{w}_F \Big) = 0 \,. \quad (4.15)$$

4.2.4. Free Helmholtz energies

Within the fluid mixture, the *Helmholtz* free energies of the mixture components are defined per mixture volume rather than per mass (cf. Bowen, 1976). Therefore, the mass-specific quantities ψ^β are transferred to the volume-specific quantities Ψ_F^β (Ehlers, 2009):

$$\Psi_F^F = \sum_\beta \Psi_F^\beta = \sum_\beta \rho_F^\beta \psi^\beta \,. \quad (4.16)$$

The corresponding time derivatives yield

$$\begin{aligned} n^F \rho_F^\beta (\psi^\beta)'_\beta &= n^F (\Psi_F^\beta)'_\beta - n^F \psi^\beta (\rho_F^\beta)'_\beta \\ &= n^F (\Psi_F^\beta)'_\beta + n^F \Psi_F^\beta \operatorname{div} \mathbf{v}_S + n^F \Psi_F^\beta \operatorname{div} \mathbf{v}_\beta + \\ &\quad + \Psi_F^\beta \operatorname{grad} n^F \cdot \mathbf{w}_\beta - n^F \Psi_F^\beta \frac{\hat{\rho}_F^\beta}{\rho_F^\beta} - \Psi_F^\beta \hat{n}^S \end{aligned} \quad (4.17)$$

and

$$(\Psi_F^\beta)'_\beta = (\Psi_F^\beta)'_F + \operatorname{grad} \Psi_F^\beta \cdot \mathbf{d}_{\beta F} \,. \quad (4.18)$$

The *Helmholtz* free energy of the fluid mixture Ψ_F^F is obtained by summation over the *Helmholtz* free energies of the mixture components Ψ_F^β.

With these relations, the entropy inequality of a biphasic material consisting of a porous solid φ^S saturated with a dilute solution φ^F composed of multiple solvents φ^γ dissolved

in a liquid solvent φ^L yields

$$\begin{aligned}
&\Big[\mathbf{T}^S + n^S\mathcal{P}\mathbf{I} - n^S\Psi_F^F\mathbf{I}\Big]\cdot\mathbf{L}_S - \rho^S(\psi^S)'_S + \\
&+\Big[\mathbf{T}^L + n^F\mathcal{P}\mathbf{I} - n^F\Psi_F^L\mathbf{I}\Big]\cdot\mathbf{L}_F - n^F(\Psi^F)'_F + \\
&+\sum_\gamma\Big[\mathbf{T}^\gamma - n^F\Psi_F^\gamma\,\mathbf{I}\Big]\cdot\mathbf{L}_\gamma - \Big[\hat{\mathbf{p}}^F - \mathcal{P}\operatorname{grad}n^F + \Psi_F^F\operatorname{grad}n^F\Big]\cdot\mathbf{w}_F - \\
&-\sum_\gamma\Big[\hat{\mathbf{p}}^\gamma + \Psi_F^\gamma\operatorname{grad}n^F + n^F\operatorname{grad}\Psi_F^\gamma\Big]\cdot\mathbf{d}_{\gamma F} - \sum_\gamma n^F\frac{\hat{\rho}_F^\gamma}{\rho_F^\gamma}\Big[\tfrac{1}{2}\rho_F^\gamma\mathbf{v}_\gamma\cdot\mathbf{v}_\gamma\Big] + \\
&+\hat{n}^F\rho^{FR}\Big[\psi^S - \frac{\Psi_F^L}{\rho^{SR}} - \sum_\gamma\Big(\frac{\Psi_F^\gamma}{\rho^{SR}}\Big) - \tfrac{1}{2}\mathbf{w}_F\cdot\mathbf{w}_F + \frac{\rho^{FR}-\rho^{SR}}{\rho^{FR}\rho^{SR}}\mathcal{P}\Big] \geq 0\,.
\end{aligned} \tag{4.19}$$

Following Ehlers (2009, eq. (116)), the fluid-component *Helmholtz* free energy Ψ_F^γ and the chemical potential μ^γ can be given as

$$\Psi_F^\gamma = \rho_F^\gamma\mu_0^\gamma + \rho_F^\gamma R^\gamma\theta\,(\ln\rho_F^\gamma - 1) \quad\text{and}\quad \mu^\gamma = \mu_0^\gamma + R^\gamma\theta\ln\rho_F^\gamma\,. \tag{4.20}$$

Therein, μ_0^γ denotes the mass-specific standard potential at a standard state, R^γ the specific gas constant and θ the uniform and constant temperature (isothermal conditions). Alternatively, it is possible to rewrite the chemical potential and the *Helmholtz* free energy in terms of the molar concentration.

4.3. Evaluation of the entropy principle

To further simplify the evaluation, the growth-energy concept is introduced. Therefore, an evaluation of the entropy inequality for biphasic porous materials with an interstitial fluid solution is not necessary in this thesis. However, the interested reader is referred to Appendix B.

However, instead of directly starting with the evaluation of the entropy principle, the growth-energy concept is introduced to allow for further simplifications.

Chapter 5: Growth-energy concept

Following the idea of Markert & Ehlers (2007), the vast amount of dissolved chemical molecules is summarised in one quantity: the growth energy $\mathcal{C}^F$. This concept is also known from the energy value on food labels. It is biologically motivated by the cellular energy metabolism, where the metabolisation of a certain substrate, i. e., the reactant of a metabolic reaction follows a fixed metabolic pathway and always yields the synthesis of the same amount of ATP.

5.1. Requirements

The growth energy is an artificial quantity that summarises multiple solutes by energetically summarising their contribution to the cellular energy metabolism. To obtain a physically meaningful quantity, several requirements must be met. In particular, these are simplicity, predictability, extensibility and divisibility. Therein, simplicity and predictability address the theoretical basis of the concept, and extensibility and divisibility are more concerned with its adaptability.

Simplicity

To provide a simple quantity, which is easily interpreted, the growth-energy must be free of redundant information. Thereby, the concept should leave the existing mixture quantities unaffected as far as possible. At least, the energetic quantities must be conserved, regarding the *Helmholtz* free energy, it must hold that

$$\Psi_F^F(\mathcal{C}^F) \equiv \Psi_F^F(\cup_\gamma \rho_F^\gamma) \quad \Longleftrightarrow \quad \Psi_F^{\mathcal{C}} \equiv \sum_\gamma \Psi_F^\gamma \,. \tag{5.1}$$

If only one solute is summarised within the growth energy, the results must be directly comparable to the results obtained by solving the original problem.

Predictability

The growth energy reflects the contributions of the fluid constituents. To obtain a predictable behaviour, the growth energy must be an increasing function of the partial densities of fluid constituents. Moreover, all spatial points with an identical composition of growth-energy constituents have the same growth energy

$$\forall \rho_F^\gamma(\mathbf{x}_1) \equiv \rho_F^\gamma(\mathbf{x}_2) \longrightarrow \mathcal{C}^F(\mathbf{x}_1) \equiv \mathcal{C}^F(\mathbf{x}_2) \,. \tag{5.2}$$

As a result, the following statements hold: if the partial densities of all growth-energy constituents at $\mathbf{x}_1$ are greater than or equal to the partial densities at $\mathbf{x}_2$, then also the

growth energy at $\mathbf{x}_1$ is greater than or equal to the growth energy at $\mathbf{x}_2$:

$$\forall \rho_F^\gamma(\mathbf{x}_1) \geq \rho_F^\gamma(\mathbf{x}_2) \longrightarrow \mathcal{C}^F(\mathbf{x}_1) \geq \mathcal{C}^F(\mathbf{x}_2)\,. \tag{5.3}$$

Furthermore, if the growth energy at $\mathbf{x}_1$ is greater than the growth energy at $\mathbf{x}_2$, then the partial density of at least one growth-energy component is at $\mathbf{x}_1$ greater than at $\mathbf{x}_2$:

$$\mathcal{C}^F(\mathbf{x}_1) > \mathcal{C}^F(\mathbf{x}_2) \longrightarrow \exists \rho_F^\gamma(\mathbf{x}_1) > \rho_F^\gamma(\mathbf{x}_2)\,. \tag{5.4}$$

In addition, to obtain the same thermodynamic restrictions, the growth energy must be at its thermodynamic equilibrium if all growth-energy constituents are at their thermodynamic equilibrium.

Extensibility

The growth energy is introduced in order to summarise the effect of the constituents of the extracellular fluid on the growth behaviour. Thereby, the contributions of cell compartments and the solutes of the cytosol are neglected. Nevertheless, to allow for an accurate description of the storage mechanisms within adipose tissue, muscles and liver employing the growth-energy concept, it is necessary to provide an extensible framework which is capable to include also the energy uptake of cells.

Recalling Section 2.2, the energy uptake follows the gradient of the chemical potential inside the membrane, which is generated by the difference between the chemical potential in the cytosol and the extracellular fluid. Thereby, the equilibrium is reached if the chemical potential of the transported molecules in the cytosol and the extracellular fluids are equal. Note that due to the complex interactions among the constituents of the cytosol, the partial densities or concentrations in the extracellular fluid and in the cytosol are in general not equivalent. This effect is increased by the storage mechanisms of cells, where nutrients are stored as macromolecules. Since these macromolecules are unable to pass the plasma membrane, the chemical energy of the cytosol exceeds the chemical energy of the extracellular fluids, even if only one metabolic pathway is considered, without hindering the nutrient uptake.

Divisibility

Although the growth-energy concept provides an integrated quantity, it is important to provide the possibility of dividing the overall growth-energy into several compartments. As mentioned in Section 2.3, cells gain energy from the metabolism of glucose, fatty acids and amino acids, which are transported to the cells via the extracellular fluids. Using the growth-energy concept, it must be possible to consider the different types of metabolites individually. Especially, if anaerobic conditions are considered, it is necessary to divide the growth-energy into metabolites that require aerobic conditions for their metabolism and metabolites that can be consumed without oxygen.

5.2. Temperature-equivalent growth energy

Markert & Ehlers (2007) introduced the growth energy as a temperature-equivalent quantity (cf. Ehlers *et al.*, 2009; Krause, 2008, for details), which acts as measure of the average amount of chemical energy available for cell metabolism. Following this concept, the growth energy $\mathcal{C}_\theta^\alpha$ is regarded in full analogy to the thermodynamic temperature θ^α, which measures the average kinetic energy of atoms. Furthermore, to be in line with continuum thermodynamics, an associated (conjugate) "configurational growth entropy" η_θ^α is introduced as a measure for the randomness in the distribution of matter analogously to the thermal entropy η^α. Following this concept, $\mathcal{C}_\theta^S$ is the growth energy calculated from the solutes within the cytosol and $\mathcal{C}_\theta^F$ is calculated from the constituents of the extracellular fluids. The thermodynamic restrictions obtained from the entropy principle are sufficiently fulfilled if the following proportionalities are met (Ehlers *et al.*, 2009):

$$\left.\begin{array}{ll} \hat{\varepsilon}_\theta^F & \propto (\mathcal{C}_\theta^S - \mathcal{C}_\theta^F) \\ \mathbf{j}_\theta^\alpha & \propto \operatorname{grad} \mathcal{C}_\theta^\alpha \end{array}\right\} \Longrightarrow \left\{\begin{array}{lll} \hat{\varepsilon}_\theta^F & = \tau_\theta^S n^S (\mathcal{C}_\theta^S - \mathcal{C}_\theta^F) & : \text{caloric interaction,} \\ \mathbf{j}_\theta^\alpha & = D_\theta^\alpha \operatorname{grad} \mathcal{C}_\theta^\alpha & : \text{enerqy diffusion.} \end{array}\right. \tag{5.5}$$

Therein, the fluid energy production $\hat{\varepsilon}_\theta^F$ results from the growth energy difference among the phases and represents the negative growth-energy uptake of the cells with τ_θ^S as the growth-energy absorption rate. Furthermore, $\mathbf{j}_\theta^\alpha$ denotes the growth-energy influx vector, analogous to the the heat influx vector $\mathbf{q}^\alpha$, with the growth-energy diffusion coefficient D_θ^α. Using a straight-forward definition for the chemical potential, e. g.

$$\mathcal{C}_\theta^F = f^\gamma \rho_F^\gamma \tag{5.6}$$

with the constant energy value f^γ would lead to wrong results regarding the growth energy uptake. Employing this definition, the energy uptake is at its equilibrium when the growth energy of the cytosol and the extracellular fluid are equivalent. However, following the discussion in Section 5.1, the chemical energy of the cytosol may exceed the chemical energy of the extracellular fluids without hindering the nutrient uptake. Herein, the restrictions in (5.5) differ from the realistic behaviour. This discrepancy obviously results from the inaccurate substitution of thermal temperature with a concentration-based growth energy. Recapitulation of the dependencies of the internal energy $\varepsilon^F = \varepsilon^F(\eta^F, n^F, \cup_\gamma \rho_F^\gamma)$ and its differential element

$$\mathrm{d}\varepsilon^F = \theta \mathrm{d}\eta^\alpha - p^F \mathrm{d}n^F + \sum_\gamma \mu_\rho^\gamma \mathrm{d}\rho_F^\gamma \tag{5.7}$$

reveals that the temperature is rather equivalent to the chemical potential μ_F^γ than to the partial density ρ_ρ^γ. Following this, it is possible to give an adequate definition for the temperature-equivalent growth-energy using the chemical potential, viz.,

$$\mathcal{C}_\theta^F = \sum_\gamma f_\mu^\gamma \mu^\gamma \,, \tag{5.8}$$

where again f_μ^γ is a constant energy value related to the chemical potential. This definition yields adequate restrictions for the growth-energy diffusion and for the caloric interaction.

At equilibrium, the value of the growth energy in both phases is equal. However, as a drawback, the growth energy is no longer directly related to the energy content of the phases, and following the idea of conjugated "configurational growth entropy" $\eta_{\mathcal{C}}^{\alpha}$, the concentrations of the growth-energy constituents must be included in the definition of $\eta_{\mathcal{C}}^{\alpha}$. Thereby a definition must be found, such that the differential relation $\mathcal{C}_{\theta}^{F} = \partial\Psi_{F}^{\mathcal{C}}/\partial\eta_{\theta}^{F}$ hold. Considering only one growth-energy constituent the "configurational growth entropy" is defined as

$$\eta_{\theta}^{F} = \frac{\rho_{F}^{\gamma}}{f_{\mu}^{\gamma}} \,. \tag{5.9}$$

Proof: Inserting (5.9) into restriction (5.1) together with (4.20) yields:

$$\Psi_{F}^{\gamma} = \rho_{F}^{\gamma}\mu_{0}^{\gamma} + \rho_{F}^{\gamma}R^{\gamma}\theta\,(\ln\rho_{F}^{\gamma} - 1) = \eta_{\theta}^{F}f_{\mu}^{\gamma}\mu_{0}^{\gamma} + \eta_{\theta}^{F}f_{\mu}^{\gamma}R^{\gamma}\theta\,(\ln(\eta_{\theta}^{F}f_{\mu}^{\gamma}) - 1) = \Psi_{F}^{\mathcal{C}} \,. \tag{5.10}$$

Then, differentiation with respect to η_{θ}^{α} yields the growth energy:

$$\mathcal{C}_{\theta}^{F} = \frac{\partial\,,\Psi_{F}^{\mathcal{C}}}{\partial\eta_{\theta}^{\alpha}} = f^{\gamma}\mu_{0}^{\gamma} + f_{\mu}^{\gamma}R^{\gamma}\theta\ln(\eta_{\alpha}^{F}f_{\mu}^{\gamma}) = f_{\mu}^{\gamma}\mu^{\gamma} \,. \tag{5.11}$$

■

If multiple growth energy constituents are considered, an adequate definition must be found. Nevertheless, following this concept finally leads to the question whether the entropy principle is still applicable and how the statement $\hat{\eta}_{\theta}^{\alpha} \geq 0$ should be interpreted. In order to avoid a discussion on the theoretical basis of rational thermodynamics, an alternative approach is chosen.

5.3. Concentration-equivalent growth energy

Instead of starting with an abstract definition as in the previous section (bottom-up), this section proceeds from a concrete definition for the growth energy (top-down), which follows the basic idea of Markert & Ehlers (2007) and summarises the energetic contribution of the vast amount of dissolved chemical molecules in one quantity. This is biologically motivated by the cellular energy metabolism, where the metabolisation of a certain substrate follows a fixed metabolic pathway and always yields the synthesis of a distinct amount of ATP, cf. Section 2.3. In analogy to the energy value on food labels, the growth energy $\mathcal{C}^{F}$ is obtained by summation over the fluid-component densities multiplied with the respective constant energy values f^{γ}, i. e., the amount of energy that is gained from the respective component by cell metabolism:

$$\mathcal{C}^{F} := \sum_{\gamma} f^{\gamma}\rho_{F}^{\gamma} =: f^{\mathcal{C}}\rho_{F}^{\mathcal{C}} \quad \text{with} \quad \rho_{F}^{\mathcal{C}} = \sum_{\gamma}\rho_{F}^{\gamma} \quad \text{and} \quad f^{\mathcal{C}} = \frac{\mathcal{C}^{F}}{\rho_{F}^{\mathcal{C}}} \,. \tag{5.12}$$

Therein, we interpret $\rho_{F}^{\mathcal{C}}$ as the total growth-energy density per pore-fluid volume and $f^{\mathcal{C}}$ as the averaged energy value of all growth-energy components.

Those nutrients of the extracellular fluid, which are converted to or used as energy, are weighted with a positive energy value and treated as growth-energy components. The remaining components of the extracellular fluid are weighted with an energy value of zero.

Proceeding from here, it postulated that the metaphysical principles formulated by Truesdell (1969) for mixture are also applicable on the growth energy. Hence, the motion of the growth energy is governed by equations equivalent to those of a single constituent. Furthermore, all properties of the growth energy are consequences of the properties of its constituents. However, in contrast to the Theory of Mixtures, the properties of the growth-energy are not determined by averaging the constituents masses, but by averaging over the energy content of each constituent.

Therefore, the growth-energy properties are, in the preceding, introduced as properties of a single component and then their relation to the properties of the growth-energy constituents is specified. Thereby, it must be kept in mind that the growth-energy constituents obey the restrictions introduced in chapter 4, whereas regarding the growth-energy, new restrictions will be introduced in this chapter. Thereby, following the metaphysical principles, these restrictions must as well result from the restrictions in chapter 4.

Growth-energy balance

With definition (5.12), the growth-energy balance is obtained by summation over the mass balances of the growth-energy components φ^γ weighted by the respective energy values f^γ:

$$\sum_\gamma \left[(n^F f^\gamma \rho_F^\gamma)'_\gamma + n^F f^\gamma \rho_F^\gamma \operatorname{div} \mathbf{v}_\gamma \right] = \sum_\gamma n^F f^\gamma \hat{\rho}_F^\gamma \quad \text{with} \quad f^\gamma = \text{const.} \tag{5.13}$$

Hence, the growth-energy balance has the same structure as a mass balance reading

$$(n^F \mathcal{C}^F)'_\mathcal{C} + n^F \mathcal{C}^F \operatorname{div} \mathbf{v}_\mathcal{C} = \hat{\mathcal{C}}^F \quad \text{with} \quad (\cdot)'_\mathcal{C} = \frac{\mathrm{d}_\mathcal{C}}{\mathrm{d}t}(\cdot) = \frac{\partial(\cdot)}{\partial t} + \operatorname{grad}(\cdot) \cdot \mathbf{v}_\mathcal{C} \,. \tag{5.14}$$

Therein, the growth-energy velocity $\mathbf{v}_\mathcal{C}$ and the growth-energy production $\hat{\mathcal{C}}^F$ are defined as

$$\mathbf{v}_\mathcal{C} := \mathbf{d}_{\mathcal{C}F} + \mathbf{v}_F = \frac{1}{\mathcal{C}^F} \sum_\gamma f^\gamma \rho_F^\gamma \mathbf{v}_\gamma \quad \text{and} \quad \hat{\mathcal{C}}^F := n^F \sum_\gamma f^\gamma \hat{\rho}_F^\gamma \tag{5.15}$$

with the growth-energy diffusion velocity $\mathbf{d}_{\mathcal{C}F}$. The growth-energy quantities are obtained by averaging over the energy content $(f^\gamma \rho_F^\gamma)$ of the growth-energy components and not over their density ρ_F^γ.

The growth-energy production summarises the growth-energy consumption of the cells. In contrast to the overall mass production, the growth-energy production $\hat{\mathcal{C}}^F$ is in general not equal to zero. A negative growth-energy production indicates nutrient consumption, and a positive production indicates nutrient production (e. g., photosynthesis). This does not contradict the summation constraint of the constituent mass productions $(3.21)_1$, as the growth-energy production is obtained by a mass-preserving transfer among metabolic

components with different energy values. For example, cells gain energy by metabolising glucose, a molecule with a high energy value, into water and carbon dioxide, molecules that have no energy value at all.

Growth-energy momentum balance

Following the preceding, the momentum balances of the growth-energy components are compiled in an equivalent balance equation for the growth energy:

$$\mathbf{0} = \operatorname{div} \mathbf{T}^{\mathcal{C}} + n^F \rho_F^{\mathcal{C}} \mathbf{b}^{\mathcal{C}} + \hat{\mathbf{p}}^{\mathcal{C}} \,. \tag{5.16}$$

Herein, the averaged quantities are related to the quantities of the growth-energy components via

$$\begin{aligned} \mathbf{T}^{\mathcal{C}} &:= \sum_{\gamma} \Big[\frac{f^\gamma}{f^{\mathcal{C}}} \mathbf{T}^\gamma - n^F \frac{f^\gamma \rho_F^\gamma}{f^{\mathcal{C}}} \, \mathbf{d}_{\gamma\mathcal{C}} \otimes \mathbf{d}_{\gamma\mathcal{C}} \Big] \,, \\ n^F \rho_F^{\mathcal{C}} \mathbf{b}^{\mathcal{C}} &:= \sum_{\gamma} n^F \frac{f^\gamma \rho_F^\gamma}{f^{\mathcal{C}}} \mathbf{b}^\gamma \,, \\ \hat{\mathbf{p}}^{\mathcal{C}} &:= \sum_{\gamma} \Big[\frac{f^\gamma}{f^{\mathcal{C}}} \hat{\mathbf{p}}^\gamma + n^F \frac{f^\gamma \hat{\rho}_F^\gamma}{f^{\mathcal{C}}} \mathbf{d}_{\gamma\mathcal{C}} \Big] \,. \end{aligned} \tag{5.17}$$

In analogy to the diffusion velocity in mixtures, the diffusion velocity equivalent $\mathbf{d}_{\gamma\mathcal{C}}$ of the growth-energy components is given as

$$\mathbf{d}_{\gamma\mathcal{C}} = \mathbf{v}_\gamma - \mathbf{v}_{\mathcal{C}} \quad \text{with} \quad \sum_{\gamma} f^\gamma \rho_F^\gamma \, \mathbf{d}_{\gamma\mathcal{C}} = \mathbf{0} \,. \tag{5.18}$$

Helmholtz free energy

To obtain the conceptual limitations and thermodynamic restrictions of the growth energy, additional quantities and balance relations must be introduced to allow for the evaluation of the entropy inequality (B.7) with respect to the growth energy. To begin with, the *Helmholtz* free energies ψ^γ of the growth-energy components are summarised by an equivalent holistic quantity $\psi^{\mathcal{C}}$. To this end, the individual *Helmholtz* free energies are weighted by the respective energy values yielding

$$\mathcal{C}^F \psi^{\mathcal{C}} := f^{\mathcal{C}} \Psi_F^{\mathcal{C}} := \sum_{\gamma} f^\gamma \Psi_F^\gamma = \sum_{\gamma} f^\gamma \rho_F^\gamma \psi^\gamma \,. \tag{5.19}$$

To obtain the summarised *Helmholtz* free energy, the *Helmholtz* free energy of the growth-

energy components (4.20) is inserted into (5.19) and reformulated:

$$\begin{aligned}\Psi_F^{\mathcal{C}} =& \frac{1}{f^{\mathcal{C}}} \sum_\gamma \Big[f^\gamma \rho_F^\gamma \mu_0^\gamma + f^\gamma \rho_F^\gamma R^\gamma \theta \left(\ln \rho_F^\gamma - 1 \right) \Big] \\ =& \frac{\rho_F^{\mathcal{C}}}{\mathcal{C}^F} \sum_\gamma \Big[f^\gamma \rho_F^\gamma \mu_0^\gamma + f^\gamma \rho_F^\gamma R^\gamma \theta \left(\ln \rho_F^\gamma - \ln \rho_F^{\mathcal{C}} + \ln \rho_F^{\mathcal{C}} - 1 \right) \Big] \\ =& \rho_F^{\mathcal{C}} \sum_\gamma \Big(\frac{f^\gamma \rho_F^\gamma}{\mathcal{C}^F} \mu_0^\gamma \Big) + \rho_F^{\mathcal{C}} \sum_\gamma \Big(\frac{f^\gamma \rho_F^\gamma}{\mathcal{C}^F} R^\gamma \Big) \theta \Big(\ln \rho_F^{\mathcal{C}} - 1 + \ln \frac{\rho_F^\gamma}{\rho_F^{\mathcal{C}}} \Big) \\ =& \rho_F^{\mathcal{C}} \mu_0^{\mathcal{C}} + \rho_F^{\mathcal{C}} R^{\mathcal{C}} \theta (\ln \rho_F^{\mathcal{C}} - 1) \,. \end{aligned} \tag{5.20}$$

Therein, the parameters $\mu_0^{\mathcal{C}}$ and $R^{\mathcal{C}}$ are identified as

$$\mu_0^{\mathcal{C}} := \frac{1}{\mathcal{C}^F} \sum_\gamma \Big[f^\gamma \rho_F^\gamma \Big(\mu_0^\gamma + R^\gamma \theta \ln \frac{\rho_F^\gamma}{\rho_F^{\mathcal{C}}} \Big) \Big] \quad \text{and} \quad R^{\mathcal{C}} := \frac{1}{\mathcal{C}^F} \sum_\gamma (f^\gamma \rho_F^\gamma R^\gamma) \,. \tag{5.21}$$

With this result, the growth-energy potential $\mu^{\mathcal{C}}$, which is thermodynamically conjugated to the growth energy, can either be calculated by differentiation of the overall *Helmholtz* free energy $\Psi_F^{\mathcal{C}}$ with respect to the growth energy or by summation over the chemical potentials of the growth energy components:

$$\mu^{\mathcal{C}} = \frac{\partial \Psi_F^F}{\partial \rho_F^{\mathcal{C}}} = \frac{\partial \Psi_F^{\mathcal{C}}}{\partial \rho_F^{\mathcal{C}}} = \mu_0^{\mathcal{C}} + R^{\mathcal{C}} \theta \ln \rho_F^{\mathcal{C}} = \frac{1}{\mathcal{C}^F} \sum_\gamma f^\gamma \rho_F^\gamma \mu^\gamma \,. \tag{5.22}$$

To guarantee that the standard growth-energy potential $\mu_0^{\mathcal{C}}$ and the specific-gas constant $R^{\mathcal{C}}$ are constants, the relation among the growth-energy components must remain constant, i. e.,

$$\frac{\rho_F^\gamma}{\rho_F^{\mathcal{C}}} = \text{const.} \tag{5.23}$$

In other words, if the densities of the growth-energy constituents are linear functions of the growth energy, then the growth-energy concept can be applied without loosing information. As a consequence of this requirement, the averaged energy value $f^{\mathcal{C}}$ becomes a constant.

$$f^{\mathcal{C}} = \frac{\mathcal{C}^F}{\rho_F^{\mathcal{C}}} = \frac{\sum_\gamma \rho_F^\gamma}{\rho_F^{\mathcal{C}}} = \sum_\gamma f^\gamma \frac{\rho_F^\gamma}{\rho_F^{\mathcal{C}}} = \text{const.} \tag{5.24}$$

The equations (5.23) and (5.24) restrict the growth energy concept. Only if (5.23) and (5.24) hold, the growth-energy concept gives equivalent results describing all constituents individually. Otherwise, the deviation form (5.23) and (5.24) can be used to determine the accuracy of the growth energy $\mathcal{C}^F$.

5.3.1. Evaluation of the entropy principle

For the evaluation of the entropy principle, the dependencies of the *Helmholtz* free energies must be included. The solid *Helmholtz* free energy ψ^S is assumed to be a function of the

solid deformation gradient $\mathbf{F}_S$ and, additionally, of the solid volume fraction n^S to account for the volume production governing the growth process. Furthermore, the growth-energy $\Psi_F^{\mathcal{C}}$ is a function of the partial growth-energy density $\rho_F^{\mathcal{C}}$. Hence, the dependencies of the *Helmholtz* free energies read:

$$\psi^S := \psi^S(\mathbf{F}_S, n^S) \quad \text{and} \quad \Psi_F^F := \Psi_F^F(\rho_F^{\mathcal{C}}) = \Psi_F^L + \Psi_F^{\mathcal{C}}(\rho_F^{\mathcal{C}}) = \Psi_F^L + \sum_{\gamma} \Psi_F^{\gamma}. \tag{5.25}$$

For a detailed derivation of the dependencies of the *Helmholtz* free energy, refer to Ehlers (2002, 2009) and the references therein. The time derivatives of the Helmholtz free energies used in the entropy inequality (4.14) are calculated by use of the chain rule:

$$\begin{aligned} \rho^S(\psi^S)'_S &= \rho^S \frac{\partial \psi^S}{\partial \mathbf{F}_S} \mathbf{F}_S^T \cdot \mathbf{L}_S + \rho^S \frac{\partial \psi^S}{\partial n^S} (n^S)'_S \,, \\ n^F(\Psi_F^F)'_F &= n^F \frac{\partial \Psi_F^F}{\partial \rho_F^{\mathcal{C}}} (\rho_F^{\mathcal{C}})'_F \,. \end{aligned} \tag{5.26}$$

Furthermore, the mass and volume balances (5.14) and (4.3) together with (3.10) are used to reformulate the local time derivatives $(n^S)'_S$ and $(\rho_F^{\mathcal{C}})'_F$:

$$\begin{aligned} (n^S)'_S =& - n^S \operatorname{div} \mathbf{v}_S + \hat{n}^S = -n^S \mathbf{L}_S \cdot \mathbf{I} + \hat{n}^S \,, \\ n^F(\rho_F^{\mathcal{C}})'_F =& - n^F \rho_F^{\mathcal{C}} \mathbf{L}_F \cdot \mathbf{I} - n^F \rho_F^{\mathcal{C}} \mathbf{L}_S \cdot \mathbf{I} + \hat{n}^F \rho_F^{\mathcal{C}} + n^F \frac{\hat{\mathcal{C}}^F}{f^{\mathcal{C}}} + \hat{n}^S \rho_F^{\mathcal{C}} - \\ & - \rho_F^{\mathcal{C}} \operatorname{grad} n^F \cdot \mathbf{w}_F - n^F \operatorname{grad} \rho_F^{\mathcal{C}} \cdot \mathbf{d}_{\mathcal{C}F} \,. \end{aligned} \tag{5.27}$$

The latter is obtained by reformulating (5.14):

$$\begin{aligned} n^F(\rho_F^{\mathcal{C}})'_F f^{\mathcal{C}} =& - n^F \mathcal{C}^F \operatorname{div} \mathbf{v}_{\mathcal{C}} + n^F \hat{\mathcal{C}}^F - n^F \operatorname{grad} \mathcal{C}^F \cdot \mathbf{d}_{\mathcal{C}F} - \mathcal{C}^F (n^F)'_{\mathcal{C}} \\ =& f^{\mathcal{C}} [-n^F \rho_F^{\mathcal{C}} \operatorname{div} \mathbf{v}_{\mathcal{C}} - n^S \rho_F^{\mathcal{C}} \operatorname{div} \mathbf{v}_S + n^F \frac{\hat{\mathcal{C}}^F}{f^{\mathcal{C}}} + \hat{n}^S \rho_F^{\mathcal{C}} - \\ & - \rho_F^{\mathcal{C}} \operatorname{grad} n^F \cdot \mathbf{w}_F - n^F \operatorname{grad} \rho_F^{\mathcal{C}} \cdot \mathbf{d}_{\mathcal{C}F} \,, \end{aligned} \tag{5.28}$$

where the derivative of the fluid volume fraction is reformulated using relation (3.10) and the saturation constraint (4.15):

$$(n^F)'_\beta = (n^F)'_S + \operatorname{grad} n^F \cdot \mathbf{w}_\beta = -(n^S)'_S + \operatorname{grad} n^F \cdot \mathbf{w}_\beta \,. \tag{5.29}$$

Concerning the solvent φ^L, after inserting (4.1) and (4.2) in $(5.27)_2$, the saturation constraint (4.15) reads:

$$n^F(\rho_F^L)'_F = -n^F \rho^{FR} \mathbf{L}_F \cdot \mathbf{I} - n^S \rho^{FR} \mathbf{L}_S \cdot \mathbf{I} + \hat{n}^F \rho^{FR} + \hat{n}^S \rho^{FR} - \rho^{FR} \operatorname{grad} n^F \cdot \mathbf{w}_F = 0 \,. \tag{5.30}$$

Following this, the entropy inequality yields:

$$
\begin{aligned}
&\Big[\mathbf{T}^S + n^S\mathcal{P}\mathbf{I} - \rho^S\frac{\partial\,\psi^S}{\partial\mathbf{F}_S}\,\mathbf{F}_S^T + \rho^{SR}(n^S)^2\frac{\partial\,\psi^S}{\partial n^S}\,\mathbf{I} - \\
&-n^S\Psi_F^F\,\mathbf{I} + n^S\rho_F^{\mathcal{C}}\frac{\partial\,\Psi_F^F}{\partial\rho_F^{\mathcal{C}}}\,\mathbf{I} + n^S\rho_F^L\frac{\partial\,\Psi_F^F}{\partial\rho_F^L}\,\mathbf{I}\Big]\cdot\mathbf{L}_S + \\
&+\Big[\mathbf{T}^L + n^F\mathcal{P}\mathbf{I} - n^F\Psi_F^L\mathbf{I} + n^F\rho_F^L\frac{\partial\,\Psi_F^F}{\partial\rho_F^L}\,\mathbf{I}\Big]\cdot\mathbf{L}_F + \\
&+\Big[\mathbf{T}^{\mathcal{C}} - n^F\Psi_F^{\mathcal{C}}\,\mathbf{I} + n^F\rho_F^{\mathcal{C}}\frac{\partial\,\Psi_F^F}{\partial\rho_F^{\mathcal{C}}}\,\mathbf{I}\Big]\cdot\mathbf{L}_{\mathcal{C}} - \\
&-\Big[\hat{\mathbf{p}}^F - \mathcal{P}\,\mathrm{grad}\,n^F + \Big(\Psi_F^F - \rho_F^{\mathcal{C}}\frac{\partial\,\Psi_F^F}{\partial\rho_F^{\mathcal{C}}} - \rho_F^L\frac{\partial\,\Psi_F^F}{\partial\rho_F^L}\Big)\,\mathrm{grad}\,n^F\Big]\cdot\mathbf{w}_F - \\
&-\Big[\hat{\mathbf{p}}^{\mathcal{C}} + \Big(\Psi_F^{\mathcal{C}} - \rho_F^{\mathcal{C}}\frac{\partial\,\Psi_F^F}{\partial\rho_F^{\mathcal{C}}}\Big)\,\mathrm{grad}\,n^F + n^F\,\mathrm{grad}\,\Psi_F^{\mathcal{C}} - n^F\frac{\partial\,\Psi_F^F}{\partial\rho_F^{\mathcal{C}}}\,\mathrm{grad}\,\rho_F^{\mathcal{C}}\Big]\cdot\mathbf{d}_{\mathcal{C}F} + \\
&+\Big[\psi^S - \frac{\Psi_F^L}{\rho^{SR}} + \frac{\Psi_F^L}{\rho^{FR}} + \frac{\rho_F^{\mathcal{C}}}{\rho^{SR}}\frac{\partial\,\Psi_F^F}{\partial\rho_F^{\mathcal{C}}} - \frac{\Psi_F^{\mathcal{C}}}{\rho^{SR}} - \tfrac{1}{2}\mathbf{w}_F\cdot\mathbf{w}_F + \\
&+\frac{\rho^{FR}-\rho^{SR}}{\rho^{FR}\rho^{SR}}\Big(\mathcal{P} + \rho^{FR}\frac{\partial\,\Psi_F^F}{\partial\rho_F^L}\Big) + \frac{1}{\rho^{SR}}\frac{\partial\,\psi^S}{\partial n^S}\Big]\hat{n}^F\rho^{FR} - \\
&-\Big[\rho_F^{\mathcal{C}}\frac{\partial\,\Psi_F^F}{\partial\rho_F^{\mathcal{C}}} - \rho_F^{\mathcal{C}}\mathbf{v}_{\mathcal{C}}\cdot\mathbf{v}_S + \tfrac{1}{2}\rho_F^{\mathcal{C}}\mathbf{v}_{\mathcal{C}}\cdot\mathbf{v}_{\mathcal{C}}\Big]n^F\frac{\hat{\mathcal{C}}^F}{\mathcal{C}_F} \geq 0\,.
\end{aligned}
\tag{5.31}
$$

Evaluation of this inequality leads to restrictions that must be fulfilled by thermodynamically consistent processes. The inequality as a whole is sufficiently fulfilled if each single term of the inequality fulfils the inequality itself, which is the standard evaluation procedure as described by Coleman & Noll (1963).

This entropy inequality slightly differs from the standard entropy inequality, which can be found in Appendix B (B.7). Due to the definition of $\mathbf{T}^{\mathcal{C}}$, cf. $(5.17)_1$, the third part of this inequality cannot be transferred to corresponding statement in the standard entropy inequality:

$$
\Big[\mathbf{T}^{\mathcal{C}} - n^F\Psi_F^{\mathcal{C}}\,\mathbf{I} + n^F\rho_F^{\mathcal{C}}\frac{\partial\,\Psi_F^F}{\partial\rho_F^{\mathcal{C}}}\,\mathbf{I}\Big]\cdot\mathbf{L}_{\mathcal{C}} \neq \sum_{\gamma}\Big[\mathbf{T}^{\gamma} - n^F\Psi_F^{\gamma}\,\mathbf{I} + n^F\rho_F^{\gamma}\frac{\partial\,\Psi_F^F}{\partial\rho_F^{\gamma}}\,\mathbf{I}\Big]\cdot\mathbf{L}_{\gamma} \tag{5.32}
$$

However, this statement is part of the equilibrium part of the entropy inequality, and thus, does not change the validity of the overall entropy inequality. Nevertheless, attention must be paid when the results obtained from this part of the inequality are interpreted.

5.3.2. Evaluation of the entropy principle

Following the evaluation procedure described by Coleman & Noll (1963), inequality (5.31) as a whole is sufficiently fulfilled if each single term of the inequality fulfils the inequality itself. To allow for a general evaluation independent from the process sequence, the variables depending on the process sequence, the velocity gradients $\mathbf{L}_S$, $\mathbf{L}_F$ and $\mathbf{L}_{\mathcal{C}}$, the

seepage and the filter velocities $\mathbf{d}_{\mathcal{C}F}$ and $\mathbf{w}_F$ as well as the production terms $\hat{n}^F$ and $\hat{\mathcal{C}}^F$, are allowed to have arbitrary values. As a consequence, the leading terms have to vanish or are chosen such that the products lead to positive values.

Growth-energy stress tensor

To begin with, the leading term in front of the velocity gradient $\mathbf{L}_{\mathcal{C}}$ is set equal to zero. Neglecting viscosity effects within the fluid mixture, the chemical potential tensor $\mathbf{K}^{\mathcal{C}}$ of the growth energy $\mathcal{C}^F$ is identified as

$$\mathbf{T}^{\mathcal{C}} - n^F \, \Psi_F^{\mathcal{C}} \, \mathbf{I} = -n^F \, \rho_F^{\mathcal{C}} \frac{\partial \, \Psi_F^{\mathcal{C}}}{\partial \rho_F^{\mathcal{C}}} \, \mathbf{I} = -n^F \, \rho_F^{\mathcal{C}} \, \mathbf{K}^{\mathcal{C}} \, . \tag{5.33}$$

Assuming a definition analogous to the definition of the chemical potential tensor given by Bowen (1967, eqs. (3.4) and (8.13)), the behaviour of the solutes is described by the scalar-valued growth-energy potential $\mu^{\mathcal{C}}$:

$$\mathbf{K}^{\gamma} = \mu^{\mathcal{C}} \, \mathbf{I} \quad \text{with} \quad \mu^{\mathcal{C}} = \frac{\partial \, \Psi_F^{\gamma}}{\partial \rho_F^{\mathcal{C}}} = \frac{\partial \, \Psi_F^{F}}{\partial \rho_F^{\mathcal{C}}} \, . \tag{5.34}$$

Following this, the growth-energy stress $\mathbf{T}^{\mathcal{C}}$ is identified by introducing the growth-energy osmotic pressure $\pi^{\mathcal{C}}$:

$$\mathbf{T}^{\mathcal{C}} = -n^F \pi^{\mathcal{C}} \mathbf{I} \quad \text{with} \quad \pi^{\mathcal{C}} = \rho_F^{\mathcal{C}} \mu^{\mathcal{C}} - \Psi_F^{\mathcal{C}} = \sum_{\gamma} \frac{f^{\gamma} \pi^{\gamma}}{f^{\mathcal{C}}} \, . \tag{5.35}$$

Therein, the growth-energy osmotic pressure is determined by summation over the osmotic pressures π^{γ} of the growth-energy components. Accordingly, the bracket term in front of $\mathbf{L}_{\mathcal{C}}$ in inequality (5.31) vanishes, and hence, the growth-energy velocity can take arbitrary values without violating the second law of thermodynamics.

Remark Alternatively, this result can be obtained by inserting the *Cauchy* stress tensors of the growth-energy constituents in $(5.17)_1$:

$$\mathbf{T}^{\gamma} = n^F \, \Psi_F^{\gamma} \, \mathbf{I} - n^F \, \rho_F^{\gamma} \, \mu^{\gamma} \, \mathbf{I} = -n^F \pi^{\gamma} \, \mathbf{I} \quad \text{with} \quad \pi^{\gamma} = \rho_F^{\gamma} \mu^{\gamma} - \Psi_F^{\gamma} \, . \tag{5.36}$$

Thereby, the *Cauchy* stress tensors of the growth-energy constituents are obtained from the evaluation of inequality (B.7) following the same procedure as described in this section and using the definition of the chemical potential tensor given by Bowen (1967, eqs. (3.4) and (8.13)):

$$\mathbf{K}^{\gamma} = \mu^{\gamma} \, \mathbf{I} \quad \text{with} \quad \mu^{\gamma} = \frac{\partial \, \Psi_F^{\gamma}}{\partial \rho_F^{\gamma}} = \frac{\partial \, \Psi_F^{F}}{\partial \rho_F^{\gamma}} \, . \tag{5.37}$$

Overall fluid pressure and solvent stress tensor

Concerning the liquid solvent, it can be shown by dimensional analysis that in porous-media flow the frictional stress is negligible compared to the influence of the momentum interaction describing the viscous drag in the pore channels (cf. Ehlers *et al.*, 1996; Markert, 2007). Thus, one finds the solvent *Cauchy* stress tensor

$$\mathbf{T}^L = -n^F \mathcal{P}\,\mathbf{I} - n^F \pi^L\,\mathbf{I} \quad \text{with} \quad \pi^L = \rho_F^L \frac{\partial\,\Psi_F^F}{\partial \rho_F^L} - \Psi_F^L\,. \tag{5.38}$$

Herein, the *Lagrange*an multiplier $\mathcal{P}$ can be identified as an growth-energy equivalent to the hydraulic pressure $\tilde{p}_0$. Furthermore, the effective fluid pressure p^{FR} is obtained by summation of the hydraulic pressure $\mathcal{P}$ and the overall osmotic pressure π:

$$p^{FR} = \mathcal{P} + \tilde{\pi} = \tilde{p}_0 + \tilde{\pi} \quad \text{with} \quad \tilde{\pi} = \pi^L + \pi^{\mathcal{C}}\,, \tag{5.39}$$

where π^L is the osmotic pressure of the solvent φ^L. However, note that, as a consequence of the chosen numerical scheme (cf. chapter 6), only the overall fluid pressure p^{FR} and the growth-energy osmotic pressure $\pi^{\mathcal{C}}$ can be determined exactly. The pressure of the liquid solvent $(\tilde{p}_0 + \pi^L)$ is determined by subtracting the growth-energy osmotic pressure $\pi^{\mathcal{C}}$ form the overall fluid pressure p^{FR}. Thereby, it must be taken into account that the growth-energy osmotic pressure $\pi^{\mathcal{C}}$ and therewith the growth-energy stress $\mathbf{T}^{\mathcal{C}}$ differ from the exact mechanical quantities obtained from the summation of the growth energy components, i. e.:

$$\pi^{\mathcal{C}} = \sum_{\gamma} \frac{f^\gamma \pi^\gamma}{f^{\mathcal{C}}} \neq \sum_{\gamma} \pi^\gamma\,. \tag{5.40}$$

As a consequence, also the values derived from this quantity (marked with a tilde $(\tilde{\cdot})$) $\tilde{\pi}$, $\tilde{p}_0$ and $\tilde{\mathbf{T}}^L$ do not correspond to the equivalent pressures that would be obtained without introducing the growth-energy concept.

With (5.36) and (5.38), the overall fluid *Cauchy* stress is then determined as

$$\mathbf{T}^F = \sum_{\beta} (\mathbf{T}^\beta - \rho_F^\beta \mathbf{d}_{\beta F} \otimes \mathbf{d}_{\beta F}) \approx -n^F (\tilde{p} + \pi^L + \pi^{\mathcal{C}}) \mathbf{I} = -n^F p^{FR} \mathbf{I}\,. \tag{5.41}$$

Therein, the terms containing diffusion velocities are neglected, due to the assumption of a dilute solution ($\rho_F^\gamma \approx 0$, $\mathbf{d}_{LF} \approx \mathbf{0}$), cf. (4.1).

Effective quantities

Following the concept of effective stresses (cf., de Boer & Ehlers, 1990), the solid and fluid *Cauchy* stress tensors and the direct momentum production are split into two parts. One part depending on the fluid pressure p^{FR} and an effective part $(\cdot)_E$, which is determined by constitutive equations, viz.:

$$\mathbf{T}^S = -n^S p^{FR} \mathbf{I} + \mathbf{T}_E^S\,, \quad \mathbf{T}^F = -n^F p^{FR} \mathbf{I} + \mathbf{T}_E^F \quad \text{and} \quad \hat{\mathbf{p}}^F = p^{FR} \operatorname{grad} n^F + \hat{\mathbf{p}}_E^F\,. \tag{5.42}$$

Applying an analogous splitting scheme, the quantities of fluid constituents are divided into an effective part, and a pressure-dependent part which contains the osmotic pressures π^L, $\pi^{\mathcal{C}}$ and the hydraulic pressure $\tilde{p}_0$:

$$\tilde{\mathbf{T}}^L = -n^F(\tilde{p}_0 + \pi^L)\mathbf{I} + \mathbf{T}^L_E\,, \quad \mathbf{T}^{\mathcal{C}} = -n^F\pi^{\mathcal{C}}\mathbf{I} + \mathbf{T}^{\mathcal{C}}_E \quad \text{and} \quad \hat{\mathbf{p}}^{\mathcal{C}} = \pi^{\mathcal{C}}\,\mathrm{grad}\,n^F + \hat{\mathbf{p}}^{\mathcal{C}}_E\,. \tag{5.43}$$

Solid stress tensors

Regarding growing biological tissue, it is convenient to split the solid effective stress tensor into a purely mechanical part $\mathbf{T}^S_{E/\mathrm{mech}}$ and a growth related part $\mathbf{T}^S_{E/\mathrm{grow}}$, viz.

$$\mathbf{T}^S_E = \overbrace{\rho^S \frac{\partial\,\psi^S}{\partial\mathbf{F}_S}\,\mathbf{F}_S^T}^{\mathbf{T}^S_{E/\mathrm{mech}}} \overbrace{-\rho^{SR}(n^S)^2\frac{\partial\,\psi^S}{\partial n^S}\,\mathbf{I}}^{\mathbf{T}^S_{E/\mathrm{grow}}}\,. \tag{5.44}$$

The choice of appropriate constitutive equations for both parts depends on the biological tissue under consideration. Two examples are presented in chapter 7, where the model is applied to avascular tumour tissue (Section 7.1) and hard osseous tissue (Section 7.2). Hence, the solid *Cauchy* stress $\mathbf{T}^S$ reads:

$$\mathbf{T}^S = \mathbf{T}^S_{E/\mathrm{mech}} + \mathbf{T}^S_{E/\mathrm{grow}} - n^S p^{FR}\mathbf{I}\,. \tag{5.45}$$

Inserting (5.45) and (5.41) in the overall momentum balance (4.12) yields its final form, which will be used in the numerical scheme

$$\mathbf{0} = \mathrm{div}(\mathbf{T}^S_{E/\mathrm{mech}} + \mathbf{T}^S_{E/\mathrm{grow}} - p^{FR}\mathbf{I}) + \hat{n}^S\rho^{SR}\mathbf{w}_F\,. \tag{5.46}$$

Momentum production

The previous constitutive relations have been obtained based on equilibrium considerations. The remaining terms of (5.31) represent the non-equilibrium contributions of the inequality. They represent the overall internal dissipation $\mathcal{D}$ of the thermodynamic process associated with the seepage flow $\mathcal{D}_{\mathbf{w}}$, the growth-energy diffusion $\mathcal{D}_{\mathbf{d}}$, the volume production (growth) $\mathcal{D}_n$ and the growth-energy production $\mathcal{D}_{\mathcal{C}}$. By use of this nomenclature, the

non-equilibrium part of the entropy inequality can be written as

$$\begin{aligned}
\mathcal{D} = &-\Big[\hat{\mathbf{p}}^F - \mathcal{P}\operatorname{grad} n^F + \Big(\Psi_F^F - \rho_F^{\mathcal{C}}\frac{\partial\,\Psi_F^F}{\partial\rho_F^{\mathcal{C}}} - \rho_F^L\frac{\partial\,\Psi_F^F}{\partial\rho_F^L}\Big)\operatorname{grad} n^F\Big]\cdot\mathbf{w}_F - \\
&-\Big[\hat{\mathbf{p}}^{\mathcal{C}} + \Big(\Psi_F^{\mathcal{C}} - \rho_F^{\mathcal{C}}\frac{\partial\,\Psi_F^F}{\partial\rho_F^{\mathcal{C}}}\Big)\operatorname{grad} n^F + n^F\operatorname{grad}\Psi_F^{\mathcal{C}} - n^F\frac{\partial\,\Psi_F^F}{\partial\rho_F^{\mathcal{C}}}\operatorname{grad}\rho_F^{\mathcal{C}}\Big]\cdot\mathbf{d}_{\mathcal{C}F} + \\
&+\Big[\psi^S - \frac{\Psi_F^L}{\rho^{SR}} + \frac{\rho_F^{\mathcal{C}}}{\rho^{SR}}\frac{\partial\,\Psi_F^F}{\partial\rho_F^{\mathcal{C}}} - \frac{\Psi_F^{\mathcal{C}}}{\rho^{SR}} - \tfrac{1}{2}\mathbf{w}_F\cdot\mathbf{w}_F + \\
&\qquad\qquad + \frac{\rho^{FR}-\rho^{SR}}{\rho^{FR}\rho^{SR}}\Big(\mathcal{P} + \rho^{FR}\frac{\partial\,\Psi_F^F}{\partial\rho_F^L}\Big) + \frac{1}{\rho^{SR}}\frac{\partial\,\psi^S}{\partial n^S}\Big]\hat{n}^F\rho^{FR} - \\
&-\Big[\rho_F^{\mathcal{C}}\frac{\partial\,\Psi_F^F}{\partial\rho_F^{\mathcal{C}}} - \rho_F^{\mathcal{C}}\mathbf{v}_{\mathcal{C}}\cdot\mathbf{v}_S + \tfrac{1}{2}\rho_F^{\mathcal{C}}\mathbf{v}_{\mathcal{C}}\cdot\mathbf{v}_{\mathcal{C}}\Big]n^F\frac{\hat{\mathcal{C}}^F}{\mathcal{C}_F} \\
= &\,\mathcal{D}_{\mathbf{w}} + \mathcal{D}_{\mathbf{d}} + \mathcal{D}_n + \mathcal{D}_{\mathcal{C}} \geq 0\,,
\end{aligned} \tag{5.47}$$

where

$$\begin{aligned}
\mathcal{D}_{\mathbf{w}} = &-\Big[\hat{\mathbf{p}}^F + \Big(-\mathcal{P} + \Psi_F^F - \rho_F^{\mathcal{C}}\frac{\partial\,\Psi_F^F}{\partial\rho_F^{\mathcal{C}}} - \rho_F^L\frac{\partial\,\Psi_F^F}{\partial\rho_F^L}\Big)\operatorname{grad} n^F\Big]\cdot\mathbf{w}_F \\
= &-(\hat{\mathbf{p}}^F - p^{FR}\operatorname{grad} n^F)\cdot\mathbf{w}_F\,,
\end{aligned}$$

$$\begin{aligned}
\mathcal{D}_{\mathbf{d}} = &-\Big[\hat{\mathbf{p}}^{\mathcal{C}} + \Big(\Psi_F^{\mathcal{C}} - \rho_F^{\mathcal{C}}\frac{\partial\,\Psi_F^F}{\partial\rho_F^{\mathcal{C}}}\Big)\operatorname{grad} n^F + n^F\operatorname{grad}\Psi_F^{\mathcal{C}} - \\
&\qquad - n^F\frac{\partial\,\Psi_F^F}{\partial\rho_F^{\mathcal{C}}}\operatorname{grad}\rho_F^{\mathcal{C}}\Big]\cdot\mathbf{d}_{\mathcal{C}F} \\
= &-[\hat{\mathbf{p}}^{\mathcal{C}} - \pi^{\mathcal{C}}\operatorname{grad} n^F]\cdot\mathbf{d}_{\mathcal{C}F}\,,
\end{aligned} \tag{5.48}$$

$$\begin{aligned}
\mathcal{D}_n = \hat{n}^F\rho^{FR}\Big[&\psi^S - \frac{\Psi_F^L}{\rho^{SR}} + \frac{\Psi_F^L}{\rho^{FR}} + \frac{\rho_F^{\mathcal{C}}}{\rho^{SR}}\frac{\partial\,\Psi_F^F}{\partial\rho_F^{\mathcal{C}}} - \frac{\Psi_F^{\mathcal{C}}}{\rho^{SR}} - \tfrac{1}{2}\mathbf{w}_F\cdot\mathbf{w}_F + \\
&+ \frac{\rho^{FR}-\rho^{SR}}{\rho^{FR}\rho^{SR}}\Big(\mathcal{P} + \rho^{FR}\frac{\partial\,\Psi_F^F}{\partial\rho_F^L}\Big) + \frac{1}{\rho^{SR}}\frac{\partial\,\psi^S}{\partial n^S}\Big]\,,
\end{aligned}$$

$$\mathcal{D}_{\mathcal{C}} = -\,n^F\frac{\hat{\mathcal{C}}^F}{\mathcal{C}_F}\Big[\rho_F^{\mathcal{C}}\frac{\partial\,\Psi_F^F}{\partial\rho_F^{\mathcal{C}}} - \rho_F^{\mathcal{C}}\mathbf{v}_{\mathcal{C}}\cdot\mathbf{v}_S + \tfrac{1}{2}\rho_F^{\mathcal{C}}\mathbf{v}_{\mathcal{C}}\cdot\mathbf{v}_{\mathcal{C}}\Big]\,.$$

The term $(5.48)_1$ is reformulated using the overall osmotic pressure $(5.39)_2$ with $(5.35)_2$ and $(5.38)_2$

$$\tilde{\pi} = \pi^L + \pi^{\mathcal{C}} = \rho_F^L\mu^L + \rho_F^{\mathcal{C}}\mu^{\mathcal{C}} - \Psi_F^F\,. \tag{5.49}$$

In $(5.48)_2$, the gradient of the *Helmholtz* free energy is evaluated by application of the chain rule, i. e.

$$n^F\operatorname{grad}\Psi_F^{\mathcal{C}} = n^F\frac{\partial\,\Psi_F^{\mathcal{C}}}{\partial\rho_F^{\mathcal{C}}}\operatorname{grad}\rho_F^{\mathcal{C}}\,. \tag{5.50}$$

Concerning the fluid and the growth-energy momentum productions, partial momentum productions $\hat{\mathbf{p}}^F_{E/\mathrm{mech}}$ and $\hat{\mathbf{p}}^{\mathcal{C}}_{\mathrm{mech}}$ are introduced. Thus, the pressure-dependent part is separated from the mechanical part of the production terms:

$$\hat{\mathbf{p}}^F_{E/\mathrm{mech}} := \hat{\mathbf{p}}^F - p^{FR}\operatorname{grad} n^F \quad \text{and} \quad \hat{\mathbf{p}}^{\mathcal{C}}_{\mathrm{mech}} := \hat{\mathbf{p}}^{\mathcal{C}} - \pi^{\mathcal{C}}\operatorname{grad} n^F\,. \tag{5.51}$$

Next, the individual contributions to the dissipation (5.47) are evaluated. Inserting the effective quantities into (5.47) yields thermodynamic restrictions for the constitutive choice of the mechanical part of the momentum productions:

$$\mathcal{D}_{\mathbf{w}} + \mathcal{D}_{\mathbf{d}} = -\hat{\mathbf{p}}^F_{E/\mathrm{mech}}\cdot\mathbf{w}_F - \hat{\mathbf{p}}^{\mathcal{C}}_{\mathrm{mech}}\cdot\mathbf{d}_{\mathcal{C}F} \geq 0\,. \tag{5.52}$$

Following Ehlers (2009), appropriate constitutive assumptions for the mechanical part of the momentum productions are given by

$$\hat{\mathbf{p}}^F_{E/\mathrm{mech}} = -(n^F)^2\frac{\mu^{FR}}{K^S}\mathbf{w}_F \quad \text{and} \quad \hat{\mathbf{p}}^{\mathcal{C}}_{\mathrm{mech}} = -(n^F)^2\frac{R^{\mathcal{C}}\theta\rho^{\mathcal{C}}_F}{D^{\mathcal{C}}}\mathbf{d}_{\mathcal{C}F}\,. \tag{5.53}$$

Therein, μ^{FR} denotes the effective fluid shear viscosity, K^S the intrinsic skeleton permeability and $D^{\mathcal{C}}$ the growth-energy diffusion coefficient.

Seepage velocity and growth-energy diffusion velocity

The seepage velocity is found by inserting the overall fluid *Cauchy* stress tensor (5.41) into the fluid momentum balance equation (4.11) $_{\alpha=F}$yielding the *Darcy*[1] filter law

$$n^F\mathbf{w}_F = -\frac{K^S}{\mu^{FR}}\operatorname{grad} p^{FR} = -\frac{k^F}{\gamma^{FR}}\operatorname{grad} p^{FR}\,, \tag{5.54}$$

where γ^{FR} is the effective fluid weight and k^F denotes the conventional hydraulic conductivity (*Darcy* permeability), which can be obtained from the intrinsic skeleton permeability K^S via

$$k^F := \frac{\gamma^{FR}}{\mu^{FR}}K^S\,. \tag{5.55}$$

Inserting the growth-energy stress $\mathbf{T}^{\mathcal{C}}$ (5.35) and the growth-energy momentum production $\hat{\mathbf{p}}^{\mathcal{C}}$ $(5.51)_2$ into (5.16) leads to

$$\mathbf{0} = n^F\operatorname{grad}(\Psi^{\mathcal{C}}_F - \rho^{\mathcal{C}}_F\mu^{\mathcal{C}}) - \pi^{\mathcal{C}}\operatorname{grad} n^F + \pi^{\mathcal{C}}\operatorname{grad} n^F + \hat{\mathbf{p}}^{\mathcal{C}}_E\,. \tag{5.56}$$

This relation in combination with (5.50) yields the conditional equation of the growth-energy diffusion velocity

$$n^F\rho^{\mathcal{C}}_F\,\mathbf{d}_{\mathcal{C}F} = -D^{\mathcal{C}}\operatorname{grad}\rho^{\mathcal{C}}_F\,, \tag{5.57}$$

which can be interpreted as a growth-energy equivalent to *Fick*'s[2] first law.

[1] *Henry Philibert Gaspard Darcy* (1803–1858): French engineer, who built the water supply system in Dijon and made several important contributions to hydraulics.

[2] *Adolf Eugen Fick* (1829–1901): German physician and physiologist, who introduced *Fick*'s law of

Mass and growth-energy production

The solid mass production describes the degenerative and regenerative processes that occur within a biological tissue. Both processes follow different metabolic pathways. Hence, they must be treated as individual processes with individual thermodynamic restrictions. The solid volume production is therefore additively split into one part that describes the degenerative process, $\hat{n}^S_{\mathrm{deg}}$, and another part that describes the regenerative process, $\hat{n}^S_{\mathrm{reg}}$. Thus,

$$\hat{n}^S = \hat{n}^S_{\mathrm{reg}} - \hat{n}^S_{\mathrm{deg}} \quad \text{with} \quad \hat{n}^S_{\mathrm{reg}} \geq 0 \quad \text{and} \quad \hat{n}^S_{\mathrm{deg}} \geq 0\,. \tag{5.58}$$

To obtain the associated restrictions, the entropy inequality must be evaluated for each process individually. Furthermore, it must be taken into account that the growth-energy production and the solid mass production depend on each other, i. e., if the tissue regenerates, more growth energy is consumed, and if no growth energy is available, no regenerative processes are possible. Consequently, the growth-energy production is additively split into a basal-metabolic part $\hat{\mathcal{C}}^F_{\mathrm{basal}}$, which depends on the amount of cells given by n^S, and an additional growth-dependent part $\hat{\mathcal{C}}^F_{\mathrm{grow}}$, which depends on the activity of the cells given by $\hat{n}^S$:

$$\hat{\mathcal{C}}^F = \hat{\mathcal{C}}^F_{\mathrm{basal}} + \hat{\mathcal{C}}^F_{\mathrm{grow}} \quad \text{with} \quad \left\{ \begin{array}{rcl} \hat{\mathcal{C}}^F_{\mathrm{basal}} & = & -k_{\mathrm{basal}}\, n^S\,, \\ \hat{\mathcal{C}}^F_{\mathrm{grow}} & = & -k_{\mathrm{grow}}\, \hat{n}^S_{\mathrm{reg}}. \end{array} \right. \tag{5.59}$$

Therein, the basal-metabolic part represents the growth-energy consumption of the tissue at quiescent state and the growth-dependent part accounts for the additional growth-energy consumption while the tissue is active and proliferating or remodelling.

Following the standard procedure, the thermodynamic restrictions of the solid volume production are found by inserting equation (5.59) into the entropy inequality. The *Gibbs* free enthalpies of the solid and the liquid solvent,

$$\xi^S = \psi^S + \frac{p^{FR}}{\rho^{SR}} + \frac{1}{\rho^{SR}} \frac{\partial\, \psi^S}{\partial n^S} \quad \text{and} \quad \xi^L = \frac{\Psi^L_F}{\rho^{FR}} + \frac{\mathcal{P} + \pi^L_F}{\rho^{FR}}\,, \tag{5.60}$$

are used to reformulate $(5.48)_3$. This leads to the dissipation inequality

$$\mathcal{D}_n = -\hat{n}^S_{\mathrm{deg}} \rho^{SR} [\xi^L - \xi^S - \tfrac{1}{2} \mathbf{w}_F \cdot \mathbf{w}_F] \geq 0\,. \tag{5.61}$$

Herein, the last term has to be considered if cell migration such as metastasis is taken into account. Concerning biological growth, the volume production is mainly a result of biochemical processes. Therefore, the direct influence of the seepage velocity is neglected in the following.

Analogously, the dissipation inequality yielding the restriction for the growth-energy production is obtained as

$$\mathcal{D}_{\mathcal{C}} = -\frac{\hat{\mathcal{C}}^F_{\mathrm{basal}}}{\mathcal{C}^F} [\rho^{\mathcal{C}}_F \mu^{\mathcal{C}} - \rho^{\mathcal{C}}_F \mathbf{v}_{\mathcal{C}} \cdot \mathbf{v}_S + \tfrac{1}{2} \rho^{\mathcal{C}}_F \mathbf{v}_{\mathcal{C}} \cdot \mathbf{v}_{\mathcal{C}}] \geq 0\,. \tag{5.62}$$

diffusion, which governs the diffusion of gas across a membrane.

Again, the influence of the velocity terms is assumed to be negligible. A positive dissipation rate is guaranteed by assuming the production terms to be proportional to the respective terms in brackets. This leads to

$$\hat{n}^S_{\mathrm{deg}} \propto \xi^S - \xi^L = \text{const.} \quad \text{and} \quad \hat{\mathcal{C}}^F_{\mathrm{basal}} \propto -\mu^{\mathcal{C}} \,. \tag{5.63}$$

Here, it is assumed that the growth-energy potential is always positive and the difference between the *Gibbs* free enthalpy of the solid and the fluid phase is a positive constant, since only small variations of pressure and temperature are physiologically meaningful. Following this, the negative basal-metabolic growth-energy consumption is always in line with the entropy principle.

To evaluate the regenerative part of the solid volume production, it must be taken into account that more growth energy is consumed if the regenerative mass production increases. Therefore, both processes must be evaluated together. Inserting the additional growth-energy consumption and the regenerative volume production into the entropy inequality, the dissipation equation of the regenerative process reads

$$\begin{aligned} \mathcal{D}_n + \mathcal{D}_{\mathcal{C}} &= \rho^{SR}\, \hat{n}^S_{\mathrm{reg}} \Big[\xi^L - \xi^S \Big] - \frac{\hat{C}^F_{\mathrm{grow}}}{\mathcal{C}^F} \rho^{\mathcal{C}}_F \mu^{\mathcal{C}} \\ &= \rho^{SR}\, \hat{n}^S_{\mathrm{reg}} \Big[\xi^L - \xi^S + \frac{k_{\mathrm{grow}}}{f^{\mathcal{C}} \rho^{SR}}\, \mu^{\mathcal{C}} \Big] \geq 0 \,. \end{aligned} \tag{5.64}$$

Since the volume production $\hat{n}^S_{\mathrm{reg}}$ is defined positive (cf. (7.14)), a regenerative process is only possible if the term in brackets is positive or equal to zero:

$$\xi^L - \xi^S + \frac{k_{\mathrm{grow}}}{f^{\mathcal{C}} \rho^{SR}} \mu^{\mathcal{C}} \geq 0 \,. \tag{5.65}$$

To receive a restriction in terms of growth energy, this inequality is reformulated using the definition of $\mu^{\mathcal{C}}$ given in (5.22), which leads to

$$\mathcal{C}^F \geq \mathcal{C}^F_0 = f^{\mathcal{C}} \left(\exp\Big(f^{\mathcal{C}} \rho^{SR} \frac{\xi^L - \xi^S}{k_{\mathrm{grow}}} - \mu^{\mathcal{C}}_0 \Big) \right)^{1/(R^{\mathcal{C}}\theta)} = \text{const.} \tag{5.66}$$

Briefly speaking, regenerative processes are only possible, if the growth energy exceeds a specific threshold. Otherwise only degenerative processes occur. Note that the threshold $\mathcal{C}^F_0$ marks an idealised, theoretic value, below which no regenerative processes occur, i. e., $\hat{n}^S_{\mathrm{reg}} = 0$. The real threshold of a biochemical reaction might be higher than this value.

To give a biochemical explanation of these results, the continuum-mechanical evaluation of the entropy principle restricts the direction of these processes towards the lower overall *Gibbs* free enthalpy. This is in accordance with explanations found in textbooks on physics and chemistry (cf. Atkins & de Paula, 2006). Following this, the basal growth-energy consumption $\hat{\mathcal{C}}^F_{\mathrm{basal}}$ as well as the tissue matrix degeneration $\hat{n}^S_{\mathrm{deg}}$ summarise exergonic processes, i. e., they proceed without the need of an external source of energy and can be used as energy sources for other processes. As a logical consequence, the reverse processes are endergonic and need a driving external source of energy. In this context,

the regenerative process $\hat{n}^S_{\mathrm{reg}}$ is driven by the additional growth-energy consumption $\hat{\mathcal{C}}^F_{\mathrm{grow}}$. Thus, both processes must be evaluated together leading to restrictions for the combined process. As a result, the endergonic regenerative solid volume production is possible, as long as the combined process remains exergonic. This is the case as long as the growth energy exceeds the threshold value $\mathcal{C}^F_0$, which marks the equilibrium of the combined process.

5.4. Discussion

In this chapter, two different approaches for the definition of a non-mechanical quantity summarising the contribution of the fluid constituents to the cellular energy metabolism are introduced. First, following a bottom-up strategy, a temperature-equivalent growth energy was introduced. There, it became clear that a straight-forward definition of the growth energy using the partial densities is impossible due to the different dependencies of mass and temperature. However, choosing an appropriate definition for the temperature-equivalent growth energy, it remained unclear how to interpret the production of the concentration-equivalent "configurational growth entropy" ($\hat{\eta}^\alpha_{\mathcal{C}} \geq 0$), cf. Section 5.2.

To avoid a discussion on the basic thermodynamic principles, an alternative top-down approach is introduced. Starting from the definition of the growth energy, the relevant governing equations are determined. This results in a concentration-equivalent growth energy. Evaluation of the equivalent entropy inequality leads to restrictions for the growth-energy production, which are fulfilled by a negative growth-energy production. Ex post, this result postulates equivalent requirements as the production of the "configurational growth entropy" following the temperature-equivalent approach. However, in the temperature-equivalent approach, it is required as a presupposition for the entropy evaluation, whereas in the concentration-equivalent approach it results from the entropy evaluation following the standard arguments of rational thermodynamics. Giving a practical explanation, the negative growth-energy production is achieved by the oxidation of nutrients to water and carbon dioxide, following the metabolic pathways of the cellular energy-metabolism described in Section 2.3.

In summary, both approaches lead to the same requirements and restrictions. However, the concentration-equivalent growth energy provides the clearer representation, and is therefore used throughout this monograph. Recalling the discussion on the cellular energy metabolism in Section 2.3, the growth energy must not be interpreted as a holistic quantity, which includes all aspects of the cellular energy metabolism. Instead, the included nutrients and the used energy values require a tissue-specific consideration.

Chapter 6: Numerical treatment

For the numerical treatment of initial-boundary-value problems, the weak variational formulation of the governing partial differential equations is implemented and numerically discretised in space and time by employing a standard *Galerkin*[1] method (*Bubnov*[2]-*Galerkin*). The presented continuum-mechanical growth model is governed by five independent field variables: the solid displacement vector $\mathbf{u}_S$, the fluid seepage velocity $\mathbf{w}_F$, the effective fluid pressure p^{FR}, the growth-energy diffusion velocity $\mathbf{d}_{\mathcal{C}F}$ and the growth energy $\mathcal{C}^F$. However, by use of (5.54), the filter velocity $n^F\mathbf{w}_F$ is obtained as a function of the pressure gradient, and the growth-energy gradient governs $\mathbf{d}_{\mathcal{C}F}$ via (5.57). Hence, the fluid seepage velocity and the growth-energy diffusion velocity can be substituted by the respective gradient terms. Accordingly, the number of independent field variables reduces to three, and $\mathbf{w}_F$ and $\mathbf{d}_{\mathcal{C}F}$ can be computed in a post-processing step. In summary, the governing equations are the overall momentum balance (5.46),

$$\mathbf{0} = \operatorname{div}(\mathbf{T}^S_{E/\mathrm{mech}} + \mathbf{T}^S_{E/\mathrm{grow}} - p^{FR}\mathbf{I}) + \hat{n}^S\rho^{SR}\mathbf{w}_F\,, \tag{6.1}$$

the overall volume balance (4.9),

$$0 = \operatorname{div}[(\mathbf{v}_S + n^F\mathbf{w}_F] - \hat{n}^S\Big(1 - \frac{\rho^{SR}}{\rho^{FR}}\Big)\,, \tag{6.2}$$

and the growth-energy balance (5.14), where, following Lanir (1987), the growth energy is assumed to be instantaneously at its equilibrium ($(\mathcal{C}^F)'_S = 0$),

$$0 = \mathcal{C}^F \operatorname{div}\mathbf{v}_S + \operatorname{div}[n^F\mathcal{C}^F(\mathbf{w}_F + \mathbf{d}_{\mathcal{C}F})] - \hat{\mathcal{C}}^F - \mathcal{C}^F\hat{n}^S\,. \tag{6.3}$$

Therein, $\mathbf{T}^S_{E/\mathrm{mech}}(\mathbf{u}_S, n^S)$, $\mathbf{T}^S_{E/\mathrm{grow}}(\mathbf{u}_S, n^S)$ and $\hat{n}^S$ have to be chosen problem-dependent (cf. chapter 7), $\mathbf{v}_S = \overset{\prime}{\mathbf{u}}_S$ (3.7), and $\hat{\mathcal{C}}^F$ according to (5.59). Furthermore, $\mathbf{w}_F = \mathbf{w}_F(p^{FR})$ and $\mathbf{d}_{\mathcal{C}F} = \mathbf{d}_{\mathcal{C}F}(\mathcal{C}^F)$ are functions of the pore pressure p^{FR} and the growth energy $\mathcal{C}^F$, see (5.54) and (5.57).

The growth and remodelling processes within biological tissues are here modelled by changes of the volume fraction of the accompanying reference configuration n^S_{tS}. It is possible to calculate the growth process globally by introducing an additional field variable or locally at every integration point (cf. Zienkiewicz & Taylor, 1989b).

For a global calculation, the solid volume fraction n^S must be used as an additional degree of freedom of the finite element system with the solid volume balance $(4.3)_{\alpha=S}$ as governing equation readily blowing up the system size. Here, the solid volume fraction is

[1] *Boris Grigoryevich Galyorkin* (1871–1945): Soviet engineer and mathematician, who became famous for the variational principle named after him.

[2] *Ivan Grigoryevich Bubnov* (1872–1919): Russian marine engineer and designer of submarines. His work "Structural mechanics of ships" published in 1906 contained the first description of the *Bubnov-Galerkin* method

calculated locally in the sense of a collocation method by introducing n^S_{tS} as an internal history variable. The additional information for the calculation of n^S_{tS} is provided by additional, problem-specific biological submodels. In particular, see Section 7.1 for the description of tumour growth, Section 7.2 for a phenomenological bone remodelling model and Section 7.3 for a biologically motivated cell-population model of bone remodelling.

For the numerical solution, monolithic solution strategies and decoupled solution strategies are applicable. Following the traditional, monolithic solution strategy, the local equation system is solved by the finite-element application, which solves the global equation system. In contrast, in a decoupled solution strategy, the problem is separated into several submodels, which are solved by individual tailored programs, which are integrated to an overall solution using web-service technology.

6.1. Monolithic solution strategy

Following the standard *Galerkin* procedure, the weak formulations of the governing field equations are obtained by multiplying each equation with a test function and integrating over the domain Ω occupied by the body. After applying the product rule and the *Gauss*ian integral theorem, the weak formulation of the overall momentum balance reads

$$\mathcal{G}_t = \int_\Omega (\mathbf{T}^S_{E/\mathrm{mech}} + \mathbf{T}^S_{E/\mathrm{grow}} + p^{FR}\,\mathbf{I}) \cdot \operatorname{grad} \delta\mathbf{u}_S \,\mathrm{d}v - \int_{\Gamma_t} \bar{\mathbf{t}} \cdot \delta\mathbf{u}_S \,\mathrm{d}a = 0\,, \tag{6.4}$$

the weak formulation of the overall volume balance becomes

$$\begin{aligned}\mathcal{G}_v = \int_\Omega \Big[\operatorname{div} \mathbf{v}_S\, \delta p^{FR} - \hat{n}^S \Big(1 - \frac{\rho^{SR}}{\rho^{FR}}\Big)\, \delta p^{FR} - n^F \mathbf{w}_F \cdot \operatorname{grad} \delta p^{FR}\Big] \mathrm{d}v + \\ + \int_{\Gamma_v} \bar{v}^F\, \delta p^{FR}\, \mathrm{d}a = 0\,,\end{aligned} \tag{6.5}$$

and the weak formulation of the growth-energy balance reads

$$\begin{aligned}\mathcal{G}_d = \int_\Omega \Big[\mathcal{C}^F \operatorname{div}(\mathbf{u}_S)'_S - \hat{\mathcal{C}}^F\Big] \delta\mathcal{C}^F \mathrm{d}v - \int_\Omega n^F \mathcal{C}^F (\mathbf{w}_F + \mathbf{d}_{\mathcal{C}F}) \cdot \operatorname{grad} \delta\mathcal{C}^F \mathrm{d}v + \\ + \int_{\Gamma_d} \bar{d}^{\mathcal{C}}_F\, \delta\mathcal{C}^F \mathrm{d}v = 0\,.\end{aligned} \tag{6.6}$$

In these equations, $\delta\mathbf{u}_S$, δp^{FR} and $\delta\mathcal{C}^F$ are the test functions, which correspond to the solid displacement $\mathbf{u}_S$, the pore pressure p^{FR} and the growth energy $\mathcal{C}^F$. Furthermore, $\bar{\mathbf{t}} = (\mathbf{T}^S_{E/\mathrm{mech}} + \mathbf{T}^S_{E/\mathrm{grow}} + p^{FR}\,\mathbf{I})\mathbf{n}$ denotes the outward-oriented total external load vector, which acts on the *Neumann*[3] boundary Γ_t of the overall medium, where $\mathbf{n}$ is the outward-oriented unit surface normal vector. Analogously, $\bar{v}^F = n^F \mathbf{w}_F \cdot \mathbf{n}$ denotes the fluid volume efflux through the *Neumann* boundary Γ_v. As well, $\bar{d}^{\mathcal{C}}_F = n^F \mathcal{C}^F (\mathbf{w}_F + \mathbf{d}_{\mathcal{C}F}) \cdot \mathbf{n}$ denotes the

[3] *Carl Gottfried Neumann* (1832–1925): German mathematician, who can be considered as one of the initiator of the theory of integral equations.

growth energy efflux through the *Neumann* boundary Γ_d. On the *Dirichlet*[4] boundaries, boundary conditions $\bar{\mathbf{u}}_S$ on $\Gamma_{\mathbf{u}_S}$, $\bar{p}^{FR}$ on Γ_p and $\bar{\mathcal{C}}^F$ on $\Gamma_{\mathcal{C}^F}$ are exactly fulfilled by the respective field variables, and the corresponding test functions $\delta\mathbf{u}_S$, δp^{FR} and $\delta\mathcal{C}^F$ vanish.

For a clearer representation, the variational problem is summarised in a compact vector notation using the functional vector $\boldsymbol{\mathcal{G}}_{\boldsymbol{u}}$, which collects the weak formulations (6.4)–(6.6), the vector of internal variables $\boldsymbol{q}$, which contains the variables of the biological submodel, i. e., at least the solid volume fraction n_{tS}^S, and the vector of unknowns $\boldsymbol{u}$, which contains the unknown field variables:

$$\begin{aligned} \boldsymbol{\mathcal{G}}_{\boldsymbol{u}} &= \begin{bmatrix} \mathcal{G}_t \\ \mathcal{G}_v \\ \mathcal{G}_d \end{bmatrix}, \quad \boldsymbol{q} = \begin{bmatrix} n_{tS}^S \\ \cdots \end{bmatrix}, \quad \boldsymbol{u} = \begin{bmatrix} \mathbf{u}_S \\ p \\ \mathcal{C}^F \end{bmatrix}, \\ \delta\boldsymbol{u} &= \begin{bmatrix} \delta\mathbf{u}_S \\ \delta p \\ \delta\mathcal{C}^F \end{bmatrix}, \quad \boldsymbol{u}'_S = \begin{bmatrix} (\mathbf{u}_S)'_S \\ (p)'_S \\ (\mathcal{C}^F)'_S \end{bmatrix}, \quad \boldsymbol{u}_0 = \begin{bmatrix} \mathbf{u}_{S0} \\ p_0 \\ \mathcal{C}_0^F \end{bmatrix}. \end{aligned} \tag{6.7}$$

Herein, the vector $\delta\boldsymbol{u}$ of the test functions, the solid time derivative of the vector of unknowns $\boldsymbol{u}'_S$ and its initial value $\boldsymbol{u}_0 = \boldsymbol{u}(\mathbf{x}, t_0)$ are defined corresponding to the vector of unknowns. With these abbreviations, the variational problem (6.4)–(6.6) is rewritten in abstract form as:

$$\text{Find} \quad \boldsymbol{u} \in \mathcal{S}_{\boldsymbol{u}}(t) \quad \text{such that} \quad \boldsymbol{\mathcal{G}}_{\boldsymbol{u}}(\boldsymbol{u}, \delta\boldsymbol{u}, \boldsymbol{q}) = \mathbf{0} \quad \forall\, \delta\boldsymbol{u} \in \mathcal{T}_{\boldsymbol{u}}\,,\ t \in [t_0, T]\,. \tag{6.8}$$

Herein, $\mathcal{S}_{\boldsymbol{u}}(t)$ is the trial space of $\boldsymbol{u}$, $\mathcal{T}_{\boldsymbol{u}}$ is the test space of $\delta\boldsymbol{u}$, and $[t_0, T]$ is the considered time interval. Next, the function spaces $\mathcal{S}_{\boldsymbol{u}}$ and $\mathcal{T}_{\boldsymbol{u}}$ are defined, such that they provide useful approximations of the integrals in the definition of $\boldsymbol{\mathcal{G}}_{\boldsymbol{u}}$.

6.1.1. Finite-Element Method

For the spatial discretisation of equations (6.4)–(6.6), the spatial domain Ω is partitioned into N_e non-overlapping subdomains Ω_e, which yield an approximated domain Ω^h,

$$\Omega \approx \Omega^h = \bigcup_{e=1}^{N_e} \Omega_e\,. \tag{6.9}$$

The subdomains Ω_e are represented by Finite Elements (FE). The FE mesh contains N_n nodes, where each element is defined by a fixed number of nodes. Proceeding from here, the infinite trial and test spaces $\mathcal{S}_{\boldsymbol{u}}(t)$ and $\mathcal{T}_{\boldsymbol{u}}(t)$ are replaced by discrete trial and test

[4] *Johann Peter Gustav Lejeune Dirichlet* (1805–1859): German mathematician, who worked in the fields of analysis and number theory, where he introduced many fundamental tools that were later named after him.

spaces $\mathcal{S}_{\boldsymbol{u}}^h(t)$ and $\mathcal{T}_{\boldsymbol{u}}^h(t)$, viz:

$$\begin{aligned} \boldsymbol{u}^h(\mathbf{x},t) &= \bar{\boldsymbol{u}}^h(\mathbf{x},t) + \sum_{i=1}^{N_{\boldsymbol{u}}} \boldsymbol{N}_{\boldsymbol{u}(i)}(\mathbf{x})\boldsymbol{u}_{(i)}(t) \in \mathcal{S}_{\boldsymbol{u}}^h(t)\,, \\ \delta\boldsymbol{u}^h(\mathbf{x}) &= \sum_{i=1}^{M_{\boldsymbol{u}}} \boldsymbol{M}_{\boldsymbol{u}(i)}(\mathbf{x})\delta\boldsymbol{u}_{(i)} \in \mathcal{T}_{\boldsymbol{u}}^h\,. \end{aligned} \tag{6.10}$$

Herein, $\bar{\boldsymbol{u}}^h(\mathbf{x},t)$ is defined by the *Dirichlet* boundary conditions, $N_{\boldsymbol{u}}$ is the number of nodes used for the approximation of the fields in $\boldsymbol{u}$, $\boldsymbol{N}_{\boldsymbol{u}(i)}(\mathbf{x})$ denotes the global basis function that corresponds to the node i, i. e., it is equal to one at the node i and equal to zero at all other nodes, $\boldsymbol{u}_{(i)}(t)$ is the time-dependent nodal value. Concerning the test functions $\delta\boldsymbol{u}^h$, $M_{\boldsymbol{u}}$ is the number of nodes used for the approximation of the test functions $\delta\boldsymbol{u}$, $\boldsymbol{M}_{\boldsymbol{u}(i)}(\mathbf{x})$ denotes the global basis functions, and $\delta\boldsymbol{u}_{(i)}$ corresponds to the nodal values of the test functions. Here, following a standard Bubnov-Galerkin procedure, the same set of basis functions is chosen for the test and trial functions $\boldsymbol{N}_{\boldsymbol{u}(i)} \equiv \boldsymbol{M}_{\boldsymbol{u}(i)}$. However, note that the basis functions of different field variables do not necessarily coincide.

The internal variables are collected in a finite vector $\boldsymbol{q}^h = \boldsymbol{q}^h(\mathbf{x}_j,t) = \boldsymbol{q}_j^h(t)$, which contains the values at discrete spacial points $\mathbf{x}_j$, $(j \in \{1,2,\dots N_q\})$, more precisely, at the integration points of the FE mesh, where N_q is the number of integration points. Following this, the variational problem (6.8) in a semi-discrete formulation reads:

$$\text{Find} \quad \boldsymbol{u}^h \in \mathcal{S}_{\boldsymbol{u}}^h(t) \quad \text{such that} \quad \boldsymbol{\mathcal{G}}_{\boldsymbol{u}}^h(\boldsymbol{u}^h, \delta\boldsymbol{u}^h, \boldsymbol{q}^h) = \mathbf{0} \quad \forall\, \delta\boldsymbol{u}^h \in \mathcal{T}_{\boldsymbol{u}}^h\,,\ t \in [t_0,T]\,. \tag{6.11}$$

To complete the spatial discretisation, an adequate set of trial and test functions must be specified. Thereby, it must be taken into account that the governing equations represent a strongly coupled system of equations, where the unknowns are either determined simultaneously requiring a mixed finite element formulation, or successively by employing a decoupled solution strategy. In both cases, the set of useful test and trial functions depends on the applied splitting and time-stepping algorithms, and will be revised later.

6.1.2. Spatial discretisation

To provide a clear and compact representation of the considered global differential algebraic equation (DAE), the primary variables and the corresponding trial functions, as well as the related derivatives are represented by numerical vectors and matrices that contain the nodal values $\mathbf{u}_S$, $\mathbf{p}$, $\mathbf{c}$ and the associated test functions $\delta\mathbf{u}_S$, $\delta\mathbf{p}$ and $\delta\mathbf{c}$:

$$\begin{aligned} \boldsymbol{u}^h &= \begin{bmatrix} \boldsymbol{U}\mathbf{u}_S \\ \boldsymbol{P}\mathbf{p} \\ \boldsymbol{C}\mathbf{c} \end{bmatrix}, \quad (\boldsymbol{u}^h)'_S = \begin{bmatrix} \boldsymbol{U}\dot{\mathbf{u}}_S \\ \boldsymbol{P}\dot{\mathbf{p}} \\ \boldsymbol{C}\dot{\mathbf{c}} \end{bmatrix}, \quad \operatorname{grad}\boldsymbol{u}^h = \begin{bmatrix} \nabla\boldsymbol{U}\mathbf{u}_S \\ \nabla\boldsymbol{P}\mathbf{p} \\ \nabla\boldsymbol{C}\mathbf{c} \end{bmatrix}, \\ \delta\boldsymbol{u}^h &= \begin{bmatrix} \boldsymbol{U}\delta\mathbf{u}_S \\ \boldsymbol{P}\delta\mathbf{p} \\ \boldsymbol{C}\delta\mathbf{c} \end{bmatrix}, \quad \operatorname{grad}\delta\boldsymbol{u}^h = \begin{bmatrix} \nabla\boldsymbol{U}\delta\mathbf{u}_S \\ \nabla\boldsymbol{P}\delta\mathbf{p} \\ \nabla\boldsymbol{C}\delta\mathbf{c} \end{bmatrix}. \end{aligned} \tag{6.12}$$

Herein, $\boldsymbol{U}$, $\boldsymbol{P}$ and $\boldsymbol{C}$ represent the interpolation functions that correspond to the nodal unknowns $\mathbf{u}_S$, $\mathbf{p}$ and $\mathbf{c}$ of the FE mesh. Furthermore, for the temporal and spatial derivatives, the abbreviations $(\cdot)^{\bullet} := (\cdot)'_S$ and $\nabla(\cdot) := \operatorname{grad}(\cdot)$ are used. Thus, the semi-discrete formulation of the variational problem in matrix form reads

$$\boldsymbol{\mathcal{G}}_{\boldsymbol{u}}^h = \underbrace{\begin{bmatrix} \mathbf{0} & \mathbf{0} & \mathbf{0} \\ \boldsymbol{M}_{21} & \mathbf{0} & \mathbf{0} \\ \boldsymbol{M}_{31} & \mathbf{0} & \mathbf{0} \end{bmatrix}}_{\boldsymbol{M}} \underbrace{\begin{bmatrix} \dot{\mathbf{u}}_S \\ \dot{\mathbf{p}} \\ \dot{\mathbf{c}} \end{bmatrix}}_{\dot{\mathbf{u}}} + \underbrace{\begin{bmatrix} \boldsymbol{K}_{11} & \boldsymbol{K}_{12} & \mathbf{0} \\ \mathbf{0} & \boldsymbol{K}_{22} & \mathbf{0} \\ \mathbf{0} & \boldsymbol{K}_{32} & \boldsymbol{K}_{33} \end{bmatrix}}_{\boldsymbol{K}} \underbrace{\begin{bmatrix} \mathbf{u}_S \\ \mathbf{p} \\ \mathbf{c} \end{bmatrix}}_{\mathbf{u}} - \underbrace{\begin{bmatrix} \mathbf{f}_u \\ \mathbf{f}_p \\ \mathbf{b}_c + \mathbf{f}_c \end{bmatrix}}_{\mathbf{f}} = \mathbf{0} \,. \tag{6.13}$$

Herein, the overall momentum balance is given by the first row; the second and third rows specify the overall volume and the growth-energy balances. In the context of linear elasticity, the submatrix $\boldsymbol{K}_{11}$ contains the elastic solid tangent. The remaining submatrices $\boldsymbol{M}_{ij}$ and $\boldsymbol{K}_{ij}$ of the mass and stiffness matrices of (6.13) are given by

$$\begin{aligned}
\boldsymbol{M}_{21} &= -\int_{\Omega^h} \boldsymbol{P}^T \nabla \boldsymbol{U} \, \mathrm{d}v \,, \\
\boldsymbol{M}_{31} &= \int_{\Omega^h} \boldsymbol{C}^T (\boldsymbol{C}\mathbf{c}) \nabla \boldsymbol{U} \, \mathrm{d}v \,, \\
\boldsymbol{K}_{12} &= -\int_{\Omega^h} \nabla \boldsymbol{U}^T \boldsymbol{P} \, \mathrm{d}v \,, \\
\boldsymbol{K}_{22} &= \int_{\Omega^h} \nabla \boldsymbol{P}^T \frac{k^F}{\gamma^{FR}} \nabla \boldsymbol{P} \, \mathrm{d}v \,, \\
\boldsymbol{K}_{32} &= \int_{\Omega^h} \nabla \boldsymbol{C}^T (\boldsymbol{C}\mathbf{c}) \frac{k^F}{\gamma^{FR}} \nabla \boldsymbol{P} \, \mathrm{d}v \,, \\
\boldsymbol{K}_{33} &= \int_{\Omega^h} \nabla \boldsymbol{C}^T D^{\mathcal{C}} \nabla \boldsymbol{C} \, \mathrm{d}v + \int_{\Omega^h} \nabla \boldsymbol{C}^T \frac{k^F}{\gamma^{FR}} (\nabla \boldsymbol{P}\mathbf{p}) \boldsymbol{C} \, \mathrm{d}v + \int_{\Omega^h} \boldsymbol{C}^T (\nabla \boldsymbol{U}\dot{\mathbf{u}}) \boldsymbol{C} \, \mathrm{d}v \,.
\end{aligned} \tag{6.14}$$

Furthermore, $\mathbf{f}_u$, $\mathbf{f}_p$ and $\mathbf{f}_c$ are the space-discrete *Neumann* boundary conditions, and $\mathbf{b}_c$ represents the growth-energy production:

$$\begin{aligned}
\mathbf{f}_u &= \int_{\Gamma_t^h} \boldsymbol{U}^T \bar{\mathbf{t}} \, \mathrm{d}a \,, & \mathbf{f}_p &= -\int_{\Gamma_v^h} \boldsymbol{P}^T \bar{v}^F \, \mathrm{d}a \,, \\
\mathbf{f}_c &= -\int_{\Gamma_d^h} \boldsymbol{C}^T \bar{d}^{\mathcal{C}} \, \mathrm{d}a \,, & \mathbf{b}_c &= \int_{\Omega^h} \boldsymbol{C}^T \hat{\mathcal{C}}^F \mathrm{d}v \,.
\end{aligned} \tag{6.15}$$

For a compact representation of (6.13), the nodal degrees of freedom are collected in a global vector $\mathbf{u} = [\mathbf{u}_S, \mathbf{p}, \mathbf{c}]^T$. This, in combination with the global vector of internal variables $\mathbf{q} = \boldsymbol{q}^h$, which summarises the values of the internal variables at the integration points, yields an abstract representation of (6.13) using matrix notation

$$\boldsymbol{\mathcal{G}}_{\boldsymbol{u}}^h(t, \mathbf{u}, \dot{\mathbf{u}}, \mathbf{q}) \equiv \boldsymbol{M}\dot{\mathbf{u}} + \boldsymbol{K}\mathbf{u} - \mathbf{f} \stackrel{!}{=} \mathbf{0} \tag{6.16}$$

with the generalised mass and stiffness matrices $\boldsymbol{M}$ and $\boldsymbol{K}$, and the generalised external force vector $\mathbf{f}$. Within this equation, the mass matrix $\boldsymbol{M}$ is rank deficient. Hence,

in a monolithic solution, no explicit time integration is possible, and an implicit time integration scheme must be applied.

The simultaneous solution of the strongly coupled system of equations (6.13) (coupling terms marked grey) requires the use of mixed finite elements. The considered solid-fluid problem yields a saddle-point problem (Markert, 2008, pp. 418 f.) where the solution is a minimum with respect to the displacement $\mathbf{u}_S$ and a maximum with respect to the fluid pressure p^{FR}. As a consequence, the equation system is indefinite. This, in combination with a low permeability ($k^F \ll 1$), leads to strongly mesh-dependent results with strange instabilities that arise from spurious pressure modes if equal approximation orders are used (cf. Brezzi & Fortin, 1991, p. 210). More precisely, the patch test or the inf-sub condition (also known as *Ladyzhenskaya*[5]*-Babuška-Brezzi* (LBB) condition) must be fulfilled. These conditions are satisfied if the approximations for shape and test functions of the solid displacement are chosen one order higher than the approximations used for shape and test functions of the fluid pressure and the growth energy (Acartürk, 2009, p. 86). Here, *Taylor-Hood* elements with quadratic approximations for the solid displacement and linear approximations for the remaining primary variables are used. They are the simplest combination that yields stable results (Braess, 1997, p. 148).

Internal variables

The biological variables are only needed to evaluate the integrals within the stiffness matrix $\boldsymbol{K}$. Hence, it is sufficient to calculate them only at the integration points of the FE mesh (collocation). Thus, a set of local differential equations $\boldsymbol{\mathcal{L}}^h$ must be solved:

$$\boldsymbol{\mathcal{L}}^h = \boldsymbol{A}\dot{\mathbf{q}} - \mathbf{r}(\mathbf{q}, \mathbf{u}) = \mathbf{0}\,. \tag{6.17}$$

Therein, $\boldsymbol{A}$ represents the local mass matrix, and $\mathbf{r}$ is the local stiffness vector. Here, the internal variables $\mathbf{q}$ represent the state of the biological submodel, which is calculated employing (7.8) and (7.14). A closer look at these equations reveals that $\boldsymbol{A}$ is a regular identity matrix, and the local system $\boldsymbol{\mathcal{L}}^h$ represents a system of ordinary differential equations (ODE) of first order in time.

6.1.3. Time discretisation

For the time discretisation, the nodal degrees of freedom $\mathbf{u}$ and the internal variables $\mathbf{q}$ are summarised in a global vector of unknowns $\mathbf{y} = [\mathbf{u}, \mathbf{q}]^T \in \mathbb{R}^m$ with $m = \dim(\mathbf{u}) + \dim(\mathbf{q})$. Thus, the initial-boundary-value problem given by differential algebraic equations (DAE) with initial values $\mathbf{y}(t_0) = \mathbf{y}_0$ and $t \in [t_0, T]$ can be written in a general implicit form as

$$\boldsymbol{F}(t, \mathbf{y}, \dot{\mathbf{y}}) \equiv \begin{bmatrix} \boldsymbol{\mathcal{G}}^h(t, \mathbf{u}, \dot{\mathbf{u}}, \mathbf{q}) \\ \boldsymbol{\mathcal{L}}^h(t, \mathbf{q}, \dot{\mathbf{q}}, \mathbf{u}) \end{bmatrix} \equiv \begin{bmatrix} \boldsymbol{M}\dot{\mathbf{u}} + \boldsymbol{K}\mathbf{u} - \mathbf{f} \\ \boldsymbol{A}\dot{\mathbf{q}} - \mathbf{r} \end{bmatrix} \stackrel{!}{=} \mathbf{0}\,. \tag{6.18}$$

[5] *Olga Aleksandrovna Ladyzhenskaya* (1922–2004): Soviet and Russian mathematician known for her works on partial differential equations and fluid dynamics.

For the time integration of (6.18), diagonal implicit *Runge-Kutta*[6] (DIRK) methods are suitable single step methods for the solution of large systems of DAE of first order at moderate storage and computational costs by successively calculating the stage solutions in a decoupled fashion (Diebels *et al.*, 1999; Ellsiepen, 1999). Thereby, the time interval $[t_0, T]$ is split into subintervals $[t_n, t_{n+1}]$ with step size $\Delta t_n = t_{n+1} - t_n$. To guarantee that the algebraic constraints are fulfilled at the beginning of each subinterval, stiffly accurate methods are preferred, where the time point of the last *Runge-Kutta* stage coincides with the end of the approximated time interval t_{n+1}. Hence, the approximated solution $\mathbf{y}_{n+1} \approx \mathbf{y}(t_{n+1})$ at time t_{n+1} is equivalent to the solution of the last *Runge-Kutta* stage $\mathbf{Y}_{ns}$, which fulfils the algebraic constraints. The approximated solution $\mathbf{y}_{n+1}$ is determined by applying an s-stage *Runge-Kutta* algorithm (Algorithm 1) on the approximated solution $\mathbf{y}_n \approx \mathbf{y}(t_n)$ at time t_n, which successively leads to an approximated solution for the whole temporal domain. In this algorithm, n is the current time step, $\mathbf{Y}_{ni}$ is the approximated

Algorithm 1: Time-step algorithm of a stiffly accurate s-stage DIRK method

Given: Coefficients c_i, a_{ij} of a stiffly accurate s-stage DIRK method, approximate solution $\mathbf{y}_n \approx \mathbf{y}(t_n)$ at time t_n, and time step size Δt_n

Find: Approximate solution $\mathbf{y}_{n+1} \approx \mathbf{y}(t_{n+1})$ at time t_{n+1}

1 **for each** *Runge-Kutta stage* $i = 1, \ldots, s$ **do**

2 set stage time $T_{ni} \leftarrow t_n + c_i \Delta t_n$ and
accumulated stage derivative $\overline{\mathbf{Y}}_{ni} \leftarrow \Delta t_n \sum_{j=1}^{i-1} a_{ij} \dot{\mathbf{Y}}_{nj}$

3 solve nonlinear system for stage increments $\Delta \boldsymbol{Y}_{ni}$
$\boldsymbol{R}_{ni}(\Delta \mathbf{Y}_{ni}) \equiv \boldsymbol{F}(T_{ni}, \mathbf{y}_n + \Delta \mathbf{Y}_{ni}, \frac{1}{\Delta t_n a_{ii}}[\Delta \mathbf{Y}_{ni} - \overline{\mathbf{Y}}_{ni}]) \stackrel{!}{=} \mathbf{0}$

4 set stage derivative $\dot{\mathbf{Y}}_{ni} \leftarrow \frac{1}{\Delta t_n a_{ii}}[\Delta \mathbf{Y}_{ni} - \overline{\mathbf{Y}}_{ni}]$

end

5 $\mathbf{y}_{n+1} \leftarrow \mathbf{Y}_{ns} = \mathbf{y}_n + \Delta \mathbf{Y}_{ns}$ and $t_{n+1} \leftarrow T_{ns}$

solution at stage i, and $\dot{\mathbf{Y}}_{ni}$ is the stage derivative with the accumulated stage derivative $\overline{\mathbf{Y}}_{ni}$, which is a constant that depends only on the results of the previous stages. To reduce round off errors, the stage increments $\Delta \mathbf{Y}_{ni} = \mathbf{Y}_{ni} - \mathbf{y}_n$ are used as unknowns instead of $\mathbf{Y}_{ni}$. By choosing the coefficients $s = 1$ and $c_1 = a_{11} = 1$, one obtains the implicit or backward Euler method.

In Algorithm 1, the solution of the non-linear system in line 3 requires the most computational effort. For its computation using the *Newton*[7]*-Raphson*[8] method, the *Jacobi*[9]-

[6] *Carl David Tolmé Runge* (1856–1927) and *Martin Wilhelm Kutta* (1867–1944): both German mathematician, who developed the *Runge-Kutta* method in 1901.

[7] *Sir Isaac Newton* (1643–1727): English physicist and mathematician, who is regarded as one of the most influential scientists of all time.

[8] *Joseph Raphson* (1648–1715): English mathematician best know for the *Newton-Raphson* method for the numerical approximating the solution of non-linear equations and the root's of an equations.

[9] *Carl Gustav Jacob Jacobi* (1804–1851): German mathematician, who contributed to elliptic functions, dynamics, differential equations and number theory.

matrix $\boldsymbol{J}_{ni}$, i. e., the derivative of the nonlinear vector function $\boldsymbol{R}_{ni}$ with respect to the stage increments $\Delta\boldsymbol{Y}_{ni}$, is needed. It has the form

$$\boldsymbol{J}_{ni} = \frac{\mathrm{d}\boldsymbol{R}_{ni}}{\mathrm{d}\Delta\mathbf{Y}_{ni}} = \left.\frac{\partial \boldsymbol{F}}{\partial \mathbf{y}}\right|_{\boldsymbol{z}} + \frac{1}{\Delta t_n a_{ii}} \left.\frac{\partial \boldsymbol{F}}{\partial \dot{\mathbf{y}}}\right|_{\boldsymbol{z}} , \tag{6.19}$$

where $\boldsymbol{z} = \{T_{ni}, \mathbf{Y}_{ni}, \dot{\mathbf{Y}}_{ni}\}$ denotes the current set of arguments of $\boldsymbol{F}$. However, if $\boldsymbol{J}_{ni}$ is used to solve the linear system of equations, the included linearisations of the time-discrete system of local evolution equations would completely destroy the sparse structure of the linearised global FEM equations (Ehlers & Ellsiepen, 2001). This can be avoided by using a generalisation of the block *Gauss-Seidel*[10] method, known as multilevel or two-stage *Newton* method (Algorithm 2), where, taking advantage of the structure of the DAE system (6.18), the sparse structure of the global system is retrained and the local integration point systems are solved in a decoupled fashion. For every *Newton* iteration

Algorithm 2: 2-stage solution algorithm for the nonlinear global-local system

Given: Coefficients c_i, a_{ij} of a stiffly accurate s-stage DIRK method, approximate solution $\mathbf{y}_n \approx \mathbf{y}(t_n)$ at time t_n, and time step size Δt_n

Find: Approximate solution $\mathbf{y}_{n+1} \approx \mathbf{y}(t_{n+1})$ at time t_{n+1}

1 **solve local integration point system** with fixed $\Delta\boldsymbol{U}_{ni}^k$

$\boldsymbol{L}_{ni}^k(\Delta\mathbf{Q}_{ni}^k; \Delta\mathbf{U}_{ni}^k) = \mathbf{0} \longrightarrow \Delta\mathbf{Q}_{ni}^k = \Delta\mathbf{Q}_{ni}^k(\Delta\mathbf{U}_{ni}^k)$

2 **solve nonlinear global FEM system**

compute consistent global Jacobian matrix $(\boldsymbol{J}_{\boldsymbol{u}})_{ni}^k$

solve global sparse linear FEM system

update vector of global variables (nodal DOFs)

$\mathbf{u}_{ni}^{k+1} \leftarrow \mathbf{u}_{ni}^k + \Delta\mathbf{u}_{ni}^k$

step k, the stage increments $\Delta\mathbf{Q}_{ni}^k$ of the local unknowns are computed in the first step by solving the local system of equation $\boldsymbol{L}_{ni}^k$ while keeping the stage increments $\Delta\mathbf{U}_{ni}^k$ of the global unknowns fixed. After that, the global sparse linear FE system is solved. Thereby, the dependence of the global system on local equations is considered in the linearisation (algorithmically consistent linearisation, cf. Simo & Taylor, 1985).

Giving a practical explanation, the local equation system is employed to determine the accompanying reference configuration, which is calculated using a fixed actual configuration. Thereafter, the actual configuration is determined iteratively, keeping the accompanying reference configuration fixed.

6.1.4. Classical numerical implementation

The solution strategy described in the previous section is implemented in a single monolithic application. Following this, a modular FE framework, which provides a DIRK

[10] *Philipp Ludwig von Seidel* (1821–1896): German mathematician and physicist and astronomer, who published in 1874 the *Gauss-Seidel* method for the iterative solution of linear equations.

algorithm for the solution of global and local DAE and supports mixed finite elements with individual test and trial functions for each global degree of freedom, is extended by appropriate subroutines that provide the physics of the problem, i. e., the weak formulation. This approach, focussing only on one specific module is often referred to as *programming in the small* (DeRemer & Kron, 1976). It is characterised by focussing on rather small pieces of code, which, in general, can be programmed by a single person, who understands the intended function and the computational framework.

6.2. Service-oriented solution strategy

In contrast to the monolithic solution method described in the previous section, the problem is divided into several subproblems in a service-oriented solution strategy. These subproblems are treated by specific, tailored services that are coupled to a web-service application (Papazoglou & Georgakopoulos, 2003). This approach is particularly beneficial if subproblems with different requirements can be identified.

6.2.1. Staggered solution scheme

The solution of the global mechanical problem requires a special treatment using mixed finite elements and an implicit time integration scheme, cf. subsection 6.1.2. Finite element solvers that meet these requirements are either purely scientific or expensive and require a user with a domain-specific expert knowledge for their control and adaptation.

The biological subproblem, on the other side, results in a system of ordinary differential equations, which can be treated by numerous proprietary and free software applications, each of which focussing on a specific aspect, e. g., usability, solution time, accuracy, hardware requirements, etc. Hence, splitting the problem allows for the use of tailored solution strategies for each subproblem, and therefore, reduces the numerical effort of the potentially expensive solid-fluid-interaction simulation.

For this reason, the coupled system presented in the previous section is split into three parts. As described in subsection 6.1.3, the local integration point systems containing the biological submodel, are separated from the rest and solved using a block *Gauss-Seidel* time integration strategy. Furthermore, the global DAE system is split into a purely mechanical part, containing the solid displacement and the pore-fluid pressure as degrees of freedom, and a chemical part containing the growth energy. The data transfer between the subsystems is again performed following a block *Gauss-Seidel* strategy. Thereby, the mechanical part predicts the kinematics of the solid and fluid constituents, and the chemical part advances the motion of the growth energy. Precisely speaking, the mechanical problem is solved employing a standard porous-media model, and the diffusion-reaction equation is solved by the chemical part. While the arguments for the former split are quite obvious, the reasons for the latter are more subtle and require the consideration of

the resulting system of equations:

$$\mathcal{G}_{\boldsymbol{u}}^{h} = \underbrace{\left[\begin{array}{ccc:c} \mathbf{0} & \mathbf{0} & \mathbf{0} & \\ \boldsymbol{M}_{12} & \mathbf{0} & \mathbf{0} & \\ \hdashline \mathbf{0} & \mathbf{0} & \mathbf{0} & \end{array}\right]}_{\boldsymbol{M}} \underbrace{\left[\begin{array}{c} \dot{\mathbf{u}}_S \\ \dot{\mathbf{p}} \\ \dot{\mathbf{c}} \end{array}\right]}_{\dot{\mathbf{u}}} + \underbrace{\left[\begin{array}{ccc:c} \boldsymbol{K}_{11} & \boldsymbol{K}_{12} & \mathbf{0} & \\ \mathbf{0} & \boldsymbol{K}_{22} & \mathbf{0} & \\ \hdashline \mathbf{0} & \mathbf{0} & \boldsymbol{K}_{33} & \end{array}\right]}_{\boldsymbol{K}} \underbrace{\left[\begin{array}{c} \mathbf{u}_S \\ \mathbf{p} \\ \mathbf{c} \end{array}\right]}_{\mathbf{u}} - \underbrace{\left[\begin{array}{c} \mathbf{f}_u \\ \mathbf{f}_p \\ \hdashline \mathbf{b}_c + \mathbf{f}_c - \mathbf{c}_c \end{array}\right]}_{\mathbf{f}} = \mathbf{0}\,. \tag{6.20}$$

Herein, the first two rows contain the fluid-structure-interaction problem, which is totally decoupled from the solution of the chemical subproblem. The third row contains the chemical subproblem, where $\mathbf{c}_c$

$$\mathbf{c}_c = \boldsymbol{M}_{13}\,\dot{\mathbf{u}}_S^* + \boldsymbol{K}_{23}\,\mathbf{p}^* \tag{6.21}$$

represents the coupling terms, where $\dot{\mathbf{u}}_S^*$ and $\mathbf{p}^*$ are the results computed by solving the mechanical subproblem. It can be seen that the chemical subproblem results in an algebraic equation, which can be solved without time integration. Furthermore, this kind of splitting scheme enables the parallel calculation of multiple solutes in a distributed environment. Thus, the number of considered solutes is only limited by the number of available processors, and additional metabolites might be included without blowing up the system size of the mechanical submodel.

6.2.2. Web-service technology

From the computational point of view, the previously described splitting strategy fits perfectly into the idea of service-oriented architectures (SOA), where the numerical functionality is separated into several services (Zeppenfeld & Finger, 2009). Thereby, SOA provide an abstract view on the considered processes. From the technical point of view, the services are self-contained modules, which are deployed in a distributed environment and dynamically invoked over the network by service-based applications. Thereby, a service is in general independent from the individual application context in which it is used. The software components are loosely coupled.

Although the service-oriented concept is not restricted to a certain technology, web services are the most common way of implementation. Web-service technology is not a new technology but rather a collection of existing standards and technologies to describe, publish, discover, coordinate and configure services (Zeppenfeld & Finger, 2009, p. 64; Papazoglou, 2008, p. 11). Precisely speaking, web-service technology summarises XML-based data usable for message exchange, which are widely accepted standards for the interprocess communication via internet-based protocols. The web-service core standards are SOAP[11] and WSDL (Weerawarana *et al.*, 2005).

[11] orignally defined as Simple Object Access Protocol but this acronym was dropped in Version 1.2 of the standard

SOAP is an XML-based extensible messaging architecture that includes protocols used by web services for the message exchange among each other. SOAP is not restricted to a specific transport protocol, but it commonly uses the hypertext transfer protocol (HTTP). Thereby, the SOAP message becomes the body of an HTTP message, which is sent to the service endpoint specified in the WSDL file of the invoked service.

WSDL (Web Service Description Language) is used to describe the web service and to specify its public interface in a machine-readable fashion. The WSDL essentially consists of two parts: the service interface definition describing the general web-service structure and the service implementation part, where the abstract interfaces are bind to a specific address. The WSDL file can be interpreted as a contract between the service provider and the service clients on the common interface.

For additional information on the web-service standards and technologies that are based on them, the interested reader is referred to Papazoglou (2008) and other related textbooks.

Scientific workflows

In a business application, a business process defines the logical order of tasks and activities performed by humans or machines to achieve a defined business outcome. A workflow contains those parts of the business process that are executed on computers (Leymann & Roller, 1999). Here, workflow technology is used to aggregate the domain-specific simulation services to an integrative simulation. Thereby, the workflow model defines the control flow, which is instantiated via the workflow management system.

The Web Service Business Process Execution Language (WS-BPEL) has emerged as the standard for modelling and execution of web-service-based workflows. Although web-service and workflow technologies have been established in the business area, they become more important also in scientific research (cf. Taylor *et al.*, 2007). Scientific applications impose additional requirements on the workflow lifecycle and the management of huge amounts of data (Görlach *et al.*, 2011).

6.2.3. Numerical implementation

Following the SOA paradigm, each service runs independent from its context. Hence, to implement the splitting strategy, it is sufficient to use tailored legacy applications for each subproblem. To integrate these applications, which are in general not intended to be executed as services in a distributed environment, a web-service wrapper must be provided for each application to enable the communication via web-service protocols. The most fundamental patterns for the integration of legacy applications into a service-oriented environment can be found in Erl (2009, Chap. 15).

We distinguish between static and interactive legacy applications. No interaction is possible with a static application during its execution, and hence, all parameters must be

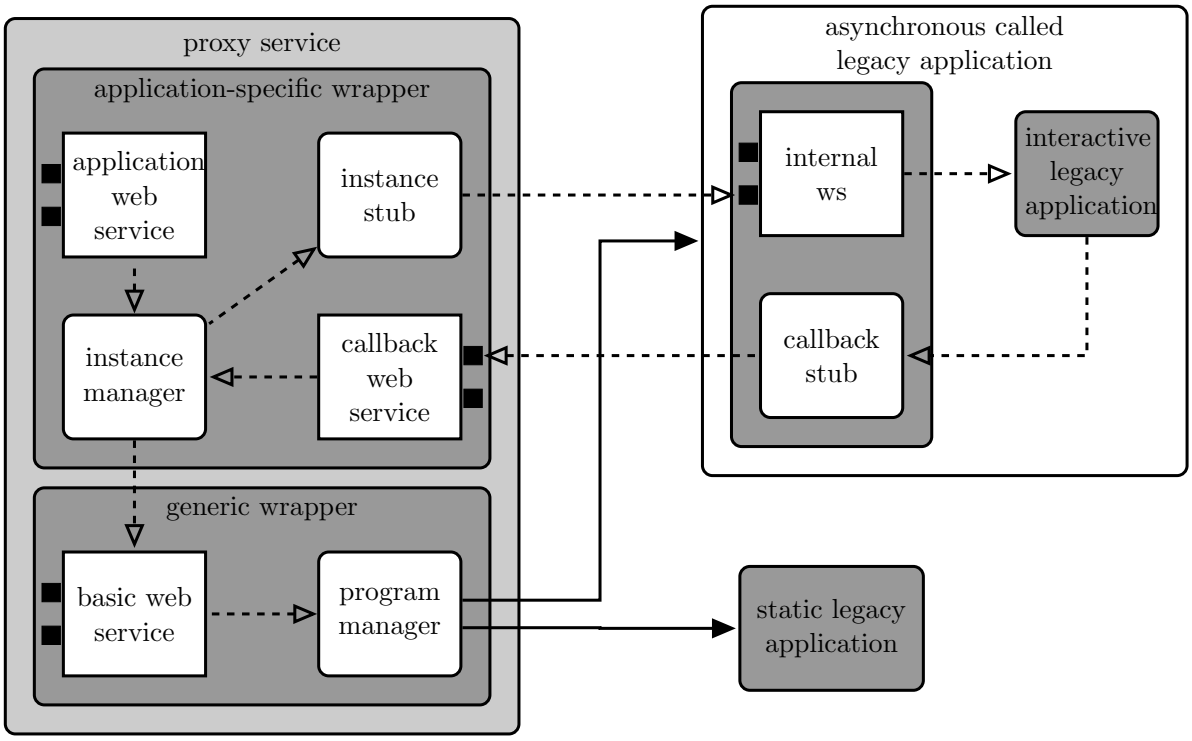

Figure 6.1.: Web-service wrapper for legacy application.

set before the application is invoked. As a consequence, the application can be directly connected to a corresponding web-service wrapper. Whenever the service is invoked, the service wrapper starts the application with the parameters specified in the SOAP message and returns the results after termination.

In contrast, an interactive application requires interactions with the executing wrapper during its execution. After invocation, it waits for further parameters and commands. Hence, it requires a more sophisticated interface, which enables the communication with the simulation during its execution. Moreover, the wrapper must be aware of applications internal states, e. g., waiting, executing, terminating, and monitoring the internal parameters, e. g., current time step, residual norm, etc.

The software architecture of the proxy service for static and interactive legacy applications is depicted in Figure 6.1. Therein, the generic adapter contains reusable modules that are application independent. The application logic is included in the application plug-in.

The *generic wrapper* is responsible for starting and stopping the legacy application. The *program manager* contains the procedures needed to start applications and to return the results after termination. If the program manager supports a remote program execution, e. g, via secure shell, the legacy application might be executed on a different server. The *basic web service* provides the web-service interface for the program manager. For static applications it is fully sufficient to use only the generic wrapper.

Interactive applications need a more sophisticated interface, which is provided by an *application-specific wrapper*. Each application instance is represented by an *instance*

manager, which is responsible for tracking the live-cycle of the application instance and responds to the SOAP messages received by the *application web service*. Depending on the incoming message, the application web service forwards the incoming messages to the correct instance manager, which creates a new instance of the legacy application by asynchronously calling the basic web service or forwards the message to the *instance stub*, which sends all incoming messages to the *internal web service* of the application instance. In addition, the instance manager checks weather the incoming messages are consistent with the instance state and responds to messages concerning variables kept by the proxy service. Via the *callback stub*, messages concerning the internal state and parameters are send to the instance manager. A basic callback stub that allows for the observation of an arbitrary internal variable of the legacy application is given in Appendix C. Thereby, the *callback web service* distributes the incoming callback messages to the instance manager and other registered observers. Note that the internal web server as well as the callback web service are internal services, which are not part of the public web-service interface. Furthermore, the internal web service as well as the callback service stub can be implemented either directly into the legacy application or realised as an external service using the standard input and output streams for the communication with the legacy application.

Due to the large communication overhead in XML-files, it is not recommended to transfer large amounts of data via SOAP messages. We have realised the data transfer among the simulation instances using SIMPL (SimTech, Information Management, Processes, and Languages) - an extensible framework that provides a generic abstraction for data management and data provisioning in simulation workflows. SIMPL offers a unified data access service by means of generic access operations for arbitrary data resources as well as special data-management activities to use these access operations directly within workflow models (Reimann *et al.*, 2011). On top of this, data management patterns enable scientists to define the data provisioning in simulation workflows in an abstract manner. Therewith, only the address of the data must be transferred via the web-service interface.

Chapter 7: Numerical examples

In this chapter, the presented model is applied to different biological tissues. The constitutive equations for the effective solid stress tensor $\mathbf{T}_E^S$ and the solid volume production $\hat{n}^S$ provide the tissue-specific material laws for tumour growth and bone remodelling. Coupled, three-dimensional numerical simulations reveal the full capacity of the described modelling approach. The presented examples are obtained using the finite-element package PANDAS[1], an adaptive finite-element tool designed for the solution of coupled multi-phase problems. During the simulations, the time-step size is automatically adapted depending on the number of required *Newton* iterations. If less than five *Newton* steps are needed to converge, the time-step size is enlarged. If more than ten *Newton* steps are needed, the time-step size is reduced.

7.1. Avascular tumour growth

Avascular tumours are neoplasms without blood vessel supply. The required nutrients are transported into the tumour tissue by diffusion, and only those cells, which are adequately supplied, are proliferating and contribute to the growth of the tumour spheroid. Cells inside the tumour spheroid, which lack in nutrients, are either in a quiescent state or form a necrotic core.

The mechanical part of the solid extra stress $\mathbf{T}^S_{E/\mathrm{mech}}$ is described by a neo-*Hooke*an[2] elasticity law. In addition, following Ambrosi & Preziosi (2002), cell adhesion and repulsion are considered via the growth-dependent part of the extra stress tensor $\mathbf{T}^S_{E/\mathrm{grow}}$:

$$\begin{aligned}
\mathbf{T}^S_{E/\mathrm{mech}} &= \frac{1}{\det \mathbf{F}_S}\Big(\mu^S(\mathbf{B}_S - \mathbf{I}) + \lambda^S \ln(\det \mathbf{F}_S)\mathbf{I}\Big)\,, \\
\mathbf{T}^S_{E/\mathrm{grow}} &= -n^S p^S_{\mathrm{grow}}\,\mathbf{I} \\
\text{with}\quad p^S_{\mathrm{grow}} &= \begin{cases} \alpha \dfrac{n^S}{n^{S\!n}} \dfrac{(n^S - n^{S\!t})^2 (n^S - n^{S\!n})}{\sqrt{1 - n^S}} & \text{for}\quad n^S \geq n^{S\!t}\,, \\ 0 & \text{for}\quad n^S < n^{S\!t}\,. \end{cases}
\end{aligned} \tag{7.1}$$

Therein, p^S_{grow} denotes the growth pressure with $n^{S\!t}$ the cell-interaction threshold and $n^{S\!n}$ as the solid volume fraction at the natural state, where neither cell repulsion nor attraction occur. This state can be seen as the ideal, desired state. In areas with a solid volume fraction below the cell-interaction threshold $n^{S\!t}$, no interactions between the cells are possible since the cells are too far from each other to interact. If the solid volume fraction n^S exceeds the value $n^{S\!n}$, the cells are repulsing each other, and if $n^{S\!t} < n^S < n^{S\!n}$,

[1] **P**orous media **A**daptive **N**onlinear finite-element solver based on **D**ifferential **A**lgebraic **S**ystems (`http://www.get-pandas.com`)

[2] *Robert Hooke* (1635–1703): English philosopher and polymath, who discovered the law of elasticity.

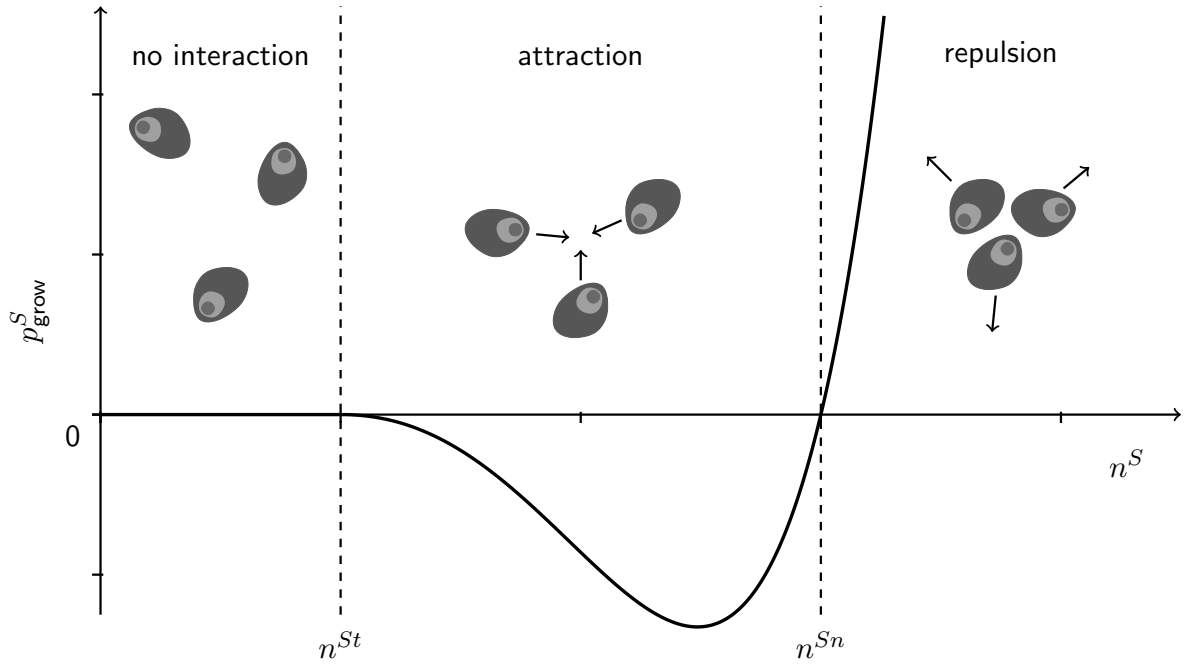

Figure 7.1.: Qualitative plot of the growth pressure p^S_{grow} as a function of the the solid volume fraction $n^S \in]0,1[$.

the cells are attracting each other. A qualitative plot of p^S_{grow} is given in Figure 7.1.

As a consequence from the thermodynamic considerations in Section 5.3.2, cell proliferation is only possible if the growth energy exceeds a certain threshold value. Concerning the degenerative process, here only necrotic cell death caused by malnutrition (nutrient starvation) is considered. Thereby, it is assumed that the considered tumour cells have lost their ability to initiate an apoptotic cell death. Accordingly, the solid volume production is calculated by employing a *Mechalis*[3]*-Menten*[4]-type reaction equation, where the regenerative process is considered if the growth-energy exceeds the threshold $\mathcal{C}^F_0$, and the degenerative process is considered if the growth-energy is below this threshold:

$$\hat{n}^S = \begin{cases} \hat{n}^S_{\text{reg}} = \gamma\, n^S n^F \dfrac{\mathcal{C}^F - \mathcal{C}^F_0}{K_M^{\mathcal{C}+} + (\mathcal{C}^F - \mathcal{C}^F_0)} & \text{if} \quad \mathcal{C}^F > \mathcal{C}^F_0\,, \\ \hat{n}^S_{\text{deg}} = \delta\, n^S n^F \dfrac{\mathcal{C}^F_0 - \mathcal{C}^F}{K_M^{\mathcal{C}-} + (\mathcal{C}^F_0 - \mathcal{C}^F)} & \text{if} \quad \mathcal{C}^F \leq \mathcal{C}^F_0\,. \end{cases} \tag{7.2}$$

In these *Michaelis-Menten* equations, $K_M^{\mathcal{C}+}$ and $K_M^{\mathcal{C}-}$ denote the *Michaelis* constants representing the growth energy at which the volume production is half of its maximum.

[3] *Leonor Michaelis* (1875–1949): German biochemist, physical chemist, and physician known for his work on enzyme kinetics. In 1922 he left Germany and became the first foreign professor at a Japanese university.

[4] *Maud Leonora Menten* (1879–1960): Canadian physician and the first woman who became a doctor of medicine in Canada. In 1912 she moved to Berlin where she worked together with *Leonor Michaelis* on enzyme kinetics.

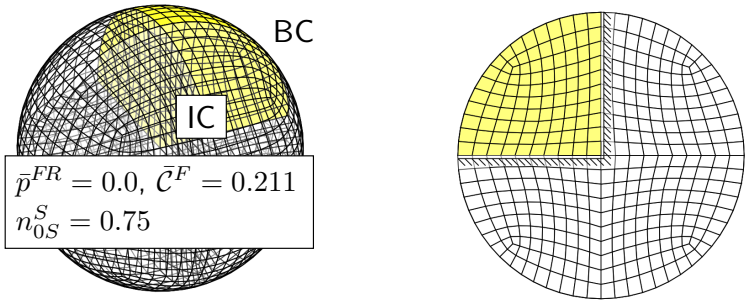

Figure 7.2.: Considered initial-boundary-value problem adopted from Ehlers *et al.* (2009): One eighth of an ideal sphere 50μm in diameter with an initial solid volume fraction of $n^S_{0S} = 0.75$. Symmetry boundary conditions are applied on the inner surfaces.

As numerical examples, three avascular tumours with different proliferation rates are calculated. It is taken into account that tumour cells differ in proliferation rate depending on tumour type and malignancy. The volume is discretised by 896 finite elements using 20-noded brick elements. The results are obtained by calculating one eighth of an unloaded tumour spheroid with an initial diameter of 50 micrometer, cf. Figure 7.2. The initial and boundary conditions are adopted from Ehlers *et al.* (2009). Thereby, symmetry conditions are applied on the inner surfaces. On the outer surface, a pore pressure of zero (fully drained condition) and a growth-energy value that lies inside the physiological range are applied and held constant during the calculation.

The simulations proceed from an initial volume fraction of $n^S_{0S} = 0.75$ as well as the material parameters given in Table 7.1 and varying proliferation coefficients $\gamma = \{3.0 \times 10^{-5}, 1.5 \times 10^{-5}, 7.5 \times 10^{-6}\}$ [cm^3/(J s)]. In Figure 7.3, the ratios of the computed tumour radii to the initial radius are depicted and compared to in-vitro experiments (Schwachöfer *et al.*, 1991). Figure 7.4 depicts results of the qualitative 3-d simulations. The colouring indicates the distribution of the tumour cell volume fractions. Within the spheroids, three regions can be identified: the outer rim (red), where the cells are proliferating, a transient region with quiescent cells (yellow) and the necrotic core without living cells (blue). At the end of the simulation depicted in Figure 7.4, top right, the tumour surface begins to buckle. This results from the fact that the tumour surface grows faster than the inner domain yielding surface instabilities, which can also be observed in in-vitro experiments. Following Byrne (2003), the linear increasing volume indicates a surface growth during the layering phase of avascular tumour growth. The decrease of the slope at the end of the calculation indicates the beginning of the plateau phase. As can be seen, the model is in principle capable in mimicking the biologically correct growth behaviour. However, more investigations are necessary to provide reliable and cell-type specific predictions.

Table 7.1.: Material parameters used for the tumour growth example.

Parameter	Symbol	Value	SI unit
1st Lamé constant of the solid skeleton	λ^S	5×10^{-5}	$\mathrm{N/cm^2}$
2nd Lamé constant of the solid skeleton	μ^S	1.0×10^{-5}	$\mathrm{N/cm^2}$
Effective density of dense solid	ρ^{SR}	1.3×10^{-3}	$\mathrm{kg/cm^3}$
Effective density of pore fluid mixture	ρ^{FR}	1.0×10^{-3}	$\mathrm{kg/cm^3}$
Darcy permeability	k^F	3.0×10^{-2}	cm/s
Natural solid volume fraction	n^{Sn}	0.75	—
Cell interaction threshold	n^{St}	0.65	—
Growth stress constant	α	50	$\mathrm{N/cm^2}$
Tumour proliferation coefficient	γ	variant	$\mathrm{cm^3/(J\,s)}$
Tumour necrosis coefficient	δ	1.5×10^{-5}	1/s
Boundary and initial pore pressure	$\bar{p}^{FR}$	0.0	$\mathrm{N/cm^2}$
Boundary and initial growth-energy value	$\bar{\mathcal{C}}^F$	2.11×10^{-1}	$\mathrm{J/cm^3}$
Growth-energy threshold value	$\mathcal{C}_0^F$	1.05×10^{-1}	$\mathrm{J/cm^3}$
Basal metabolic growth-energy consumption	k_{basal}	1.0×10^{-4}	$\mathrm{J/(cm^3\,s)}$
Additional growth-energy consumption	k_{grow}	60.0	$\mathrm{J/cm^3}$
Growth-energy diffusion coefficient	$D^{\mathcal{C}}$	2.0×10^{-8}	cm/s
Michaelis constant	$K_M^{\mathcal{C}+}$	3.0×10^{-2}	$\mathrm{J/cm^3}$
Michaelis constant	$K_M^{\mathcal{C}-}$	2.0×10^{-2}	$\mathrm{J/cm^3}$

7.2. Bone remodelling

In contrast to the development of tumours, which depends only on the availability of growth energy, the remodelling of bones is triggered by the local mechanical loading situation. Following Wolff (1892), the bone matrix is built in regions with a high stress level and removed from regions with low stress level. The material and energy needed to construct the bone matrix is transported through the extracellular fluid by diffusion. As a consequence, the growth energy constricts the bone matrix accretion, but has no influence on the direction of the remodelling process. In contrast to classical considerations, where the density development depends only on the mechanical stresses inside the tissue, the presented growth-energy-dependent approach allows for the consideration of malnutrition.

The effective solid stress is calculated using the linear *Hooke*an elasticity law

$$\mathbf{T}_E^S = 2\mu^S \boldsymbol{\varepsilon}_S + \lambda^S (\boldsymbol{\varepsilon}_S \cdot \mathbf{I})\mathbf{I} \quad \text{with} \quad \boldsymbol{\varepsilon}_S = \tfrac{1}{2}[\mathrm{Grad}_S\, \mathbf{u}_S + (\mathrm{Grad}_S\, \mathbf{u}_S)^T] \tag{7.3}$$

as the linear solid strain tensor. Moreover μ^S and λ^S denote the growth-dependent *Lamé*[5] parameters, which are functions of the growth process and are obtained from experiments

[5] *Gabriel Léon Jean Baptiste Lamé* (1795–1870): French mathematician known for his work on differential geometry and elasticity.

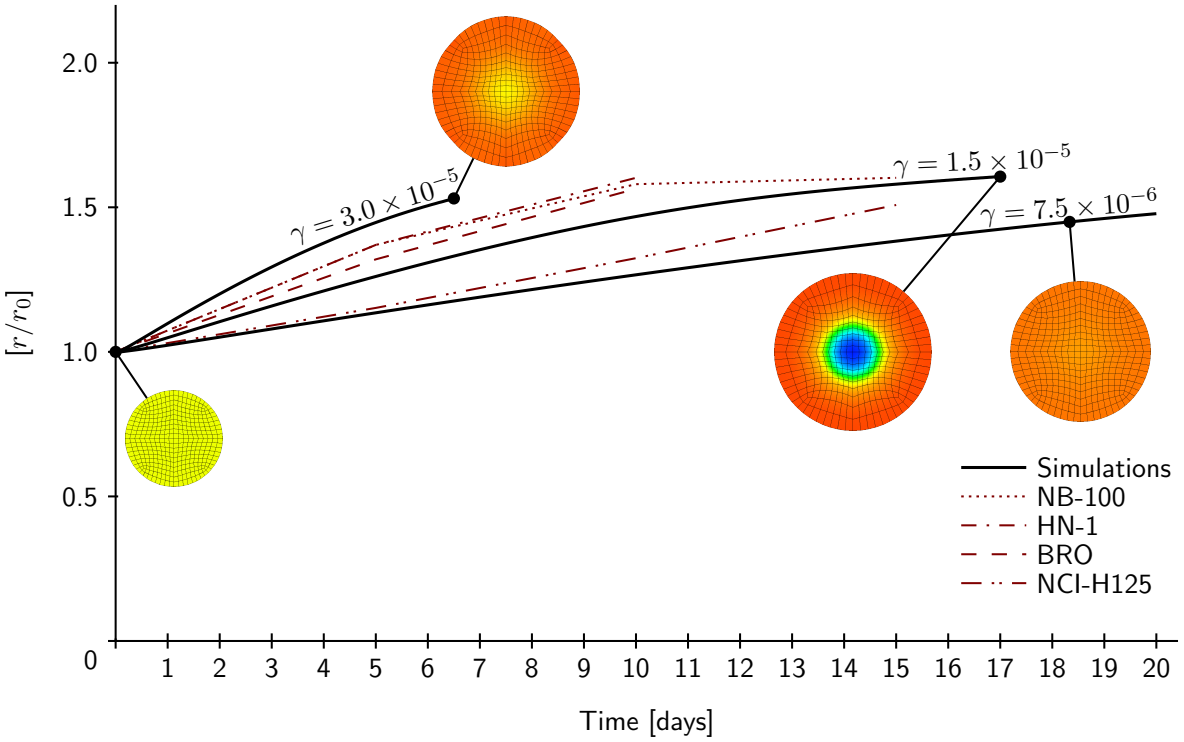

Figure 7.3.: Computed outer tumour radius related to the initial radius compared with experimental data given by Schwachöfer *et al.* (1991, Figure 1, 100μg/ml) for four different tumour cell types.

by Carter & Hayes (1977):

$$\mu^S(n^S_{tS}) = \Big(\frac{n^S_{tS}}{n^S_{0S}}\Big)^m \mu^S_{0S} \quad \text{and} \quad \lambda^S(n^S_{tS}) = \Big(\frac{n^S_{tS}}{n^S_{0S}}\Big)^m \lambda^S_{0S}\,. \tag{7.4}$$

Therein, μ^S_{0S} and λ^S_{0S} denote the values of the *Lamé* parameters at the initial solidity n^S_{0S}, and the parameter m governs the non-linearity of the stiffness increase during growth. Note that, for simplicity, the anisotropic behaviour of bones is not taken into account here.

The solid volume production is calculated by employing again a *Michaelis-Menten*-type reaction equation, which is a standard equation for the description of enzyme reaction velocities (cf. Löffler, 2008, p. 39):

$$\hat{n}^S = \begin{cases} \dfrac{\hat{n}^S_{\max}(\mathcal{C}^F - \mathcal{C}^F_0)}{K^+_m + (\mathcal{C}^F - \mathcal{C}^F_0)} & \text{if} \quad \hat{n}^S_{\max} > 0 \quad \text{and} \quad \mathcal{C}^F > \mathcal{C}^F_0\,, \\ \dfrac{\hat{n}^S_{\max} n^S}{K^-_m + n^S} & \text{if} \quad \hat{n}^S_{\max} < 0\,. \end{cases} \tag{7.5}$$

Therein, the production rate increases with increasing substrate concentration $\mathcal{C}^F$ or n^S, asymptotically approaching the maximum rate $\hat{n}^S_{\max}$. Furthermore, the Michaelis con-

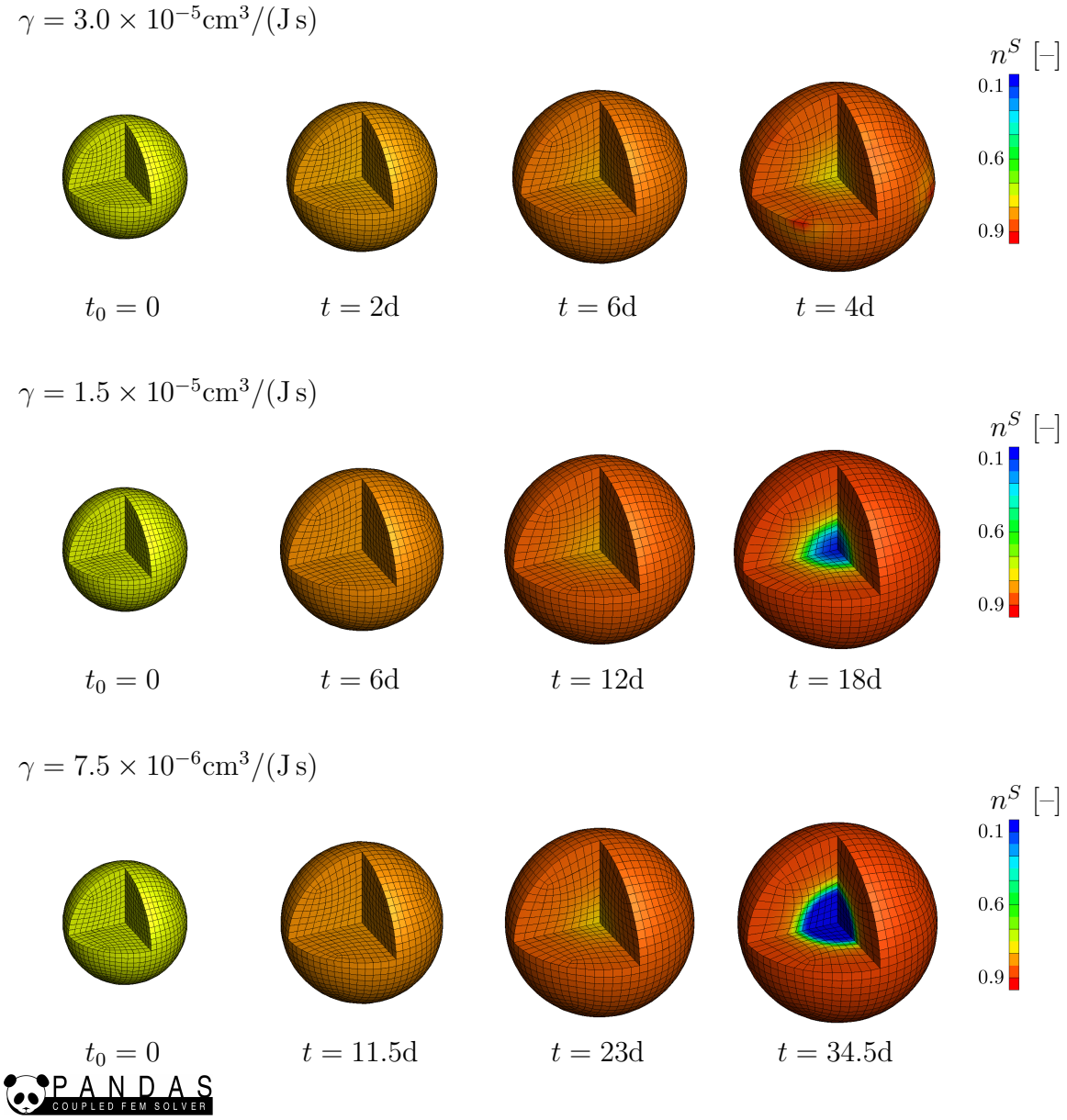

Figure 7.4.: Qualitative 3-d simulation results of a growing avascular tumour spheroid mapped with the distribution of the volume fraction of living tumour cells for different proliferation coefficients γ.

stants K_m^+ and K_m^- mark the substrate concentration $\mathcal{C}^F$ or n^S at which the production rate reaches half of its maximum value. The maximum production rate $\hat{n}^S_{\max}$ is adopted from Nackenhorst (1997):

$$\hat{n}^S_{\max} = k^S A^S (W^S - W^S_{\mathrm{atr}}) \quad \text{with} \quad W^S = \tfrac{1}{2}\mathbf{T}^S_E \cdot \boldsymbol{\varepsilon}_S \,. \tag{7.6}$$

Herein, $\hat{n}^S_{\max}$ is positive if the solid strain energy W^S is above the attractor stimulus W^S_{atr}, and negative if it is below. Moreover, A^S is the volume-specific surface area (see, e. g., Beaupré *et al.*, 1990), and k^S is the growth-rate coefficient.

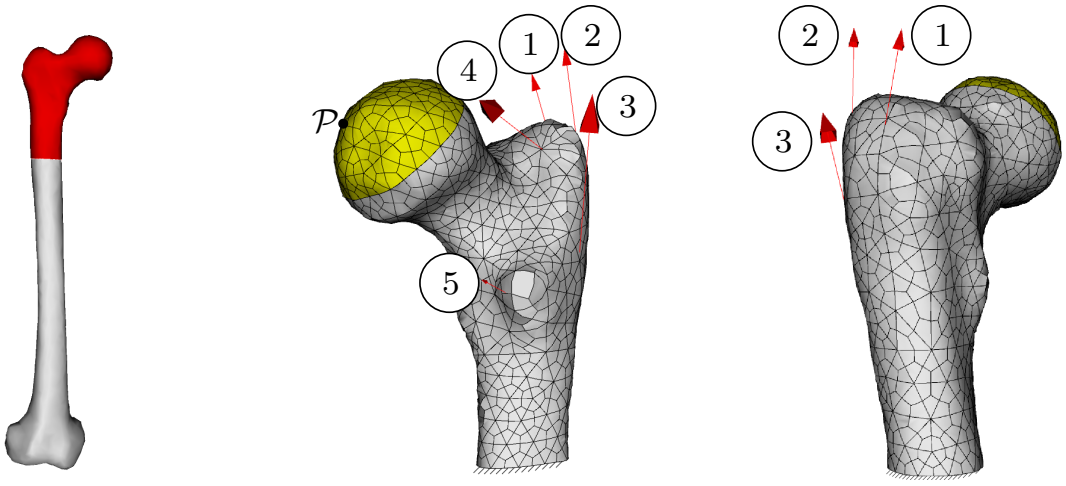

Figure 7.5.: Considered initial-boundary-value problem of the upper femur. Left: discretised part of the whole femur (red). Centre and right: considered boundary conditions: muscle forces (red, 1–5), hip joint (yellow), fixed displacement at the bottom surface and constant pore-fluid pressure and growth-energy value at the surrounding surfaces (grey).

Table 7.2.: Material parameters used for the bone remodelling example.

Parameter	Symbol	Value	SI unit
1st *Lamé* constant of the solid skeleton	λ^S	9.3055×10^5	$\mathrm{N/mm^2}$
2nd *Lamé* constant of the solid skeleton	μ^S	3.877×10^5	$\mathrm{N/mm^2}$
Stiffness parameter	m	3.0	–
Effective density of dense solid	ρ^{SR}	2.1×10^{-6}	$\mathrm{kg/mm^3}$
Effective density of pore fluid	ρ^{FR}	1.0×10^{-6}	$\mathrm{kg/mm^3}$
Darcy permeability	k^F	3.0×10^{-2}	mm/s
Initial volume fraction of solid	n^S_{0S}	0.1	–
Growth-rate coefficient	k^S	1.0	1/s
Attractor stimulus	W^S_{atr}	6.0×10^{-6}	$\mathrm{J/mm^3}$
Boundary and initial pore pressure	$\bar{p}^{FR}$	0.0	$\mathrm{N/cm^2}$
Boundary and initial growth-energy value	$\bar{\mathcal{C}}^F$	variant	$\mathrm{mJ/mm^3}$
Growth-energy threshold value	$\mathcal{C}^F_0$	1.5×10^{-1}	$\mathrm{mJ/mm^3}$
Basal metabolic growth-energy consumption	k_{basal}	1.0×10^{-8}	$\mathrm{mJ/mm^3\,s}$
Additional growth-energy consumption	k_{grow}	1.5×10^{-4}	$\mathrm{mJ/mm^3}$
Growth-energy diffusion coefficient	$D^{\mathcal{C}}$	6×10^{-1}	mm/s
Michaelis constant	K^+_M	3.0×10^{-1}	$\mathrm{mJ/mm^3}$
Michaelis constant	K^-_M	1.0×10^{-2}	–

To give an example, the remodelling within the upper part of a human femur is calculated with geometry data obtained by courtesy of Van Sint Jan *et al.* (2003). The volume was

Table 7.3.: Considered muscle and joint forces.

Name	Value	SI unit	unit direction vector
Musculus gluteus minimus (1)	300	N	$\mathbf{f}_0 = \frac{1}{\sqrt{109}}(3,0,10)^T$
Musculus gluteus medius (2)	290	N	$\mathbf{f}_0 = \frac{1}{\sqrt{113}}(3,2,10)^T$
Musculus gluteus maximus (3)	550	N	$\mathbf{f}_0 = \frac{1}{\sqrt{38}}(2,3,5)^T$
Musculus piriformis (4)	500	N	$\mathbf{f}_0 = \frac{1}{\sqrt{129}}(10,5,2)^T$
Musculus iliacus (5)	100	N	$\mathbf{f}_0 = \frac{1}{\sqrt{129}}(2,-10,5)^T$
Hip joint	-1900	N	$\mathbf{f}_0 = \frac{1}{\sqrt{41}}(4,1,36)^T$

discretised into 876 finite elements using 20-noded brick elements. During the simulation, the displacement at the bottom surface is fixed, the muscle and joint forces that characterise the loading conditions at an upright standing state are applied, cf. Figure 7.5. The load is applied in three steps. To avoid convergence problems, at the beginning only 10% of the full load is applied, after ten seconds the load is increased to 50%, and after another ten seconds the full load is subjected. Furthermore, on the outer bone surface, i. e. all surfaces except the bottom surface, the pore pressure and the growth-energy value are kept identical to their initial values given in Table 7.2. During the initial phase, the remodelling calculation is deactivated, it starts first when the full load is applied.

Starting from an initial solid volume of $n^S_{0S} = 0.1$ and using a monolithic solution strategy, the resulting development of the solid volume fraction of two qualitative simulations with differing growth-energy boundary values $\bar{\mathcal{C}}^F$ is depicted in Figure 7.12. During the simulations, the solid volume fraction at the bone surface increases while the solid volume fraction decreases in the bone centre, where the bone marrow is situated. At first sight, the results look quite similar, but a closer look reveals a significant difference in the average solid volume fractions of both calculations (Figure 7.7). Strictly speaking, a permanent malnutrition has only a subtle influence on the macroscopic bone structure but significantly changes the resulting bone micro structure associated with a lower solid volume fraction. These changes also influence the mechanical behaviour (see Figure 7.8, where the vertical displacement of point $\mathcal{P}$ during the simulation is depicted), and are a key indicator for osteoporosis (cf. Sambrook & Cooper, 2006).

7.3. Inclusion of cell-population dynamics

In this section, a systems-biological cell population model is used for the simulation of bones. It consists of four cell types, which interact via messenger molecules. This example

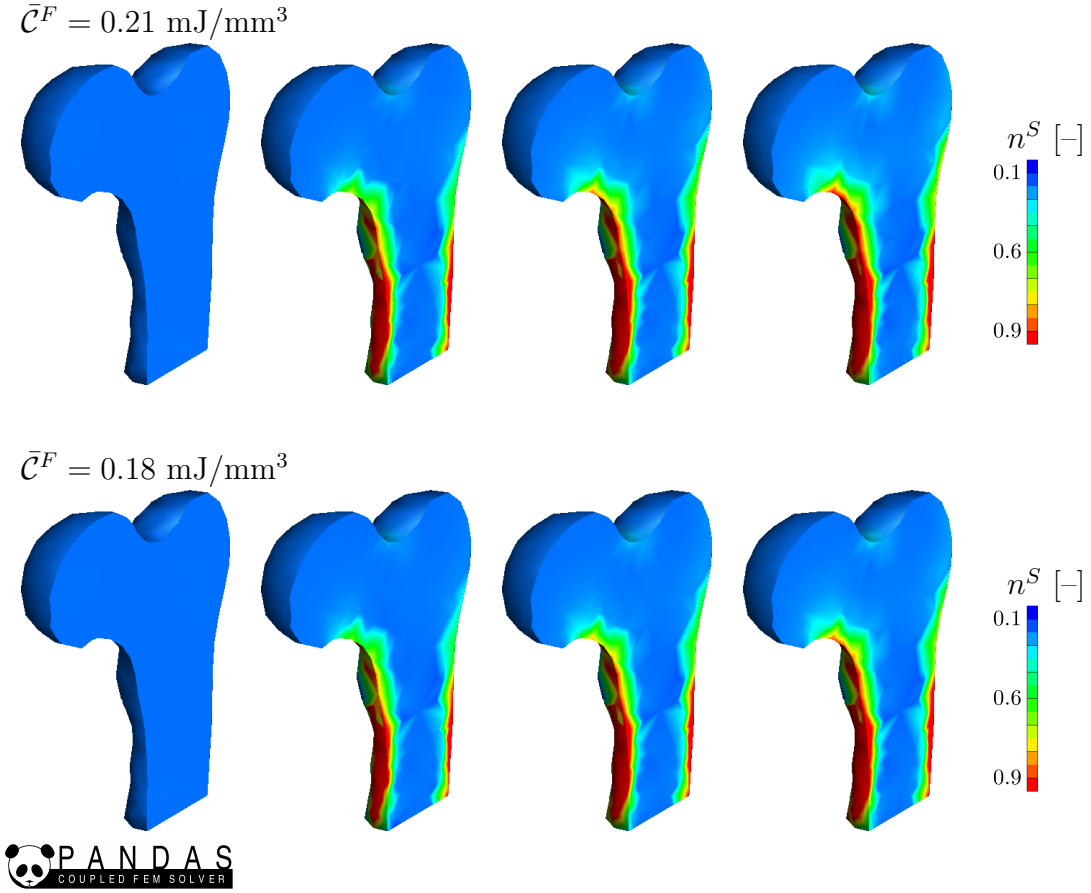

Figure 7.6.: 3-d simulation of remodelling in a human femur. The colouring indicates the development of the solid volume fraction in a loaded femur starting from an initially homogeneous distribution ($n^S_{0S} = 0.1$).

is then used to compare the results of the traditional solution strategy with the results obtained from the service-oriented solution strategy (subsection 7.3.2). Finally, to demonstrate the potential of the service-oriented solution strategy, it is used to remodelling in bones for a daily routine consisting of several activities (subsection 7.3.4).

The presented results are obtained using the finite-element package PANDAS. The simulations are invoked as web services on an Apache Tomcat[6] server, using Apache Axis2[7] as SOAP engine and Apache ODE[8] as workflow management system.

7.3.1. Systems-biological submodel

On the cellular level, the remodelling of bones results from mutual interactions among different types of bone cells. The cell types which are directly related to the remodelling process are the osteoclasts, which decompose the bone matrix, and the osteoblasts, which

[6]Apache Tomcat (`http://tomcat.apache.org/`)
[7]Apache eXtensible Interaction System (`http://ws.apache.org/axis2/`)
[8]Orchestration Director Engine (`http://ode.apache.org/`)

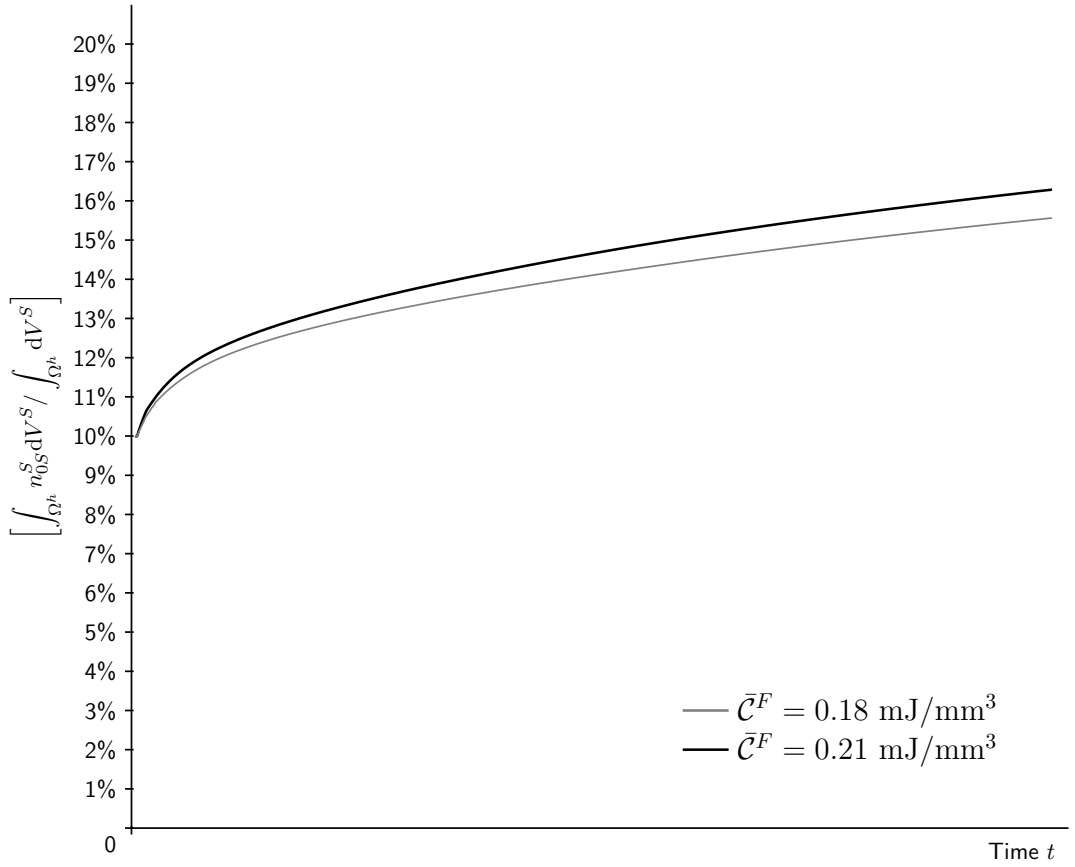

Figure 7.7.: Development of the average solid volume fraction during the simulations. Changes of the growth-energy boundary value $\bar{\mathcal{C}}^F$ significantly reduce the solid volume.

synthesise the bone matrix. Once an osteoblast gets trapped inside the bone matrix, it is transformed to an osteocyte, which acts as cellular sensor of the mechanical loading situation in the surrounding bone tissue.

The cell populations are mediated by biochemical signalling pathways. These signals depend on the signalling components, such as hormones, their emission by cells and their reception by cell surface receptors. The effects of the biochemical signalling pathways relevant for bone remodelling are modelled in detail by Lemaire *et al.* (2004) and Maldonado *et al.* (2007).

Cell-population dynamics

Proceeding from the mathematical descriptions of the cells and molecules related to bone remodelling given by Komarova *et al.* (2003); Lemaire *et al.* (2004); Maldonado *et al.* (2007), a cell-population model is developed that fits in the continuum-mechanical framework presented in this monograph. Thereby, the cell populations φ^δ and messenger molecules φ^ζ are described by their molar concentrations c_m^γ, which relate the local number

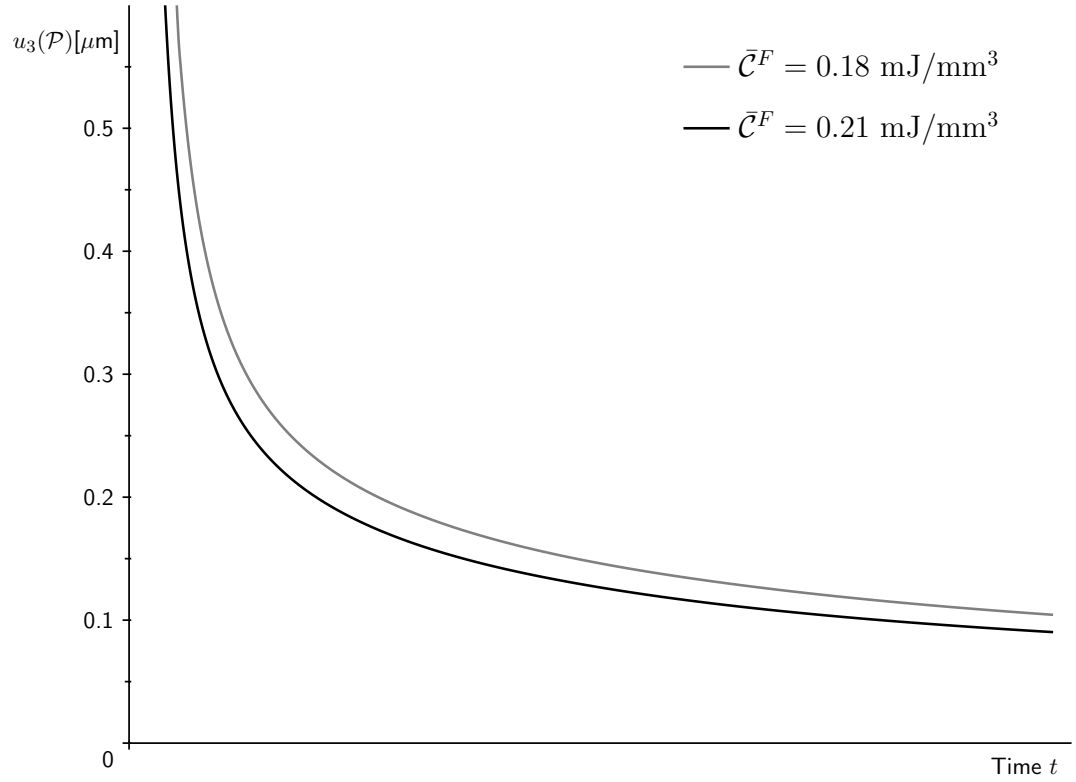

Figure 7.8.: Development of the displacement of point $\mathcal{P}$ during the simulations. Changes of the growth-energy boundary value $\bar{\mathcal{C}}^F$ significantly influence the mechanical behaviour.

of cells $\mathrm{d}n_m^\delta$ or molecules $\mathrm{d}n_m^\zeta$ to the overall volume:

$$\begin{aligned} &c_m^\gamma = \frac{\mathrm{d}n_m^\gamma}{\mathrm{d}v} \quad \text{with} \quad \gamma \in \{\delta, \zeta\}\,, \\ &\delta \in \{R, B, Y, C\} \quad \text{and} \quad \zeta \in \{T, P, L, O\}\,. \end{aligned} \tag{7.7}$$

Here, four cell populations and four messenger molecules are considered: pre-osteblasts R, osteoblasts B, osteocytes Y and osteoclasts C as well as the transforming growth-factor beta (TGF-β) T, prostagladine E_2 (PGE_2) P, receptor activator of nuclear factor kappa ligand (RANKL) L and osteoprotegerin (OPG) O. The cell-population dynamics is described by ordinary differential equations, which include cell apoptosis and cell development rates that in addition might depend on the occupancy of a specific receptor on

the cell membrane Π^ζ. In particular, we have

$$\begin{aligned}
\dot{c}_m^R &= D^R \Pi^T (1 + c_p \Pi^P) - \frac{D^B}{\Pi^T} c_m^R \,, \\
\dot{c}_m^B &= \frac{D^B}{\Pi^T} c_m^R - A^B c_m^B - D^Y c_m^B \,, \\
\dot{c}_m^Y &= D^Y c_m^B - A^Y c_m^Y \,, \\
\dot{c}_m^C &= D^C \Pi^L - A^C \Pi^T c_m^C \,.
\end{aligned} \tag{7.8}$$

Therein, A^δ and D^δ are the apoptosis and development rate coefficients of φ^δ. Note that the development of φ^δ has an increasing effect on the cell population of φ^δ, and a decreasing effect on the population of progenitor cells of φ^δ. Concerning the messenger molecules, only the occupancies Π^ζ of the messenger-specific receptors are considered. Figure 7.9 gives a schematic overview of the considered cell-population dynamics.

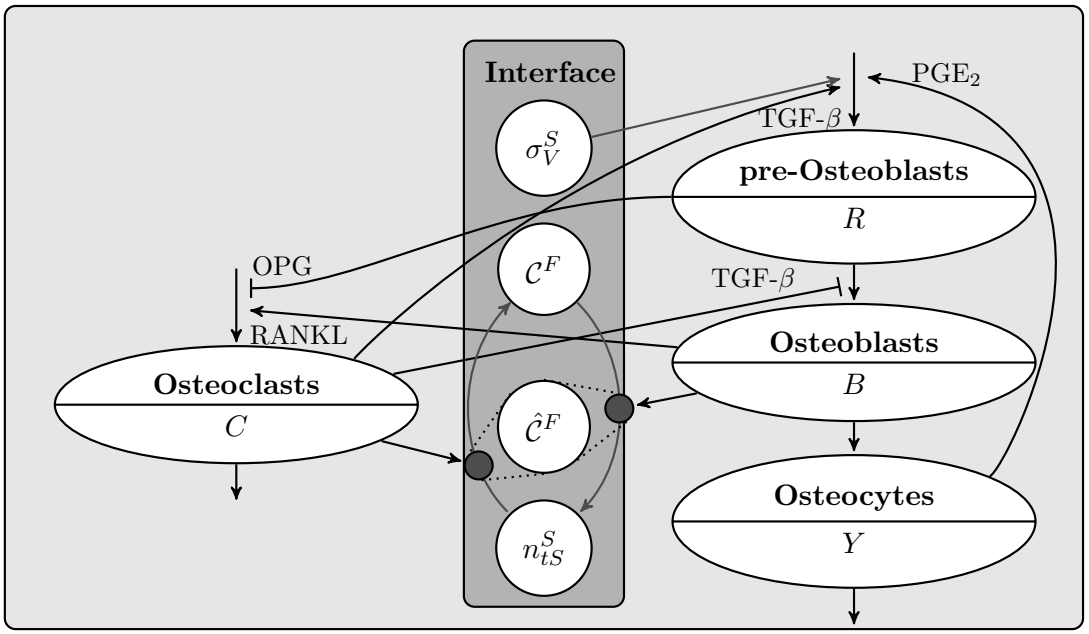

Figure 7.9.: Schematic representation of the considered cell population model.

The dynamics of the messenger molecules happens on a rather fast time scale compared to the cell-population dynamics (7.8) (Lemaire *et al.*, 2004; Maldonado *et al.*, 2007). After changes they quickly converge to a new steady equilibrium. Thus, only the equilibrium state is of interest for the cell population dynamics. Therefore, the messenger-molecule concentrations are considered to be at a quasi-steady state ($\dot{c}_m^\zeta = 0$), which leads to algebraic equations for their determination.

Following Lemaire *et al.* (2004), the differentiation of osteoblast progenitors into pre-osteoblasts and their activation are mainly triggered by the occupied TGF-β receptors,

where the occupancy is given by

$$\Pi^T = \frac{c_m^T + c_{m0}^T}{c_m^T + c_{mS}^T} = \frac{c_m^C + c_{m0}^{TC}}{c_m^C + c_{mS}^{TC}}\,, \tag{7.9}$$

where the TGF-β concentration is assumed to be proportional to the osteoclast concentration $c_m^T = \gamma^T c_m^C$ with the proportionality factor γ^T. Moreover, c_{m0}^T is the basal concentration of TGF-β, and c_{mS}^T denotes the dissociation coefficient of TGF-β with its receptor. They are related to c_{m0}^{TC} and c_{mS}^{TC} via γ^T, which are the cell-concentration equivalents of the basal concentration and the dissociation coefficient.

Furthermore, the amount of PGE_2 emitted by the octeocytes depends on the mechanical stress level. Following Maldonado *et al.* (2007), the PGE_2 concentration is given by

$$c_m^P = k^\psi \frac{\sigma_V^S\, c_m^Y}{1 + \exp(-k^\sigma \sigma_V^S - k^Y c_m^Y)} \tag{7.10}$$

with the material constants k^ψ, k^σ and k^Y. Instead of using the PGE_2 concentration directly for the calculation of the cell population, as proposed by Maldonado *et al.* (2007), where the direct, linear dependency might lead to unstable results, we introduce an additional PGE_2 receptor. The proportion of occupied PGE_2 receptors is calculated following Lemaire *et al.* (2004, cf. Eqs. 2 and 6):

$$\Pi^P = \frac{c_m^P}{c_m^P + c_{mS}^P}\,. \tag{7.11}$$

Therein, c_{mS}^P is the dissociation coefficient of PGE_2 with its receptor.

RANKL is a messenger molecule attached to the osteoblast surface. It binds to the Receptor Activator of Nuclear Factor Kappa (RANK) on the membrane of the osteoclast precursors, which initiates the osteoclast differentiation and activation, where Π^L is the RANK occupancy. This binding is inhibited by OPG, which is released by pre-osteoblasts and binds to RANKL as well. Assuming the RANKL concentration proportional to the osteoblast concentration $c_m^L = \gamma^L c_m^B$ with the proportionality factor γ^L, and the OPG concentration proportional to the pre-osteoblasts concentration $c_m^O = \gamma^O c_m^R$ with the proportionality factor γ^O, the RANK occupancy Π^L reads (Lemaire *et al.*, 2004, Eq. A.2):

$$\begin{aligned}\Pi^L &= \frac{c_m^L}{c_{mS}^L\left(1 + \dfrac{c_m^K}{c_{mS}^L} + \dfrac{c_m^O}{c_{mS}^O}\right)} \\ &= \frac{c_m^{LB}}{c_{mS}^B\left(1 + \dfrac{c_m^{KB}}{c_{mS}^{LB}} + \dfrac{c_m^R}{c_{mS}^{OR}}\right)}\,.\end{aligned} \tag{7.12}$$

Herein, c_{mS}^L is the dissociation coefficient of RANKL with RANK, which is related to c_{mS}^B via γ^L, c_{mS}^O denotes the dissociation coefficient of OPG with RANKL, which is related

to c^R_{mS} via γ^O, and c^K_{mS} marks the concentration of the receptor RANK, which is kept constant to reflect the unlimited availability of osteoclast precursors.

Remodelling process

To update the mechanical model, the changes of the solid volume fraction n^S_{tS} and the growth-energy consumption $\hat{\mathcal{C}}^F$ are calculated. The solid volume fraction n^S_{tS} is related to the solid volume production via the deformation gradient, recall (4.5):

$$(n^S_{tS})'_S = \hat{n}^S_{tS} = \hat{n}^S (\det \mathbf{F}_S)^{-1} \,. \tag{7.13}$$

And like the solid volume production n^S in (7.14), it is conceptually split into regenerative and degenerative parts

$$(n^S_{tS})'_S = \hat{n}^S_{tS\mathrm{reg}} - \hat{n}^S_{tS\mathrm{deg}} \,, \tag{7.14}$$

where the regenerative part $\hat{n}^S_{tS\mathrm{reg}}$ represents the bone-matrix formation by the osteoblasts, and the degenerative part $\hat{n}^S_{tS\mathrm{deg}}$ denotes the bone-matrix degradation by the osteoclasts. For both parts, a *Michaelis-Menten*-type reaction equation is used:

$$\begin{aligned} \hat{n}^S_{tS\mathrm{reg}} &= c^+ \frac{\mathcal{C}^F}{K^+_M + \mathcal{C}^F} \big(1 - \frac{n^S_{tS}}{n^S_{tS\mathrm{max}}}\big) c^B_m \,, \\ \hat{n}^S_{tS\mathrm{deg}} &= c^- \frac{n^S_{tS}}{K^-_M + n^S_{tS}} c^C_m \,. \end{aligned} \tag{7.15}$$

Therein, the production rates of osteoblasts and osteoclasts increase with increasing substrate concentration, asymptotically approaching the maximum rate, where $\mathcal{C}^F$ is the substrate of the regenerative part, and n^S_{tS} is the substrate of the degenerative reaction. Furthermore, the *Michaelis* constants K^+_m and K^-_m mark the substrate concentration $\mathcal{C}^F$ or n^S_{tS}, at which the production rate reaches half of its maximum value, and c^+ and c^- are material parameters. In addition, the regenerative part is limited by $n^S_{tS\mathrm{max}}$.

The growth-energy production $\hat{\mathcal{C}}^F$ summarises the basal energy consumption of the cells and an additional energy production, which results from the bone-matrix formation:

$$\hat{\mathcal{C}}^F = -k_{\mathrm{basal}}(c^R_M + c^B_m + c^Y_m) - k_{\mathrm{grow}} \hat{n}^S_{tS\mathrm{reg}} \,. \tag{7.16}$$

Herein, it is assumed that the cells of the osteoblastic cell line have the same basal-metabolic energy consumption. The osteoclasts are not considered explicitly. It is assumed that their energy demand is covered by the released energy of the bone matrix degradation.

7.3.2. Upright standing

To compare the monolithic solution strategy (Section 6.1) and the service-oriented decoupled solution strategy (Section 6.2), the remodelling processes in an upper human femur under upright standing conditions are calculated starting from an identical initial

solid volume fraction $n^S_{0S} = 0.1$. Thereby, the used geometry data was discretised into 3676 finite elements using 20-noded brick elements. During the simulation, the displacement at the bottom surface is fixed. Furthermore, on the outer bone surface, i. e. all surfaces except the bottom surface, the pore pressure and the growth-energy value are kept identical to their initial values given in Table 7.4.

Muscle and hip-joint forces The muscle and hip-joint forces on the femur under upright standing conditions were calculated by a previous, unpublished forward dynamic multi-body simulation of the whole muscular-skeletal system. The data was obtained by courtesy of S. Schmitt. Note that standing is a dynamic and periodic process where the human torso is slightly moving forward and backward. Here, we consider a characteristic sequence, depicted in Figure 7.10, with a total length of 1.65 seconds as boundary condition. The SIMPL framework (subsection 6.2.3) is used to transfer the muscle forces from the global coordinate system, used by the multi-body simulation, to the local coordinate system, used by the continuum-mechanical simulation.

Monolithic solution strategy

Traditionally, the mechanical problem is solved using a monolithic solution strategy, implemented in a single program. Thereby, the mechanical and systems-biological subproblems are solved at once. However, due to the large time-scale differences between the remodelling process and the considered boundary conditions, it is impractical to compute the solution of the combined model using the time-step size required to resolve the transient boundary conditions. Even if the required computational resources are available, the very small changes in the remodelling simulation are susceptible to an accumulation of round-off errors. Therefore, instead of applying the transient loading conditions, the averages of the characteristic sequences of the muscle and hip-joint contact forces are applied as static boundary conditions (cf. Table 7.5). The resulting developments of the solid volume fraction and the cell populations are depicted in Figure 7.11. During the simulation, the osteoblast concentration (Row 3) increases at the bone surface, where the equivalent tensile stress (Row 2) is high, while it remains constant at a low concentration in the bone centre, where the bone marrow is situated. This leads to an increase of the solid volume fraction (Row 1) at the bone surface. Here, starting from a low initial solid density, the remodelling is mostly a bone matrix formation and no removal. Therefore, the osteoclast concentration (Row 4) remains nearly constant throughout the whole domain at a very low value, compared to the osteoblast concentration.

Decoupled solution strategy

For the decoupled solution (Algorithm 3), the program that contains the monolithic solution strategy is divided into three parts, a mechanical, a chemical and a systems-biological part, that are solved individually. Thus, the global equation system is split into a mechanical part and a chemical part. The mechanical part, containing the overall momentum and the overall volume balances, predicts the kinematics of the solid and fluid constituents.

Table 7.4.: Material parameters used for the bone remodelling example (The molar concentration is given in molar M i. e. 1mol/dm^3).

Parameter	Symbol	Value	SI unit
1st *Lamé* constant of the solid skeleton	λ^S	9.3055×10^5	N/mm^2
2nd *Lamé* constant of the solid skeleton	μ^S	3.877×10^5	N/mm^2
Stiffness parameter	m	3.0	–
Effective density of dense solid	ρ^{SR}	2.1×10^{-6}	kg/mm^3
Effective density of pore fluid	ρ^{FR}	1.0×10^{-6}	kg/mm^3
Darcy permeability	k^F	3.0×10^{-2}	mm/s
Initial volume fraction of solid	n^S_{0S}	0.1	–
Boundary and initial pore pressure	$\bar{p}^{FR}$	0.0	N/mm^2
Boundary and initial growth-energy value	$\bar{\mathcal{C}}^F$	2.11×10^{-1}	mJ/mm^3
Growth-energy diffusion coefficient	$D^{\mathcal{C}}$	6.0×10^{-1}	mm/s
Development rate coefficient of pre-osteoblasts	D^R	7.0×10^{-4}	pM/dm^3
Development rate coefficient of osteoblasts	D^B	3.5×10^{-3}	1/d
Development rate coefficient of osteocytes	D^Y	1.89×10^{-3}	1/d
Development rate coefficient of osteoclasts	D^C	2.1×10^{-4}	pM/d
Apoptosis rate coefficient of osteoblasts	A^B	1.701×10^{-1}	1/d
Apoptosis rate coefficient of osteocytes	A^Y	1.9×10^{-3}	1/d
Apoptosis rate coefficient of osteoclasts	A^C	7.0×10^{-1}	1/d
PGE_2 influence factor	c_p	1.5×10^{-3}	pM/d
Basal concentration of TGF-β	c^{TC}_{m0}	2.5×10^{-5}	pM
Dissociation coefficient of TGF-β	c^{TC}_{mS}	5.0×10^{-3}	pM
PGE_2 Production rate coefficient	k^ψ	1.0	mm^{2}d^2/N
Stress influence factor	k^σ	1.0	mm^2/N
Osteocyte influence factor	k^Y	1.0	1/pM
Dissociation coefficient of PGE_2	c^P_{mS}	1.0	pM
Dissociation coefficient of RANKL	c^{LB}_{mS}	5.036×10^{-4}	pM
Dissociation coefficient of OPG with RANKL	c^{OR}_{mS}	3.395×10^{-5}	pM
RANK concentration	c^{KB}_m	1.7183×10^{-4}	pM
Regenerative rate parameter	c^+	1.0×10^2	1/pM
Degenerative rate parameter	c^-	1.35×10^1	1/pM
Michaelis constant of regenerative process	K^+_M	1.0	mJ/mm^3
Michaelis constant of degenerative process	K^-_M	1.0×10^{-3}	–
Maximal solid volume fraction	$n^S_{tS\max}$	1.0	–
Basal metabolic growth-energy consumption	k_{basal}	1.0×10^{-6}	mJ/pMs
Additional growth-energy consumption	k_{grow}	8.0×10^{-7}	mJ/mm^3

The chemical part advances the motion of the growth energy. Precisely speaking, the mechanical problem is solved employing a standard porous-media model, which neither contains internal state variables nor a diffusion-reaction equation such as the growth-

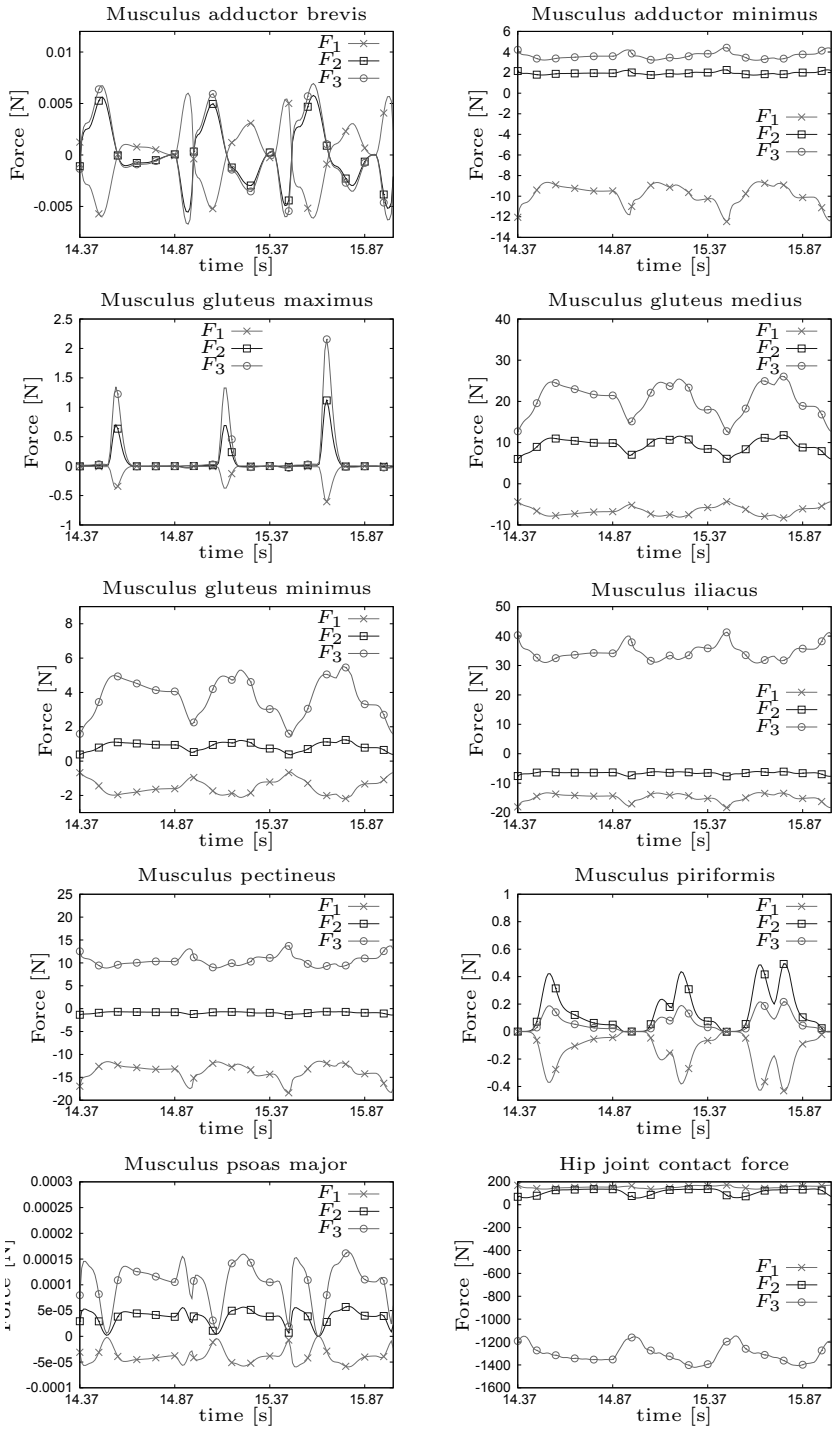

Figure 7.10.: Muscle and hip-joint contact forces of an upright standing person calculated by dynamic multi-body simulation (cf., e.g. Rupp *et al.*, 2011) of the whole muscular-skeletal system and transformed into the local bone coordinate system. Data obtained by courtesy of S. Schmitt.

Table 7.5.: Averages of the characteristic sequences depicted in Figure 7.10 used as static boundary conditions applied for the monolithic solution strategy.

Force [N]	$\mathbf{x}_1$	$\mathbf{x}_2$	$\mathbf{x}_3$
Musculus adductor brevis	0.0	0.0	0.0
Musculus adductor minimus	-9.823	1.944	3.619
Musculus gluteus maximus	-0.054	0.090	0.170
Musculus gluteus medius	-6.625	9.380	20.456
Musculus gluteus minimus	-1.521	0.864	3.761
Musculus iliacus	-14.866	-6.559	34.516
Musculus pectineus	-13.693	-0.884	10.480
Musculus piriformis	-0.140	0.157	0.075
Musculus psoas major	0.0	0.0	0.0
Hip joint contact force	153.453	113.005	-1304.33

Algorithm 3: Global block *Gauss-Seidel* method

Require: The mechanical, chemical and systems-biological simulations are started and the input parameters are loaded

repeat

  Import the new accompanying reference configuration at time T_N;

  for each $t \in (t_N, t_{N+1}]$ **do**

    Predict the solid and fluid motion by solving the mechanical subproblem;

    Transfer the results to the chemical simulation;

    Calculate the growth energy by **advancing** the chemical subproblem;

  end

  Transfer the required mechanical and chemical quantities to the systems–biological simulation;

  Calculate a new accompanying reference configuration at time T_{N+1} by solving the systems–biological subproblem;

until *the accompanying reference configuration converges to a steady state*;

energy balance. The chemical problem is solved using the same global system of equations as is used for the monolithic solution, however, the solid displacement and the pore-fluid pressure are obtained from the mechanical simulation and applied in the sense of *Dirichlet* boundary conditions on the whole domain. Hence, following the standard finite-element solution strategy (cf., e. g., Zienkiewicz & Taylor, 1989a), the rows and columns associated with displacement and pressure degrees of freedom are eliminated from the matrices of the overall equation system resulting in an equation system containing only the growth-energy balance. To control both simulations, the instance manager (subsection 6.2.3) of the chemical simulation is registered as observer at the callback web service of the mechanical simulation. Whenever a new result is available, the instance manager advises the chemical simulation to continue until it reaches the new time step. Thereby, it also in-

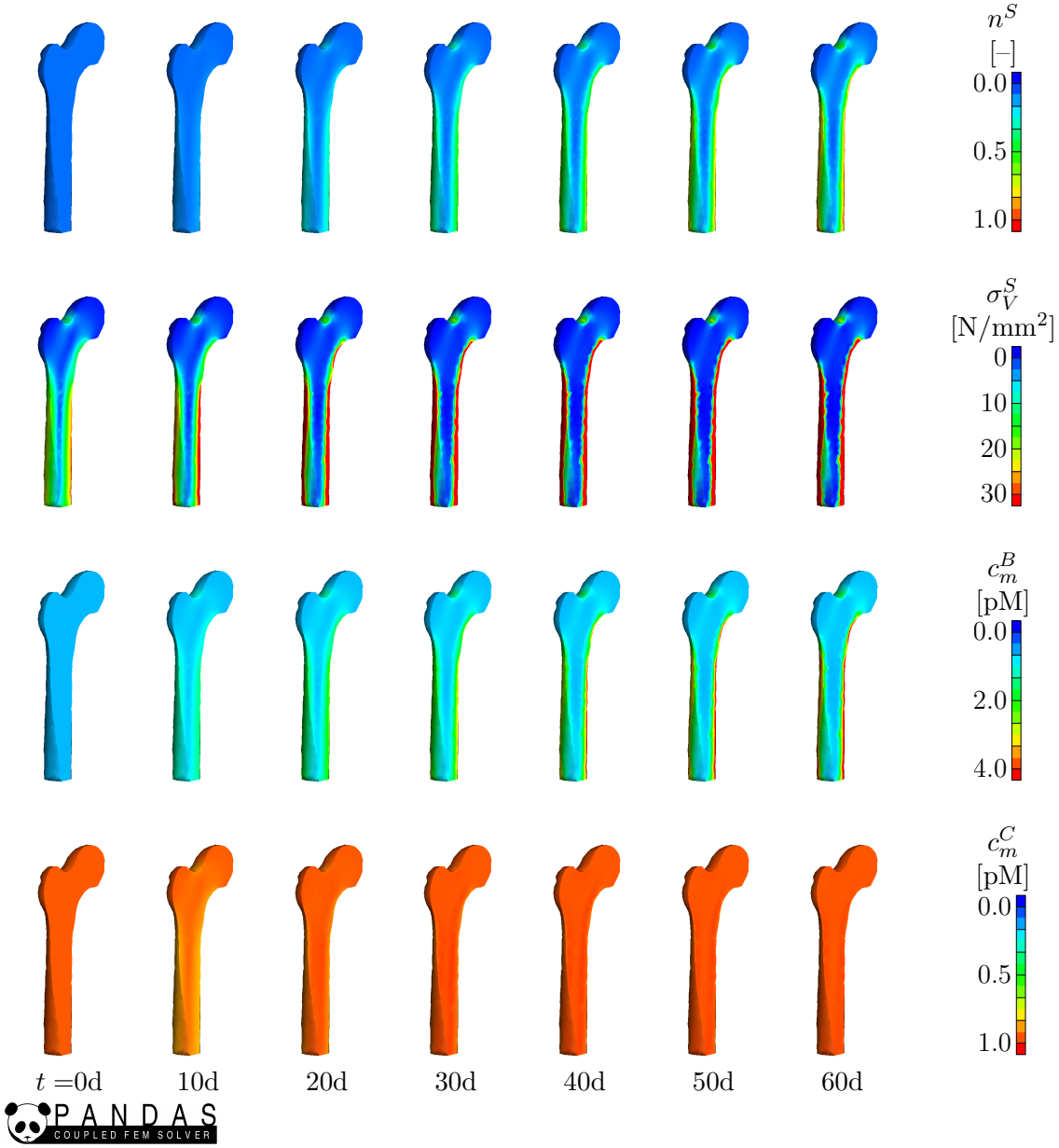

Figure 7.11.: 3-d simulation of remodelling in a human femur using a monolithic solution strategy. The colouring indicates the development of the solid volume fraction in a loaded femur starting from an initially homogeneous distribution ($n_{0S}^S = 0.1$).

terrupts the callback web service and so, the mechanical simulation until the chemical simulation is finished.

Using this staggered algorithm, the *von-Mises* stress σ_V^S and the growth energy $\mathcal{C}^F$ are calculated over an interval of 1 second using static boundary conditions and, the values at the integration points are stored in a database. The interval of 1 second is chosen to make a direct comparison with the monolithic solution possible. Keeping mechanical quantities constant, the cell-population dynamics and the changes of the accompanying reference

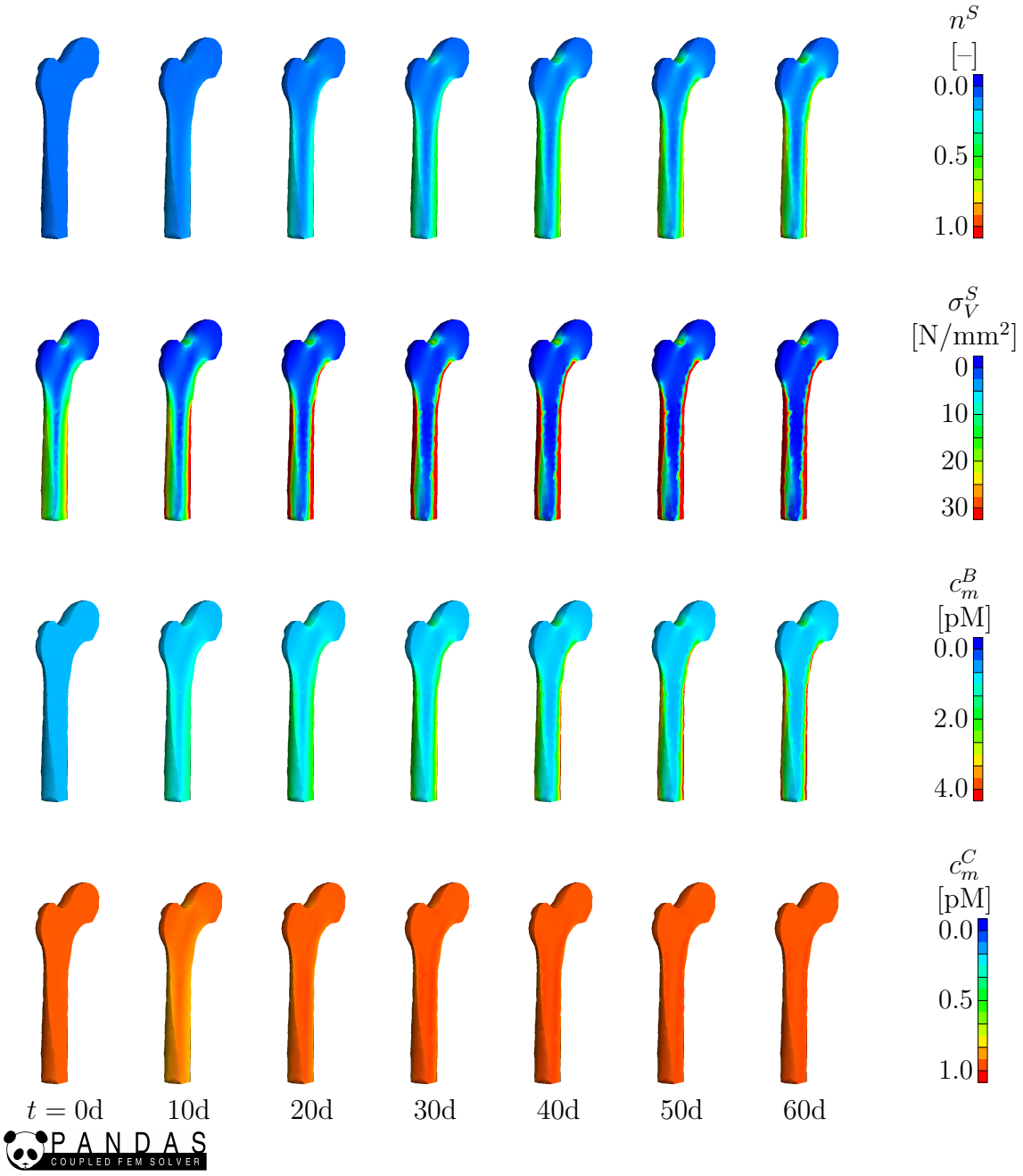

Figure 7.12.: 3-d simulation of remodelling in a human femur using a decoupled solution strategy with time interval $\Delta T = 1$d for the systems-biological submodel and static boundary conditions. The colouring indicates the development of the solid volume fraction in a loaded femur starting from an initially homogeneous distribution ($n_{0S}^S = 0.1$).

configuration during 1 day are calculated ($\Delta T = 1$d) using a time-step size of a half day for the temporal discretisation. Then, the new accompanying reference configuration is transferred to the mechanical and the chemical simulations and the whole algorithm is repeated.

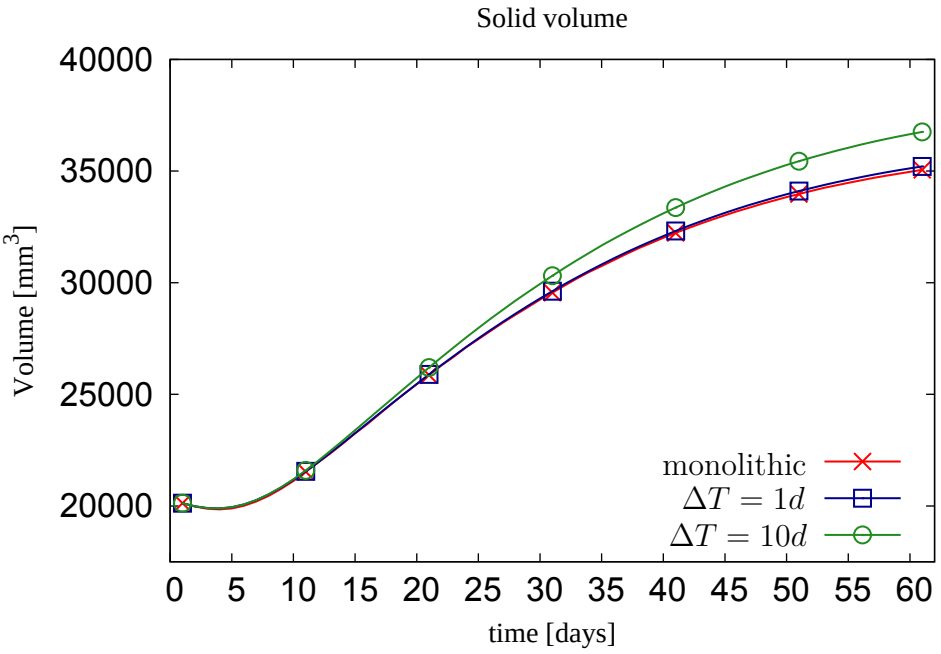

Figure 7.13.: Development of the overall solid volume $V^S = \int_\Omega n^S \mathrm{d}v$ in several simulations using a monolithic solution strategy and a decoupled solution strategy with different time-step sizes for the systems-biological subsystem ΔT. Qualitatively no difference can be found when compared.

The resulting developments of the solid volume fraction and the cell populations are depicted in Figure 7.12. Qualitatively, the results of the monolithic solution strategy are equivalent to the results obtained from the decoupled solution strategy. Also quantitatively, the increase of the solid volume during the decoupled solution coincides with the results obtained from the monolithic solution (Figure 7.13).

Moreover, with the decoupled solution scheme, the time intervals used for temporal discretisation of the mechanical subsystem Δt_n and time interval of the systems-biological subsystem ΔT_n can be chosen independent from each other. Choosing larger time intervals ΔT_n for the systems-biological simulation, tremendously reduces the time-consuming mechanical simulations. Exemplarily, the development of the solid volume fraction during a decoupled simulation using Algorithm 3 with a time interval of $\Delta t = 1$s for the mechanical subproblem and a time interval of $\Delta T = 10$d for the systems-biological subproblem is compared with the solution obtained by using a time interval of $\Delta T = 1$d in Figure 7.14. To calculate these results depicted the mechanical subproblem was solved 6 times, whereas to obtain the results depicted in Figure 7.12 the mechanical subproblem was solved 60 times. Qualitatively, both result are comparable with each other. However, in the latter simulation the systems-biological subproblem responds slower to changes of the variables obtained from the mechanical and chemical subproblem, and therefore, the quantitative difference becomes larger (Figure 7.13).

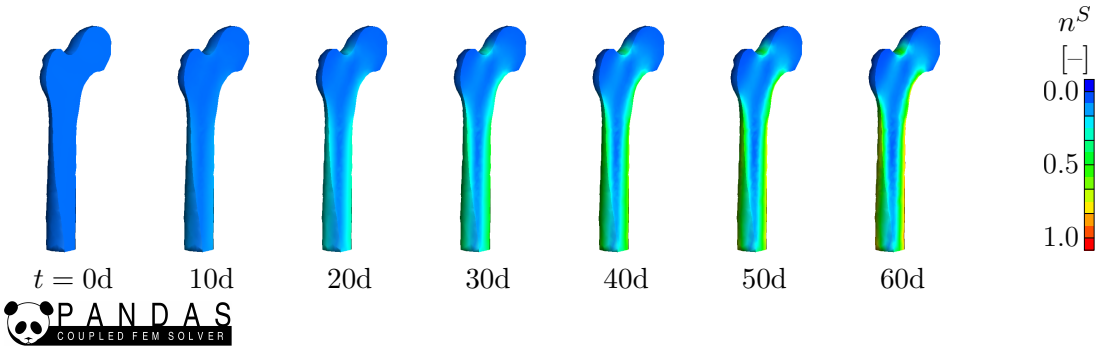

Figure 7.14.: 3-d simulation of remodelling in a human femur using a decoupled solution strategy with time interval $\Delta T = 10$d for the systems-biological submodel and static boundary conditions. The colouring indicates the development of the solid volume fraction in a loaded femur starting from an initially homogeneous distribution ($n^S_{0S} = 0.1$). Although a ten times larger time interval was chosen for the systems-biological subproblem, the results are qualitatively comparable to the results depicted in Figure 7.12

Transient loading conditions

Taking into account that the exact cellular mechanisms that sense the mechanical loads are still unknown (Mellon & Tanner, 2012), the service-oriented solution might also serve as a flexible platform for simulation and evaluation. By replacing the systems-biological submodel with a different model, it becomes possible to evaluate the micro-scale models in a 3-d domain. However, in several experiments, a remodelling response was observed only at an altering distribution of dynamic strain rather than at a continuous static strain (cf., e. g., Hert *et al.*, 1971; Lanyon & Rubin, 1984; Lisková & Hert, 1971; Rubin & Lanyon, 1984). Hence, using a cell-population model that correctly mimics the mechanotransduction and static loading conditions cannot result in a realistic bone-matrix distribution. Thus, at least transient loading conditions must be considered.

The decoupled solution scheme is not restricted to simulations with static boundary conditions. Slight modification of the overall workflow model (Algorithm 3) yields Algorithm 4, which enables remodelling simulations with transient loading conditions without changing the involved simulation programs. Following this, the whole loading cycle depicted in Figure 7.10 is applied on the mechanical submodel, and for each global time-step, the stress and growth-energy distribution during the whole cycle are calculated and stored in the database. At the end of the loading cycle, instead of transferring the results of the last time-step, the results of the whole cycle are aggregated and transferred to the systems-biological submodels. Here, the average of the *von-Mises* stress and the growth energy are used. They are calculated by the database without interaction with the simulation programs. With this approach, the additional information is completely included into the overall workflow model and the implementations of the subproblems are unaffected. However, note that it is a problem-specific challenge to find adequate aggregation functions for the mechanical variables, which preserve the necessary information, needed by the systems-biological equation system under consideration.

Algorithm 4: Global block Gauss-Seidel method for transient loads

Require: The mechanical, chemical and systems–biological simulations are started and the input parameters are loaded

repeat

  Import the new accompanying reference configuration at time T_N;

  for each $t \in$ *the current loading cycle* **do**

    Predict the solid and fluid motion by solving the mechanical subproblem;

    Transfer the results to the chemical simulation;

    Calculate the growth energy by **advancing** the chemical subproblem;

  end

  Aggregate *the relevant quantities by use of an adequate function*;

  Transfer the *aggregated* mechanical and chemical quantities to the systems–biological simulation;

  Calculate a new accompanying reference configuration at time T_{N+1} by solving the systems–biological subproblem;

until *the accompanying reference configuration has converged to a steady state*;

In Figure 7.18, the resulting development of the solid volume fraction and the cell population distribution are depicted. Thereby, a time interval of $\Delta T = 10\text{d}$ for the systems-biological simulation is used. Again, the results are qualitatively in good agreement with the results obtained using static boundary conditions. As well, the quantitative development of the solid volume fraction coincides with the results obtained using static boundary conditions (Figure 7.16). Thus, for the considered systems-biological set of equations it is sufficient to use the average of the equivalent tensile stress as aggregation function.

7.3.3. Absence of gravity

To test the sensitivity of the systems-biological cell-population model to changes of the mechanical conditions, the response under the absence of gravity is examined. This special boundary condition is especially of interest when the effects of extended spaceflights have to be examined. Under these conditions, where bones are only loaded by the internal muscle forces, an average bone loss of one to two percent of mass per month is reported (LeBlanc *et al.*, 2000).

Here, the boundary conditions presented in Figure 7.17, are again obtained from previous forward dynamic multi-body simulation of the whole muscular-skeletal system, where the whole system is in a free fall and no ground contact forces are applied. Choosing a time interval of $\Delta T = 10\text{d}$, the resulting development of the solid volume fraction and the cell population distribution depicted in Figure 7.18 are obtained. Clearly, the lower equivalent tensile stress σ_V^S reduces the active osteoblasts c_m^B, and hence, results in a decreased solid volume fraction n_{tS}^S (cf. Figure 7.19).

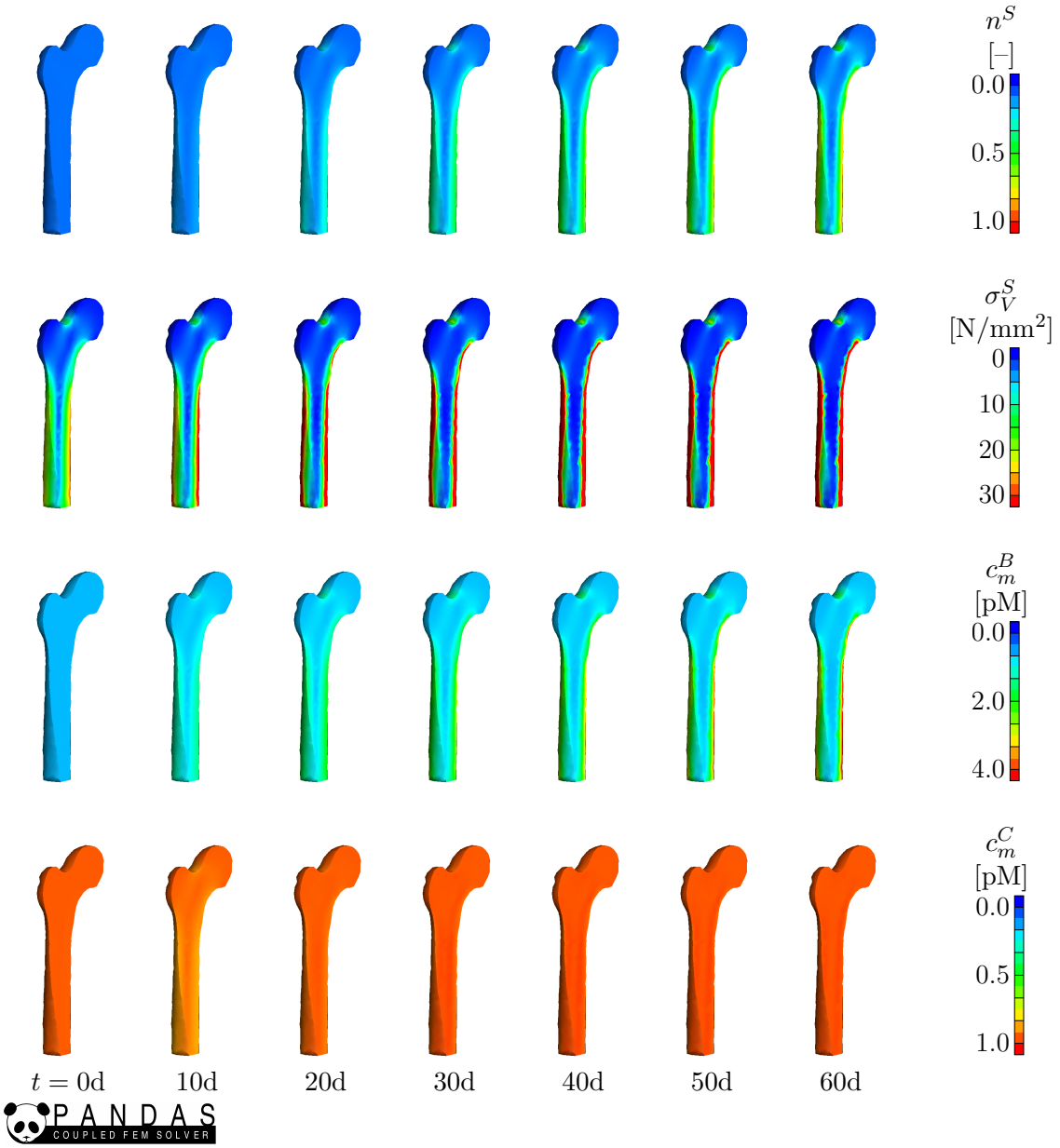

Figure 7.15.: 3-d simulation of remodelling in a human femur using a decoupled solution strategy with time interval $\Delta T = 10$d for the systems-biological submodel and transient boundary conditions. The colouring indicates the development of the solid volume fraction in a loaded femur starting from an initially homogeneous distribution ($n_{0S}^S = 0.1$). Due to the chosen systems-biological submodel the differences to the results obtained with static boundary conditions are rather small, cf. Figure 7.12 and Figure 7.14

7.3.4. Assembly of daily routines

The daily routine of healthy persons is an assembly of several activities that are sequentially joined together rather than a single activity. Morlock *et al.* (2001) report the daily activities of patients with a total hip replacement (arthoplasty), who spend the most time

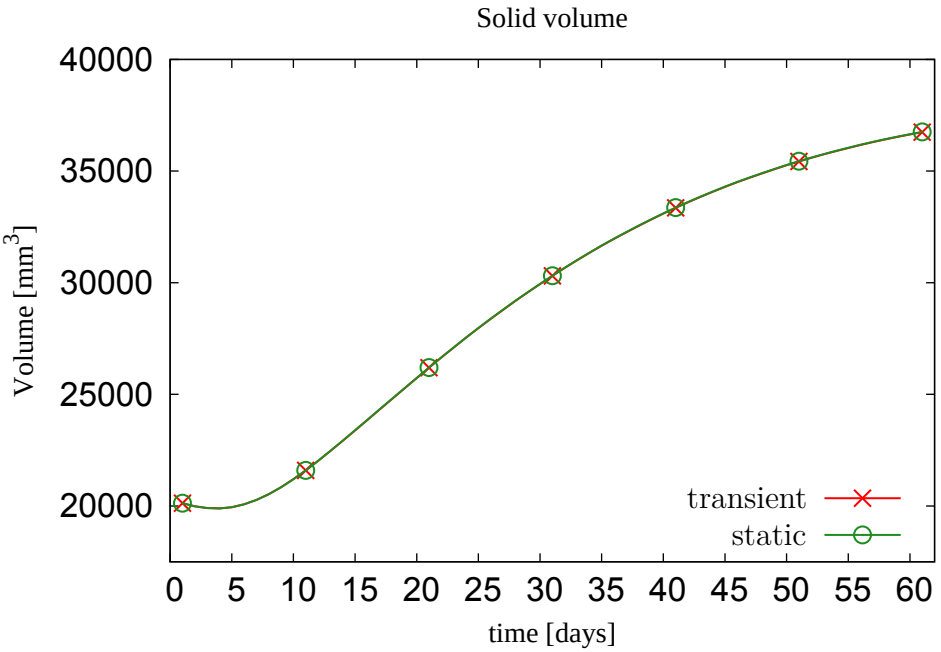

Figure 7.16.: Development of the overall solid volume $V^S = \int_\Omega n^S \mathrm{d}v$ in several simulations using a decoupled solution strategy with $\Delta T = 10\mathrm{d}$ and static and transient boundary conditions.

sitting (44.3%) followed by standing (14.5%), walking (10.2%), lying (5.8%) and stair climbing (0.4%). In this regard, the introduced decoupled solution strategy provides also the possibility to model a sequence of activities, where also small numbers of loading cycles can be included. Thereby, only the overall workflow model is adjusted, whereas the individual mechanical, chemical and systems-biological simulations remain unaffected. In Figure 7.20, a graphical illustration of the workflow model is depicted. Therein, employing the assumption of a slow remodelling process, using the same constant solid volume fraction ($n^S_{tS} = \text{const.}$), the characteristic loading cycles of several activities are calculated in parallel. Then, the course through the daily activities is assembled within the database, and the characteristic values are transferred to the systems-biological simulation, which updates the solid volume fraction n^S_{tS}. Again, the average function is used to aggregate the growth energy $\mathcal{C}^F$ and the equivalent tensile stress σ^S_V, before they are transferred to the systems-biological submodel. The resulting solid volume fraction is depicted in Figure 7.21. Alternatively, the remodelling can be calculated strictly following the daily course. The simulation results depicted in Figure 7.22 are obtained by alternating the used equivalent tensile stress. In particular, for an interval of a half day the average of the equivalent tensile stress obtained from the mechanical simulation of an upright standing person is applied, and then for the next interval of a half day the the equivalent tensile stress determined at the absence of gravity is applied. As expected, the overall solid volume lies between the volume fractions related to the genuine loading cases, standing and absence of gravity (Figure 7.23). As can be seen, the results obtained using altern-

ating equivalent tensile stresses coincides with the result obtained by using the average equivalent tensile stresses.

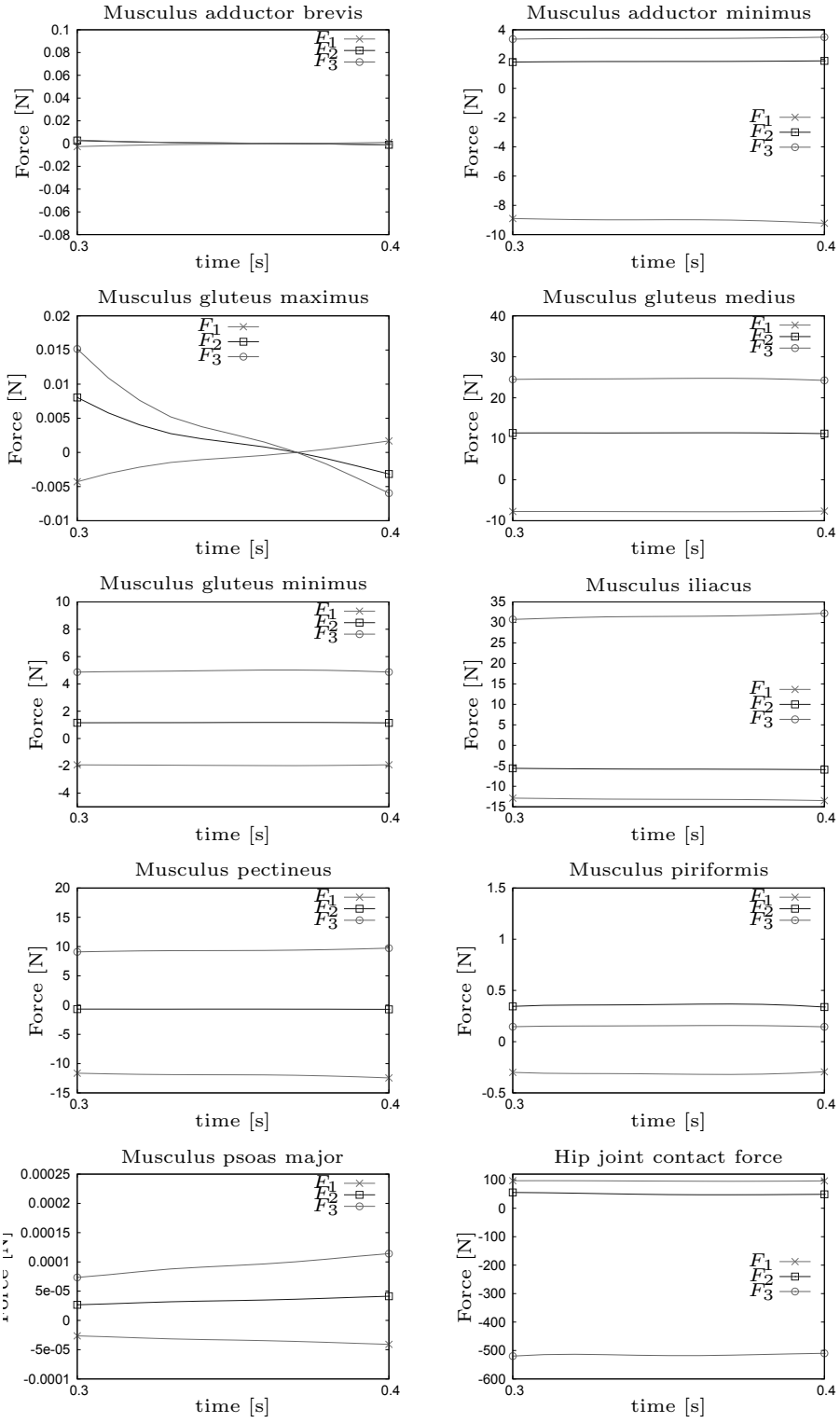

Figure 7.17.: Muscle and hip-joint contact forces at the absence of gravity calculated by a forward dynamic multi-body simulation of the whole muscular-skeletal system and transformed into the local bone coordinate system.

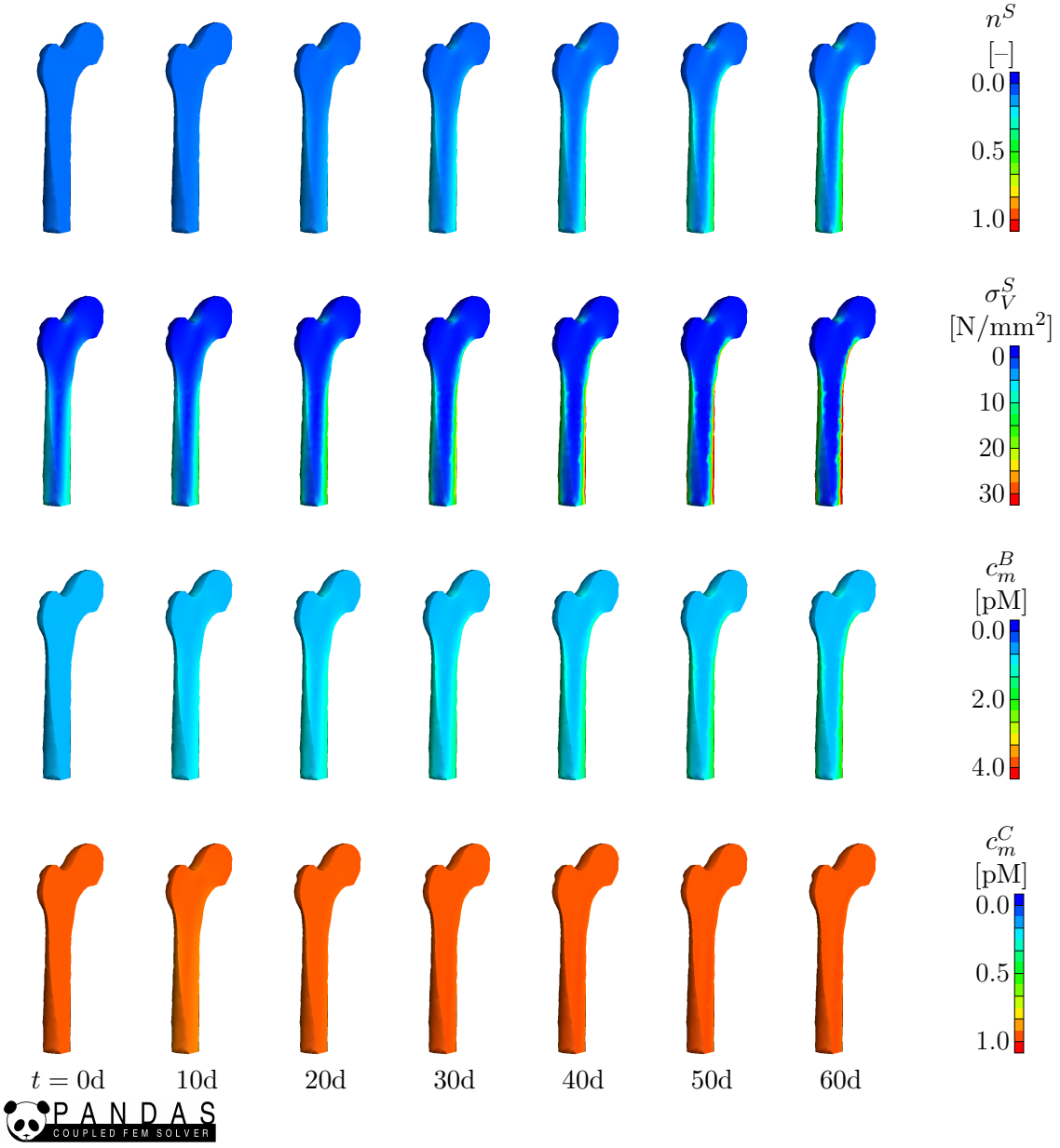

Figure 7.18.: 3-d simulation of remodelling in a human femur at the absence of gravity. The colouring indicates the development of the solid volume fraction in a loaded femur starting from an initially homogeneous distribution ($n_{0S}^S = 0.1$).

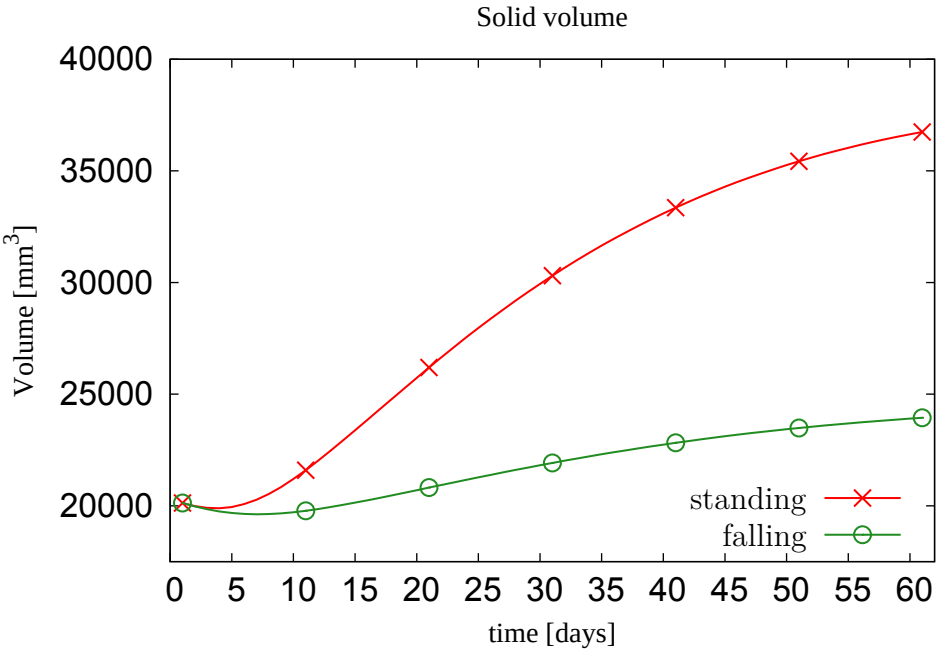

Figure 7.19.: Development of the overall solid volume $V^S = \int_\Omega n^S \mathrm{d}v$ at zero gravity conditions compared with the development at standing boundary conditions.

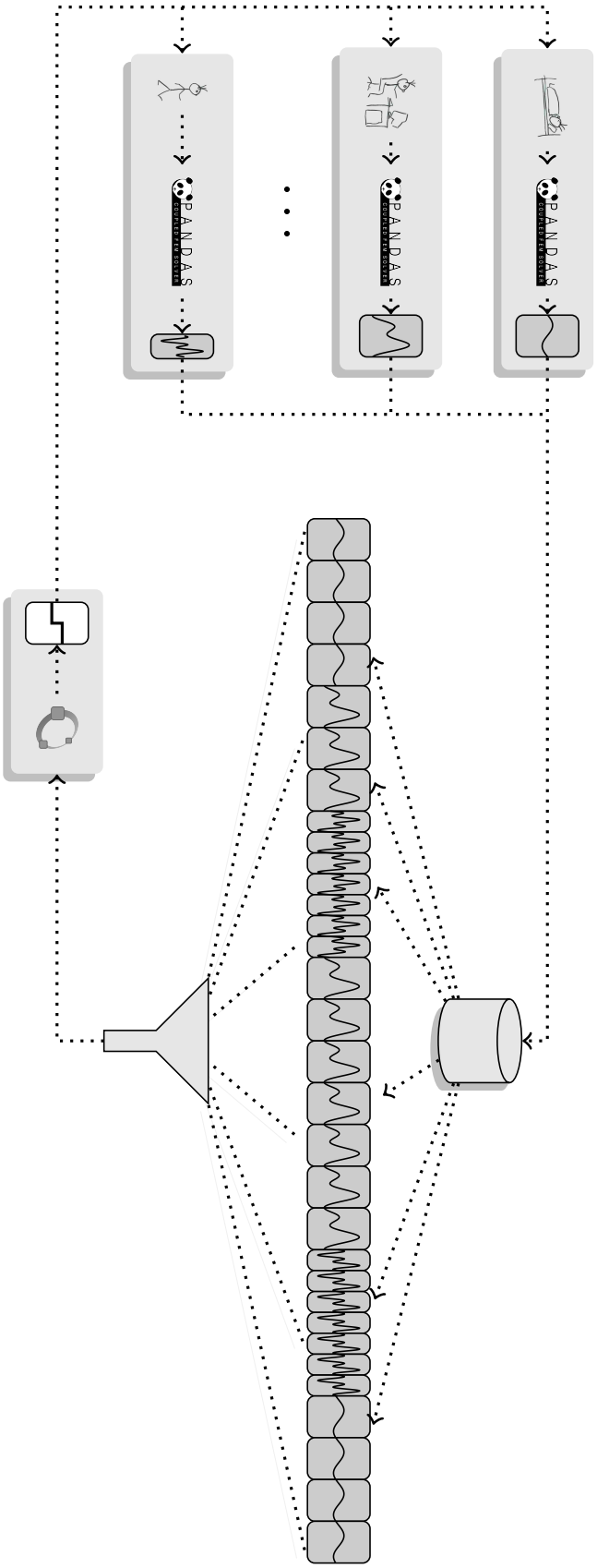

Figure 7.20.: Assembly of daily routines. Illustration of the workflow model including the data flow among the simulation instances.

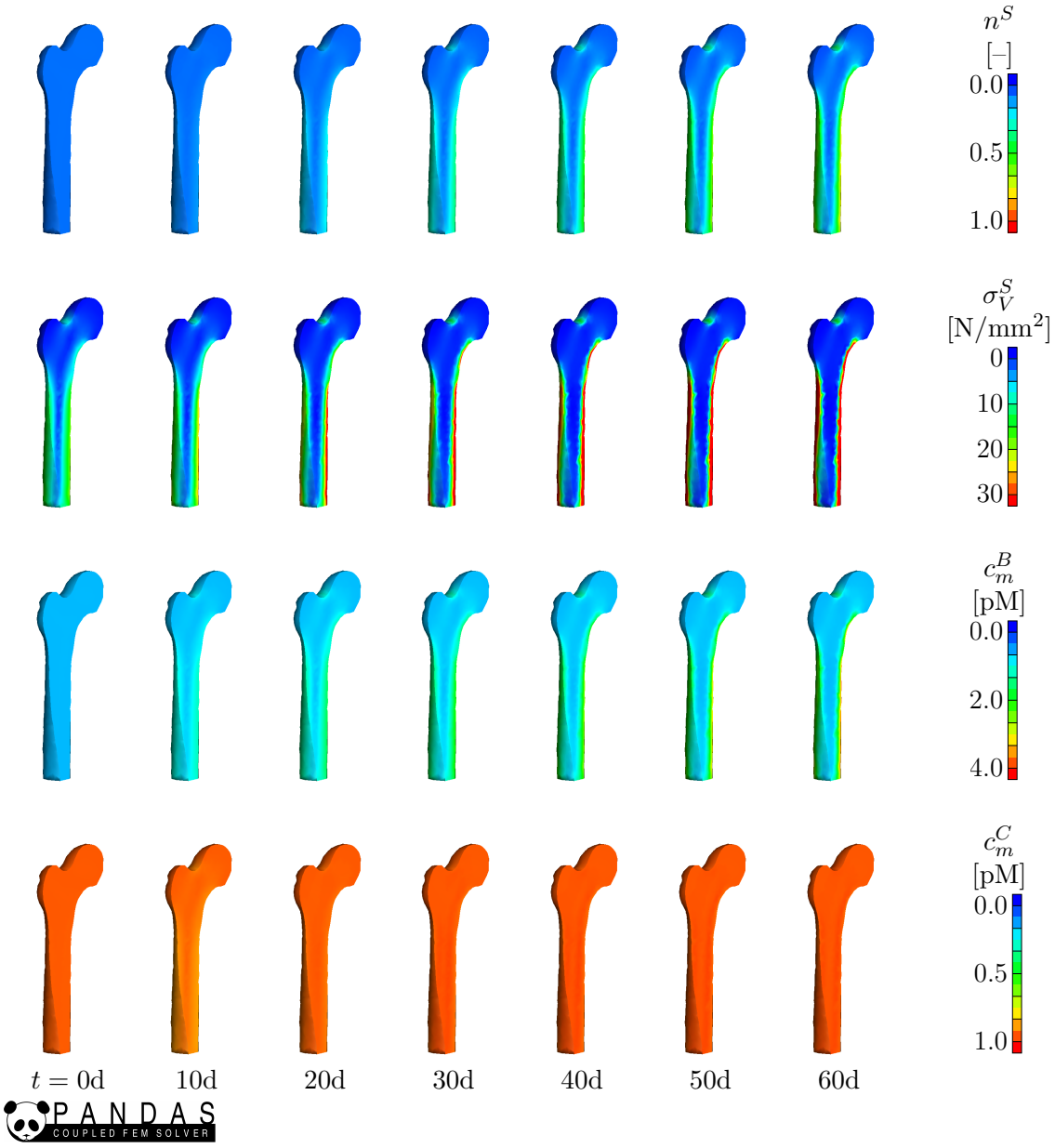

Figure 7.21.: 3-d simulation of remodelling in a human femur using the average equivalent tensile stress of the loading conditions absence of gravity and standing to calculate the remodelling. The colouring indicates the development of the solid volume fraction in a loaded femur starting from an initially homogeneous distribution ($n_{0S}^S = 0.1$).

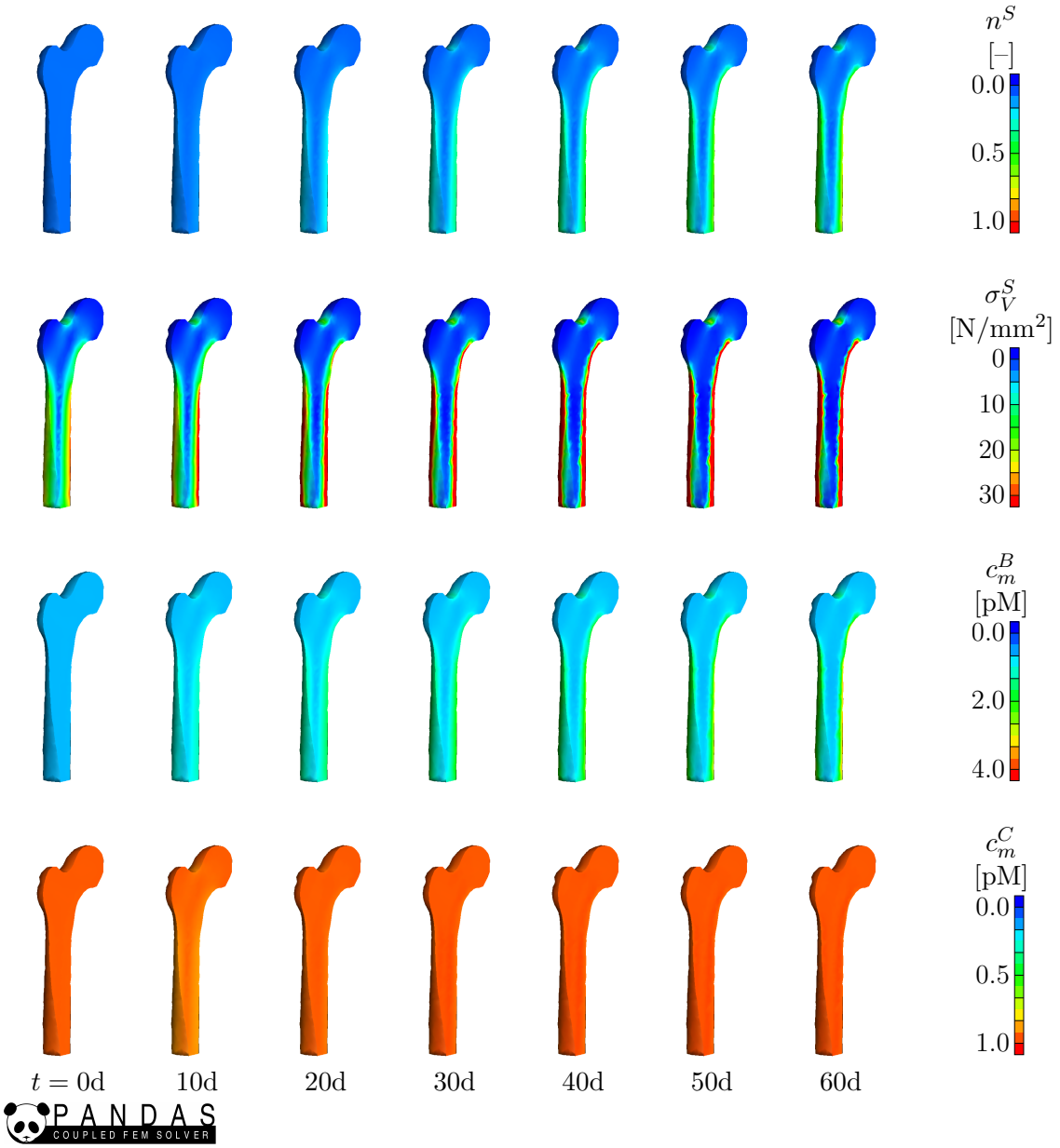

Figure 7.22.: 3-d simulation of remodelling in a human femur using the average equivalent tensile stress at the absence of gravity and average equivalent tensile stress at standing alternating to calculate the remodelling. The colouring indicates the development of the solid volume fraction in a loaded femur starting from an initially homogeneous distribution ($n_{0S}^S = 0.1$). The differences with the results depicted in Figure 7.22 are marginal.

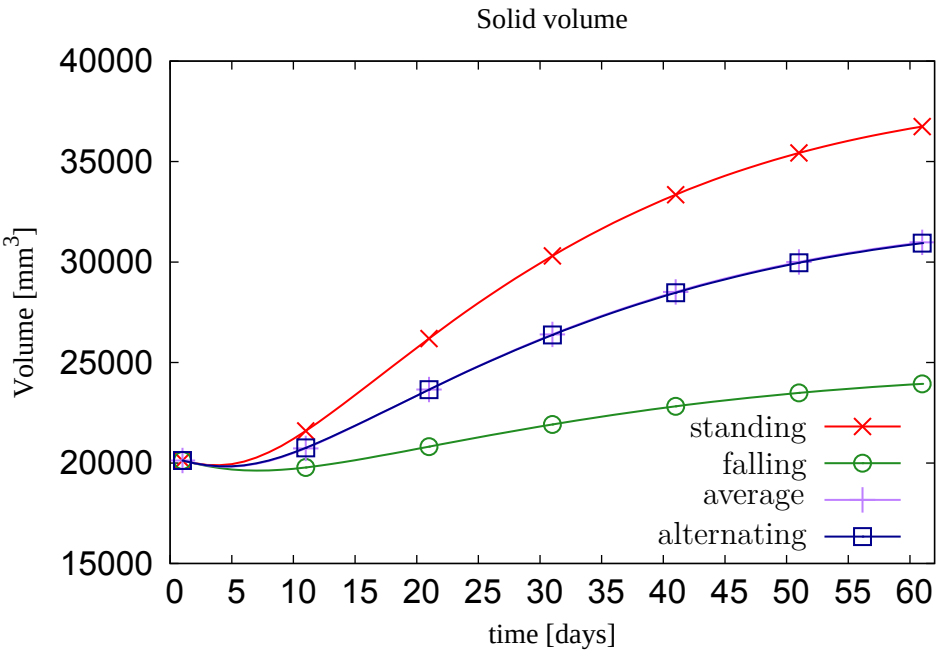

Figure 7.23.: Development of the overall solid volume $V^S = \int_\Omega n^S \mathrm{d}v$ calculated from a daily routine consisting of 50% zero gravity conditions and 50% standing boundary conditions compared with the development at the genuine loading cases.

Chapter 8: Outlook and Future Work

Here, the complex behaviour of biological tissue is described on the tissue scale by employing the Theory of Porous Media. Growth and remodelling processes are included into the model by assuming a distinct mass exchange between the fluid and the solid phase, which results in changes of the solid volume fraction of the accompanying reference configuration.

To identify thermodynamically consistent material laws for the growth and remodelling processes, it becomes necessary to consider biological and chemical mechanisms. These processes are incorporated by employing the growth energy as a measure of the chemical energy available for cell metabolism. As a result, it gets obvious that for a thermodynamically consistent description of the growth and remodelling mechanisms, the consumption of metabolic energy by the cells must be considered. Thus, the solid volume production is split into a degenerative and a regenerative part, which are evaluated individually. This leads to separate restrictions for both parts, where the regenerative part is restricted by the growth energy, which must be above a certain threshold value.

To demonstrate the applicability and to clarify the necessity of this approach, the growth-energy concept was applied to the early stages of avascular tumour growth and bone remodelling, where 3-d initial-boundary-value problems were numerically solved using the mixed finite-element method. For the description of tumour growth, the growth energy acts as the major trigger of the growth process itself. Concerning the remodelling of bones, the growth-energy concept is a plausible extension of the existing models. It is necessary for thermodynamic considerations and allows the inclusion of further metabolic effects into the model, e. g., the impact of a permanent malnutrition.

Furthermore, this concept provides the basis for the inclusion of regulation mechanisms that occur on the cellular level. These mechanisms are investigated by the discipline of Systems Biology, which uses specific methods and numerical tools. Modern computational solution strategies like the web-service technology and Scientific Workflows provide an excellent framework for the incorporation of continuum-mechanical and systems-biological tools towards an integrated growth and remodelling model. Thereby, the mechanical model is employed to calculate the relevant mechanical quantities and the systems-biological model focusses on the local remodelling processes. The numerical treatment using workflow and web-service technology is introduced and compared with a traditional implementation strategy. Thereby, the web-service technology allows for the usage of tailored programs for the solution of each subproblem, where the workflow controls the data and control flow among the services. This allows each scientist to concentrate on a specific subproblem and to develop a domain-specific solution strategy, which can be readily incorporated into the overall workflow.

To demonstrate the capability of the service-oriented solution strategy, the remodelling under different transient boundary conditions obtained from a previous multi-body simulation of the overall muscular-skeletal system is calculated. A preliminary simulation, using static boundary conditions, and the results of the monolithic and decoupled solu-

tion strategies are qualitatively and quantitatively in very could agreement. Using the decoupled solution strategy, the interval size used for the systems-biological subproblem influences the result quality and the computational effort. Choosing a larger interval reduces the computational effort and the accuracy of the results. The latter is mostly caused by a delayed response to changes of the variables calculated in the mechanical and chemical subproblem. Then, instead of using static boundary conditions, remodelling caused by transient boundary conditions is calculated. Therefore, a sequence of boundary conditions is applied, and the average of the resulting stress distribution is transferred to the systems-biological subproblem. Again, the results are qualitatively and quantitatively in very good agreement with the results obtained from simulations with static boundary conditions.

By changing the overall workflow model, it becomes possible to simulate multiple loading scenarios in parallel and to assemble the daily routine within the database. Therewith, the remodelling caused by a sequence of activities can be calculated from the assembled data set (subsection 7.3.4), which has high clinical relevance. A simulation considering multiple loading situations helps to qualitatively predict the surgery outcome with different prosthesis types. Thereby, the integration of cell-population dynamics provides an accurate way of simulating and interpreting the influence of mechanical loads on the bone structure, and allows for considering the effects of medicaments, hormones or diseases. This approach provides the possibility to numerically predict the individual patient risk to suffer a periprosthetic joint infection after a total hip replacement, where a slower cellular response increases the probability of bacterial infections on the surface of the endoprosthesis. This is one of the most challenging complications of total joint arthroplasty. Furthermore, the accurate prediction of the bone loss during extended spaceflights becomes possible, where a combination of exercises and a special dietary attenuates the bone loss.

Beyond the clinical relevance, the integration of simulations into the business processes, as discussed in Section 6.2 and demonstrated in Section 7.3, will become more important in industrial applications. For example, Cyber Physical Production Processes allow for the manufacturing of individual products for each client. To guarantee that every product fulfils legal and normative restrictions, simulations before and during its production are indispensable.

The solution strategy presented in subsection 7.3.4 has not only clinical relevance, but also provides a suitable method for construction and dimensioning in structural engineering following the technical rules provided by the Eurocodes, where the huge number of load combinations prevent an a-priori identification of the relevant loading scenario, and requires the parallel calculation and combination of several loading cases.

Last but not least, in scientific research, the possibility to easily exchange one submodel, enables a simple numerical validation and verification of the multiple hypothesis on the remodelling stimuli within bones by comparing the results of different remodelling algorithms. In this context, splitting of the global equation system into mechanical and chemical parts, as introduced in subsection 6.2.1, allows for the consideration of multiple fluid components, where the diffusion of every component is calculated by an individual simulation. Hence, the number of considered solutes is only limited by the available hard-

ware structure and can be adapted to the requirements of the systems-biological submodel. Nevertheless, here only uncharged molecules are included. The inclusion of charged ions might lead to swelling of the solid constituent, which requires a special treatment.

To investigate the effect of tumour cells on a whole organ, the example demonstrated in Section 7.1 should be extended, such that the consideration of the surrounding healthy tissue becomes possible. Therefore, the solid phase must be split into a healthy and a tumorous part, where the latter contributes to the positive solid-mass production. Furthermore, to include the influence of hormones and therapeutic agents on the cell populations, a systems-biological model that includes this aspects should be considered.

Concerning the growth energy, the numerical concept introduced in subsection 6.2.1 provide an alternative solution strategy. By using modern simulation techniques, it becomes possible to calculated the distribution of multiple solutes in parallel. Thus, it is in principle possible to consider an unlimited number of solutes, and therefore, future research should identify and consider the relevant solutes, rather than abstracting all solutes within one quantity.

Appendix A: Mathematical relations

It is possible to calculate the solid volume fraction n^S by an analytical integration of the solid volume balance

$$(n^S)'_S + n^S \operatorname{div} \mathbf{v}_S = \hat{n}^S \,. \tag{A.1}$$

The divergence term is replaced by the determinant of the deformation gradient and its derivative:

$$\operatorname{div} \mathbf{v}_\alpha = \frac{(\det \mathbf{F}_\alpha)'_\alpha}{\det \mathbf{F}_\alpha} \,, \tag{A.2}$$

which yields the form

$$\frac{(n^S)'_S}{n^S} + \frac{(\det \mathbf{F}_S)'_S}{\det \mathbf{F}_S} = \frac{\hat{n}^S}{n^S} \,. \tag{A.3}$$

Recalling the definition of the time derivatives in this equation

$$(n^S)'_S = \frac{\mathrm{d}_S n^S}{\mathrm{d}t} \quad \text{and} \quad (\det \mathbf{F}_S)'_S = \frac{\mathrm{d}_S \det \mathbf{F}_S}{\mathrm{d}t} \,, \tag{A.4}$$

the solid volume balance after separation of variables and after analytical integration reads:

$$\int \frac{1}{n^S} \mathrm{d}n^S + \int \frac{1}{\det \mathbf{F}_S} \mathrm{d}(\det \mathbf{F}_S) = \int_0^t \frac{\hat{n}^S}{n^S} \mathrm{d}t \,. \tag{A.5}$$

With the integration relation

$$\ln x - \ln y(0) = \int_0^x \frac{1}{y} \mathrm{d}y \,, \tag{A.6}$$

where $\ln y(0)$ is the integration constant which can be calculated from the initial value, the solid volume fraction reads:

$$\ln n^S - \ln n^S_{0S} + \ln \det \mathbf{F}_S - \ln \det \mathbf{I} = \int_0^t \frac{\hat{n}^S}{n^S} \mathrm{d}t \,. \tag{A.7}$$

Therein, n^S_{0S} is the initial volume fraction, and the initial deformation gradient is equal to the identity tensor $\mathbf{I}$. After exponentiation and transformation, the final form is found:

$$n^S = n^S_{0S} \, \exp\Big(\int_{t_0}^t \frac{\hat{n}^S}{n^S} \mathrm{d}t \Big) (\det \mathbf{F}_S)^{-1} \,, \tag{A.8}$$

where the solid volume fraction of the accompanying reference configuration can be identified as

$$n^S_{tS} = n^S_{0S} \, \exp\Big(\int_{t_0}^t \frac{\hat{n}^S}{n^S} \mathrm{d}t \Big) \,. \tag{A.9}$$

To calculate the time derivative of n_{tS}^S, the exponent in (A.9) is substituted by $g(t)$

$$g(t) = \int_{t_0}^{t} \frac{\hat{n}^S}{n^S} \mathrm{d}t \quad \text{with} \quad \frac{\mathrm{d}g}{\mathrm{d}t} = \frac{\hat{n}^S}{n^S} \,. \tag{A.10}$$

Employing the chain rule, the time derivative reads:

$$(n_{tS}^S)'_S = \underbrace{n_{0S}^S \exp(g(t))}_{\frac{\partial n_{tS}^S}{\partial g}} \underbrace{\frac{\hat{n}^S}{n^S}}_{\frac{\partial g}{\partial t}} \,. \tag{A.11}$$

Inserting the solid volume fraction, the final form is found

$$(n_{tS}^S)'_S = \frac{n_{0S}^S \exp(g(t)) \hat{n}^S}{n_{0S}^S \exp(g(t)) (\det \mathbf{F}_S)^{-1}} = \hat{n}^S \det \mathbf{F}_S =: \hat{n}_{tS}^S \,. \tag{A.12}$$

Appendix B: Entropy inequality

For the evaluation of the entropy principle, the dependencies of the *Helmholtz* free energies must be included. The solid *Helmholtz* free energy ψ^S is assumed to be a function of the solid deformation gradient $\mathbf{F}_S$ and, additionally, of the solid volume fraction n^S to account for the volume production governing the growth process. Furthermore, the *Helmholtz* free energies of the mixture components Ψ_F^β are functions of the partial pore density ρ_F^β of the respective component. Hence, the dependencies of the *Helmholtz* free energies read:

$$\psi^S := \psi^S(\mathbf{F}_S, n^S) \quad \text{and} \quad \Psi_F^F := \Psi_F^F(\cup_\gamma \rho_F^\gamma) = \Psi_F^L + \sum_\gamma \Psi_F^\gamma(\rho_F^\gamma). \tag{B.1}$$

For a detailed derivation of the dependencies of the *Helmholtz* free energy, refer to Ehlers (2002, 2009) and the references therein. The time derivatives of the Helmholtz free energies used in the entropy inequality (4.14) are calculated by use of the chain rule:

$$\begin{aligned} \rho^S(\psi^S)'_S &= \rho^S \frac{\partial \psi^S}{\partial \mathbf{F}_S} \mathbf{F}_S^T \cdot \mathbf{L}_S + \rho^S \frac{\partial \psi^S}{\partial n^S}(n^S)'_S \,, \\ n^F(\Psi_F^F)'_F &= n^F \sum_\gamma \frac{\partial \Psi_F^F}{\partial \rho_F^\gamma}(\rho_F^\gamma)'_F \,. \end{aligned} \tag{B.2}$$

Furthermore, the mass and volume balances (4.10) and (4.3) together with (3.10) are used to reformulate the local time derivatives $(n^S)'_S$ and $(\rho_F^\gamma)'_F$:

$$\begin{aligned} (n^S)'_S &= -\, n^S \operatorname{div} \mathbf{v}_S + \hat{n}^S = -n^S \mathbf{L}_S \cdot \mathbf{I} + \hat{n}^S \,, \\ n^F(\rho_F^\beta)'_F &= -\, n^F \rho_F^\beta \mathbf{L}_\beta \cdot \mathbf{I} - n^S \rho_F^\beta \mathbf{L}_S \cdot \mathbf{I} + n^F \hat{\rho}_F^\beta + \hat{n}^S \rho_F^\beta - \\ &\quad - \rho_F^\beta \operatorname{grad} n^F \cdot \mathbf{w}_\beta - n^F \operatorname{grad} \rho_F^\beta \cdot \mathbf{d}_{\beta F} \,. \end{aligned} \tag{B.3}$$

The latter is obtained by reformulating (4.10):

$$\begin{aligned} n^F(\rho_F^\beta)'_F &= -\, n^F \rho_F^\beta \operatorname{div} \mathbf{v}_\beta + n^F \hat{\rho}_F^\beta - n^F \operatorname{grad} \rho_F^\beta \cdot \mathbf{d}_{\beta F} - \rho_F^\beta (n^F)'_\beta \\ &= -\, n^F \rho_F^\beta \operatorname{div} \mathbf{v}_\beta - n^S \rho_F^\beta \operatorname{div} \mathbf{v}_S + n^F \hat{\rho}_F^\beta + \hat{n}^S \rho_F^\beta - \\ &\quad - \rho_F^\beta \operatorname{grad} n^F \cdot \mathbf{w}_\beta - n^F \operatorname{grad} \rho_F^\beta \cdot \mathbf{d}_{\beta F} \,, \end{aligned} \tag{B.4}$$

where the derivative of the fluid volume fraction is reformulated using relation (3.10) and the saturation constraint (4.15):

$$(n^F)'_\beta = (n^F)'_S + \operatorname{grad} n^F \cdot \mathbf{w}_\beta = -(n^S)'_S + \operatorname{grad} n^F \cdot \mathbf{w}_\beta \,. \tag{B.5}$$

Concerning the solvent φ^L, after inserting (4.1) and (4.2) in $(\text{B.3})_2$, the saturation constraint (4.15) reads:

$$n^F(\rho_F^L)'_F = -n^F \rho^{FR} \mathbf{L}_F \cdot \mathbf{I} - n^S \rho^{FR} \mathbf{L}_S \cdot \mathbf{I} + \hat{n}^F \rho^{FR} + \hat{n}^S \rho^{FR} - \rho^{FR} \operatorname{grad} n^F \cdot \mathbf{w}_F = 0 \,. \tag{B.6}$$

With these results, the entropy inequality (4.19) yields

$$
\begin{aligned}
&\Big[\mathbf{T}^S + n^S\mathcal{P}\mathbf{I} - \rho^S\frac{\partial\,\psi^S}{\partial\mathbf{F}_S}\,\mathbf{F}_S^T + \rho^{SR}(n^S)^2\frac{\partial\,\psi^S}{\partial n^S}\,\mathbf{I} - \\
&-n^S\Psi_F^F\mathbf{I} + n^S\sum_\gamma \rho_F^\gamma\frac{\partial\,\Psi_F^F}{\partial\rho_F^\gamma}\,\mathbf{I}\Big]\cdot\mathbf{L}_S + \\
&+\Big[\mathbf{T}^L + n^F\mathcal{P}\mathbf{I} - n^F\Psi_F^L\mathbf{I} + n^F\rho_F^L\frac{\partial\,\Psi_F^F}{\partial\rho_F^L}\,\mathbf{I}\Big]\cdot\mathbf{L}_F + \\
&+\sum_\gamma\Big[\mathbf{T}^\gamma - n^F\Psi_F^\gamma\,\mathbf{I} + n^F\rho_F^\gamma\frac{\partial\,\Psi_F^F}{\partial\rho_F^\gamma}\,\mathbf{I}\Big]\cdot\mathbf{L}_\gamma - \\
&-\Big[\hat{\mathbf{p}}^F - \mathcal{P}\,\mathrm{grad}\,n^F + \Big(\Psi_F^F - \sum_\gamma\rho_F^\gamma\frac{\partial\,\Psi_F^F}{\partial\rho_F^\gamma}\Big)\,\mathrm{grad}\,n^F\Big]\cdot\mathbf{w}_F - \\
&-\sum_\gamma\Big[\hat{\mathbf{p}}^\gamma + \Big(\Psi_F^\gamma - \rho_F^\gamma\frac{\partial\,\Psi_F^F}{\partial\rho_F^\gamma}\Big)\,\mathrm{grad}\,n^F + n^F\,\mathrm{grad}\,\Psi_F^\gamma - \\
&-n^F\frac{\partial\,\Psi_F^F}{\partial\rho_F^\gamma}\,\mathrm{grad}\,\rho_F^\gamma\Big]\cdot\mathbf{d}_{\gamma F} + \\
&+\hat{n}^F\rho^{FR}\Big[\psi^S - \frac{\Psi_F^L}{\rho^{SR}} + \frac{\Psi_F^L}{\rho^{FR}} + \sum_\gamma\Big(\frac{\rho_F^\gamma}{\rho^{SR}}\frac{\partial\,\Psi_F^F}{\partial\rho_F^\gamma} - \frac{\Psi_F^\gamma}{\rho^{SR}}\Big) - \tfrac{1}{2}\mathbf{w}_F\cdot\mathbf{w}_F + \\
&+\frac{\rho^{FR}-\rho^{SR}}{\rho^{FR}\rho^{SR}}\Big(\mathcal{P} + \rho^{FR}\frac{\partial\,\Psi_F^F}{\partial\rho_F^L}\Big) + \frac{1}{\rho^{SR}}\frac{\partial\,\psi^S}{\partial n^S}\Big] - \\
&-\sum_\gamma n^F\frac{\hat{\rho}_F^\gamma}{\rho_F^\gamma}\Big[\rho_F^\gamma\frac{\partial\,\Psi_F^F}{\partial\rho_F^\gamma} - \rho_F^\gamma\mathbf{v}_\gamma\cdot\mathbf{v}_S + \tfrac{1}{2}\rho_F^\gamma\mathbf{v}_\gamma\cdot\mathbf{v}_\gamma\Big] \geq 0\,.
\end{aligned}
\tag{B.7}
$$

Evaluation of this inequality leads to restrictions that must be fulfilled by thermodynamically consistent processes. The inequality as a whole is sufficiently fulfilled if each single term of the inequality fulfils the inequality itself, which is the standard evaluation procedure as described by Coleman & Noll (1963).

Appendix C: Implementation details

Executing a legacy application as a web service with tight binding to calling instance, makes it necessary to provide information on the internal state of the application through the external web-service interface. This can be done by submitting all changes of the internal state variables to the web-service wrapper. The observable template class, which is part of the PANDAS callback stub provides such an interface.

C.1. Observable template class

The observable template class provides an abstract interface for variables and parameters that are monitored by the web-service wrapper. It is designed such that an existing variable can be declared as observable with minimal changes of the source code. More precisely, for using the observable template class only the definition of the variable must be changed, where the variable type is used as template parameter C.

Thereby, the private member function `reportChange()`, which is called whenever the value of the observable is changed, notifies the web-service wrapper. In detail, a SOAP message containing simulation ID, the variable name, the new value and the type of the variable is sent to the web-service wrapper:

```
<?xml version="1.0"?>
<soap:Envelope xmlns:soap="http://www.w3.org/2003/05/soap-envelope">
    <soap:Body>
        <sc:SimulationCallback xmlns:soap="http://get-pandas.com/sc">
            <sc:reportVariableChange>
                <sc:simID>42</sc:simID>
                <sc:VariableName>time</sc:VariableName>
                <sc:VariableType>double</sc:VariableType>
                <sc:VariableValue>43.5</sc:VariableValue>
            </sc:reportVariableChange>
        </sc:SimulationCallback>
    </soap:Body>
</soap:Envelope>
```

C.1.1. Member variables

Beside the value of the observed variable, also its name must be stored. The variable name used in the source code cannot be determined at runtime from the executable, since it is replaced during compilation. Instead, the variable name must be stored as an additional constant member variable.

```
///@file observable.h

template <class C> class Observable{
```

```
4 private:
5         C value;
6         const std::string name;
```

Therein, following Stroustrup (2000), the constant modifier is required to allow further optimisations by the compiler and linker.

C.1.2. Member functions

To assure that using the observable class instead of the original class requires no changes of the source code, implicit conversion between the observable class and the observable type must be provided by member functions. In particular, an assignment operator as well as conversion operators are implemented.

Constructors

To construct an observable, at least its name and type must be provided. Thereby, the variable type is used to instantiate the template. In addition, an initial value can be passed to the object. If no initial value is provided, the constructor uses the standard constructor of the template type if applicable. If no standard constructor is applicable at compile time, the compilation fails.

```
7 public:
8         Observable( const std::string & name, const C & value = C()):
9                 value(value),
10                name(name)
11        {
12                this->reportChange();
13        }
```

After initiation, the constructor reports the new value to the wrapper. To initiate the member variable value, the template type must provide a copy operator, else instantiation will fail. Furthermore, note that the this-pointer in line 12 is required by the C++ ISO standard. Otherwise, the instantiation and usage of the member function cannot be guaranteed if a function with the same name is defined at global or namespace scope. More precisely, if the function call in line 12 was not qualified by the `this` pointer and a global function `reportChange()` is found in the lookup table, an ISO conform compiler links to the global function instead of initiating the member function of the template class. However, in this special case, not all compilers do behave according to the standard (Schneeweiß, 2012, p. 228).

By default, if no standard constructor and no copy operator are defined, a C++ compiler provides these operations. These standard constructor initialises all member variables by calling their standard constructor, and the copy operator of the compiler copies all member variables by calling their standard copy operator. Using these functions, the constant variable name is either initialised with an empty string or with the name of another observable. Both results are not desirable. Therefore, to preclude an accidental

use of these functions, they are declared as private member functions and remain without definition.

```
14 private:
15         Observable( );
16         Observable(const Observable & );
```

The declaration as private functions inhibits the definition of the default operators and leads to a compiler error, if the functions are called from outside of the class scope. Furthermore, an accidental function call inside the class scope leads to a linker error since the functions are not defined.

Assignment operator

The assignment operator enables the assignment of arbitrary values to the Observable class, which are then stored in the member variable value. After assignment, the new value is forwarded to the wrapper.

```
17 public:
18         Observable<C>& operator=(const C & value){
19                 if (this->value != value){
20                         this->value = value;
21                         this->reportChange();
22                 }
23                 return *this;
24         }
```

Conversion to a constant reference

The Observable is converted to a constant reference of the template type either by explicitly calling the member function `value()` or implicitly via the conversion function `operator const C &`. Both functions return a constant reference to the member variable value.

```
25         inline const C & value() const{
26                 return this->value;
27         }
28
29         inline operator const C&() const{
30                 return this->value;
31         }
```

Since constant references provide only reading access to their value and no assignment is possible, it is not necessary to report the conversion to a constant reference to the wrapper.

Conversion to a pointer to a mutable

The most difficult part of the implementation is the conversion to a mutable object. It is required to allow for function calls that require a pointer to the value of the observable as parameter. Thereby, the major challenge is to ensure that the wrapper is notified after the value that the pointer addresses, has been changed. This task is handled by the internal pointer classes. Whenever a mutable is required, the observable generates a pointer object which is then implicitly converged to the required pointer. At the end of its life-time, the deconstructer of the pointer object informs the wrapper.

```
32          class Pointer {
33                  Observable<C> & obs;
34          public:
35                  ~Pointer(){
36                          this->obs.reportChange();
37                  }
```

All constructors of the pointer class are declared as private functions and only one constructor, which requires a reference to the respective observable is defined. That means, a pointer object can only be generated by its member functions and by member functions of the observable class, which is declared as friend.

```
39          private:
40                  Pointer(Observable<C>& obs):
41                          obs(obs){};
42                  friend class Observable<C>;
43
44                  Pointer(const Pointer &);
45                  Pointer();
```

The conversion operator is required to implicitly convert the pointer object to the required pointer of the observable type. It returns a pointer to the value of the observable.

```
46          public:
47                  inline operator C*(){return &(this->obs.value);};
48
49          };
```

The pointer object is generated by the address operator & of the observable, which is usually called to return a pointer to the address of the object.

```
50
51          inline Pointer  operator&(){
52                  return Pointer(*this);
53          }
```

The member function `reportChange()` is called whenever the value of the Observable changes. It is responsible for sending the update information to the web-service wrapper via the `callbackProxy`. If no callback proxy exists, i. e., PANDAS is running in local mode, the function returns without doing anything. Else value, name and type as well as the simulation id are stored in the structure `message`, which is then used to call the

`reportVariableChange()` function of the callback proxy. The response variable reply is just a dummy variable that contains no information. The variable type is not stored as variable, but returned by the function `getTypename()`.

```
54          inline void reportChange(){
55                  if (callbackProxy == 0)
56                          return;
57                  _ns1__reportVariableChange message;
58                  {
59                          std::ostringstream ss;
60                          ss << ::simID;
61                          message.SimID = ss.str();
62                  }
63                  message.VariableType = this->getTypename();
64                  {
65                          std::ostringstream ss;
66                          ss << value;
67                          message.VariableValue = ss.str();
68                  }
69                  message.VariableName = name;
70
71                  __ns1__reportVaribaleChangeResponse reply;
72
73                  if(callbackProxy->reportVariableChange(&report, reply)){
74                          callbackProxy->soap_stream_fault(std::cerr);
75                  }
76          }
77
78          std::string getTypename() const;
79
80  }; // class observable
```

The function `getTypename()` must be declared and defined for all types that are used as Observable.

```
81  template <> std::string Observable<int>::getTypename() const;
82
83  template <> std::string Observable<std::string>::getTypename() const;
84
85  template <> std::string Observable<double>::getTypename() const;
```

The definition of the functions must not be located in the header file, but in an additional source file.

```
1   ///@file observable.cpp
2   template <> std::string Observable<int>::getTypename() const{
3           return "int";
4   }
5
6   template <> std::string Observable<std::string>::getTypename() const{
7           return "string";
8   }
9
10  template <> std::string Observable<double>::getTypename() const{
```

```
11          return "double";
12  }
```

C.1.3. Usage

The Observable class is designed to requires only minimal changes of the implementation code for its usage. In general, variables that are reported to the web-service wrapper are global or static variables that are available during the whole execution of the program. To define a variable as an Observable, it is usually sufficient to change only the variable declaration.

```
1  ///@file usage.cpp
2  // int subject(0);
3  webservice::Observable<int>   subject("test",0);
```

Functions that use the Observable as constant or pointer can remain unchanged. However, note that functions that require a mutable reference variable are not implemented in PANDAS, and therefore, their usage is not yet supported.

```
4  void f(int* i)
5  {
6          *i = 42;
7  }
8
9  void g(const int * i)
10 {
11         std::cout<<*i<<std::endl;
12 }
13
14 void h(const int & i)
15 {
16         std::cout<<i<<std::endl;
17 }
```

The functions `f(int* i)` and `g(const int* i)` have a pointer as parameter. If they are called, the address operator returns a pointer object, which is implicitly converted to a pointer to the value of the observable. When the functions return, the pointer object reaches the end of its scope, and the destructor passes the changes to the web-service wrapper.

```
18 void test_subject()
19 {
20         g(&subject);
21         f(&subject);
```

However, the destructor always informs the web-service wrapper also if the value is not changed at all. Therefore, to speed up execution, calling the member function `value()` is recommended, when a pointer to a constant is required. This avoids an unnecessary call of `reportChange()`

```
22          g(&subject.value());
```

When the observable is assigned to a variable of the observable type, it is implicitly converted to a constant reference. Therefore, it is not necessary to change functions that are called by value or need a constant reference as parameter.

```
23          int test = subject;
24          h(subject);
```

Furthermore, when a constant value is assigned to the Observable, the assignment operator is called, which automatically informs the wrapper.

```
25          subject = 14;
```

Attention must be paid when the Observable is assigned to a pointer. In this case, the pointer object is destroyed after the assignment operator returns. Therefore, assignments to the pointer change the value of the Observable and are not reported to web-service wrapper automatically, but require an explicit call of `reportChange()`;

```
26          int * pointer = &subject;//Pointer object is generated
27          //Pointer object is destroyed and calls reportChange()
28          pointer* = 33;
29          f(pointer);
30          subject.reportChange();
31  }
```

Bibliography

Acartürk, A.: *Simulation of charged hydrated porous materials*. Dissertation, Report No. II-18 of the Institute of Applied Mechanics (CE), University of Stuttgart 2009.

Adam, G.; Läuger, P. & Stark, G.: *Physikalische Chemie und Biophysik*, 5th Edition. Springer Dordrecht 2009.

Alberts, B.; Johnson, A.; Lawis, J.; Raff, M.; Roberts, K. & Walter, P.: *Molecular biology of the cell*,4th Edition. Garland Science, New York 2002.

Ambrosi, D. & Guana, F.: Stress-modulated growth. *Mathematics and Mechanics of Solids* **12** (2007), 319–342.

Ambrosi, D. & Guillou, A.: Growth and dissipation in biological tissues. *Continuum Mechanics and Thermodynamics* **19** (2007), 245–251.

Ambrosi, D. & Mollica, F.: On the mechanics of a growing tumor. *International Journal of Engineering Science* **40** (2002), 1297–1396.

Ambrosi, D. & Mollica, F.: The role of stress in growth of multicell spheroid. *Journal of Mathematical Biology* **48** (2004), 477–499.

Ambrosi, L. & Preziosi, L.: On the closure of mass balance models for tumor growth. *Mahematical Models and Methods in Applied Sciences* **12** (2002), 737–754.

Atkins, P. & de Paula, J.: *Physical Chemistry*, 8th Edition. Oxford University Press 2006.

Baehr, H. D. & Kabelac, S.: *Thermodynamik: Grundlagen und technische Anwendungen*, 14th Edition. Springer-Verlag, Berlin Heidelberg 2012.

Beaupré, G. S.; Orr, T. E. & Carter, D. R.: An approach for time-dependent bone modeling and remodeling – Theoretical development. *Journal of Orthopaedic Research* **8** (1990), 651–661.

Blaxter, K.: *Energy metabolism in animals and man*. Cambridge University Press, Cambridge 1989.

Blome, P.: *Ein Mehrphasen-Stoffmodell für Böden mit Übergang auf Interface-Gesetze*. Dissertation, Bericht Nr. II-10 aus dem Institut für Mechanik (Bauwesen), Universität Stuttgart 2003.

de Boer, R. & Ehlers, W.: *Theorie der Mehrkomponentenkontinua mit Anwendung auf bodenmechanische Probleme*. Forschungsberichte aus dem Fachbereich Bauwesen, Heft 47, Universität-GH-Essen 1986.

de Boer, R. & Ehlers, W.: The development of the concept of effective stresses. *Acta mechanica* **83** (1990), 77–92.

Bowen, R. M.: Toward a thermodynamics and mechanics of mixtures. *Archive for Rational Mechanics and Analysis* **24** (1967), 370–403.

Bowen, R. M.: Theory of mixtures. In *Continuum Physics*, Vol. III, Eringen, A. C. (ed.), Academic Press, New York 1976, pp. 1–127.

Bowen, R. M.: Incompressible porous media models by use of the theory of mixtures. *International Journal of Engineering Science* **18** (1980), 1129–1148.

Bowen, R. M.: Compressible porous media models by use of the theory of mixtures. *International Journal of Engineering Science* **20** (1982), 697–735.

Braess, D.: *Finite Elemente*, 2nd Edition. Springer-Verlag, Berlin 1997.

Brezzi, F. & Fortin, M.: *Mixed and Hybrid Finite Element Methods*. Springer-Verlag, New York 1991.

Byrne, H.: Modelling avascular tumour growth. In *Cancer Modelling and Simulation*, Preziosi, L. (ed.), Chapman and Hall/CRC, Boca Raton 2003.

Byrne, H. & Preziosi, L.: Modelling solid tumour growth using the theory of mixtures. *Mathematical Medicine and Biology* **20** (2003), 341–366.

Carter, D. R. & Hayes, W. C.: The compressive behavior of bone as a two-phase porous structure. *The Journal of Bone and Joint Surgery* **59** (1977), 954–962.

Coleman, B. & Noll, W.: The thermodynamics of elastic materials with heat conduction and viscosity. *Archive for Rational Mechanics and Analysis* **13** (1963), 167–178.

Cowin, S. C.: How is a tissue built? *Journal of Biomechanical Engineering* **122** (2000), 553–569.

Cowin, S. C. & Hegedus, D. H.: Bone remodeling I: theory of adaptive elasticity. *Journal of Elasticity* **6** (1976), 313–326.

DeRemer, F. & Kron, H. H.: Programming-in-the-large versus programming-in-the-small. *IEEE Transactions on Software Engineering* **SE-2** (1976), 80–86.

Diebels, S.; Ellsiepen, P. & Ehlers, W.: Error controlled Runge-Kutta time integration of a viscoplastic hybrid two-phase model. *Technische Mechanik* **19** (1999), 19–27.

Ehlers, W.: *Poröse Medien – ein kontinuumsmechanisches Modell auf der Basis der Mischungstheorie*. Bericht Nr. II-22 aus dem Institut für Mechanik (Bauwesen), Stuttgart 2012, Nachdruck der Habilitationsschrift aus dem Jahr 1989 (Forschungsberichte aus dem Fachbereich Bauwesen der Universität-GH-Essen **47**, Essen 1989).

Ehlers, W.: Grundlegende Konzepte in der Theorie Poröser Medien. *Technische Mechanik* **16** (1996), 63–76.

Ehlers, W.: Foundations of multiphasic and porous materials. In *Porous Media: Theory, Experiments and Numerical Applications*, Ehlers, W. & Bluhm, J., eds., Springer-Verlag, Berlin 2002, pp. 3–86.

Ehlers, W.: Challenges of porous media models in geo- and biomechanical engineering including electro-chemically active polymers and gels. *International Journal of Advances in Engineering Sciences and Applied Mathematics* **1** (2009), 1–24.

Ehlers, W.; Diebels, S.; Mahnkopf, D. & Ellsiepen, P.: *Theoretische und numerische Studien zur Lösung von Rand- und Anfangswertproblemen in der Theorie Poröser Medien.* Forschungsbericht zum DFG-Projekt Eh 107/6-2, Bericht Nr. II-96-1 aus dem Institut für Mechanik (Bauwesen), Universität Stuttgart 1996.

Ehlers, W. & Ellsiepen, P.: Theoretical and numerical methods in environmental continuum mechanics based on the theory of porous media. In *Environmental Geomechanics*, Schreflor, B. A., ed., Springer-Verlag, Wien 2001, CISM Courses and Lectures No. 417, pp. 1–81.

Ehlers, W.; Markert, B. & Röhrle, O.: Computational continuum biomechanics with application to swelling media and growth phenomena. *GAMM–Mitteilungen* **32** (2009), 135–156.

Eipper, G.: *Theorie und Numerik finite elastischer Deformationen in fluidgesätigten porösen Medien.* Dissertation, Bericht Nr. II-1 aus dem Institut für Mechanik (Bauwesen), Universität Stuttgart 1998.

Ellsiepen, P.: *Zeit- und ortsadaptive Verfahren angewandt auf Mehrphasenprobleme pröser Medien.* Dissertation, Bericht Nr. II-3 aus dem Institut für Mechanik (Bauwesen), Universität Stuttgart 1999.

Erl, T.: *SOA design patterns.* Prentice Hall, Upper Saddle River 2009.

Frost, H. M.: Tetracycline-based histological analysis of bone remodeling. *Calcified Tissue Research* **3** (1969), 211–237.

Graf, T.: *Multiphasic Flow Processes in Deformable Porous Media under Consideration of Fluid Phase Transitions.* Dissertation, Report No. II-17 of the Institut of Applied Mechanics (CE), University of Stuttgart 2008.

Görlach, K.; Sonntag, M.; Karastoyanova, D.; Leymann, F. & Reiter, M.: Conventional workflow technology for scientific simulation. In *Guide to e-Science*, Yang, X.; Wang, L. & Jie, W. (eds.), Springer, London 2011, chap. 12, pp. 323–352.

Hazelwood, S. J.; Martin, R. B.; Rashid, M. M. & Rodrigo, J. J.: A mechanistic model for internal bone remodeling exhibits different dynamic responses in disuse and overload. *Journal of Biomechanics* **34** (2001), 299–308.

Hert, J.; Lisková, M. & Landa, J.: Reaction of bone to mechanical stimuli. 1. continuous and intermittent loading of tibia in rabbit. *Folia Morphologica* **19** (1971), 290–300.

Humphrey, J. D.: Continuum biomechanics of soft biological tissues. *Proceedings of the Royal Society of London A* **459** (2003), 3–46.

Humphrey, J. D. & Rajagopal, K. R.: A constrained mixture model for growth and remodeling of soft tissues. *Mahematical Models and Methods in Applied Sciences* **12** (2002), 407–430.

Junqueira, L. C. U. & Carneiro, J.: *Histologie*, 6th Edition. Springer Medizin-Verlag, Heidelberg 2005.

Karajan, N.: *An Extended Biphasic Description of the Inhomogeneous and Anisotropic Intervertebral Disc*. Dissertation, Report No. II-19 of the Institut of Applied Mechanics (CE), University of Stuttgart 2009.

Klotz, I. M. & Rosenberg, R. M.: *Chemical Thermodynamics*, 6th Edition. John Wiley & Sons, New York 2000.

Komarova, S. V.; Smith, R. J.; Dixon, S. J.; Sims, S. M. & Wahl, L. M.: Mathematical model predicts a critical role for osteoclast autocrine regulation in the control of bone remodeling. *Bone* **33** (2003), 206 – 215, ISSN 8756-3282.

Krause, R.: *Kontinuumsmechanische Beschreibung von avaskulären Tumoren*. Diplomarbeit, Universität Stuttgart (2008).

Krstin, N.; Nackenhorst, U. & Lammering, R.: Zur konstitutiven Beschreibung des anisotropen, beanspruchungsadaptiven Knochenumbaus. *Technische Mechanik* **20** (2000), 31–40.

Kuhl, E. & Steinmann, P.: Mass- and volume-specific views on thermodynamics for open systems. *Proceedings of the Royal Society A* **459** (2003), 2547–2568.

Lanir, Y.: Biorheology and fluid flux in swelling tissue. I. Bicomponent theory for small deformations, including concentration effects. *Biorheology* **24** (1987), 173–187.

Lanyon, L. & Rubin, C.: Static vs dynamic loads as an influence on bone remodelling. *Journal of Biomechanics* **17** (1984), 897–905.

LeBlanc, A.; Schneider, V.; Shackelford, L.; West, S.; Oganov, V.; Bakulin, A. & Voronin, L.: Bone mineral and lean tissue loss after long duration space flight. *Journal of Musculoskeletal & Neuronal Interactions* **1** (2000), 157–160.

Lemaire, V.; Tobin, F. L.; Greller, L. D.; Cho, C. & Suva, L. J.: Modeling the interactions between osteoblast and osteoclast activities in bone remodeling. *Journal of Theoretical Biology* **229** (2004), 293 – 309.

Leymann, F. & Roller, D.: *Production Workflow: Concepts and Techniques*. Prentice Hall, Englewood Cliffs 1999.

Lisková, M. & Hert, J.: Reaction of bone to mechanical stimuli. 2. periosteal and endosteal reaction of tibial diaphysis in rabbit to intermittent loading. *Folia Morphologica* **19** (1971), 301–317.

Löffler, G.: *Basiswissen Biochemie mit Pathobiochemie*, 7th Edition. Springer-Verlag, Berlin 2008.

Lutz, A. & Nackenhorst, U.: Numerical investigations on the biomechanical compatibility of hip-joint endoprosteses. *Archive of Applied Mechanics* **80** (2010), 503–512.

Mahnkopf, D.: *Lokalisierung fluidgesättigter poröser Festkörper bei finiten elastoplastischen Deformationen*. Dissertation, Bericht Nr. II-5 aus dem Institut für Mechanik (Bauwesen), Universität Stuttgart (2000).

Maldonado, S.; Borchers, S.; Findeisen, R. & Allgöwer, F.: Mathematical modeling and analysis of force induced bone growth. In *Engineering in Medicine and Biology Society. Proceedings of the 28th Annual International Conference of the IEEE*, 2006, pp. 3154–3157.

Maldonado, S.; Findeisen, R. & Allgöwer, F.: Phenomenolgical mathematical modeling and analysis of force-induced bone growth and adaptation. In *Proceedings of the FOSBE*, Stuttgart 2007, pp. 147–152.

Markert, B.: *Porous Media Viscoelasticity with Application to Polymeric Foams*. Dissertation, Report No. II-12 of the Institut of Applied Mechanics (CE), University of Stuttgart 2005.

Markert, B.: A constitutive approach to 3-d nonlinear fluid flow through finite deformable porous continua. *Transport in Porous Media* **70** (2007), 427–450.

Markert, B.: A biphasic continuum approach for viscoelastic high-porosity foams: Comprehensive theory, numerics, and application. *Archives of Computational Methods in Engineering* **15** (2008), 371–446.

Markert, B. & Ehlers, W.: Modeling and simulation of spheroidal tumor growth. In *Proceedings of the ECCOMAS Thematic Conference on Modelling of Heterogeneous Materials*, Bittnar, Z. & Mang, S. (eds.), Czech Technical University, Prague, Czech Republic 2007, pp. 24–25.

Mellon, S. J. & Tanner, K. E.: Bone and its adaptation to mechanical loading: a review. *International Materials Reviews* **57** (2012), 235–255.

Morlock, M.; Schneider, E.; Bluhm, A.; Vollmer, M.; Bergmann, G.; Müller, V. & Honl, M.: Duration and frequency of every day activities in total hip patients. *Journal of Biomechanics* **34** (2001), 873–881.

Müller, I.: *Thermodynamics*. Pitman, Boston 1985.

Nackenhorst, U.: Numerical simulation of stress stimulated bone remodeling. *Technische Mechanik* **17** (1997), 31–40.

Nyman, J. S.; Hazelwood, S. J.; Rodrigo, J. J.; Martin, R. B. & Yeh, O. C.: Long stemmed total knee arthroplasty with interlocking screws: A computational bone adaptation study. *Journal of Orthopaedic Research* **22** (2004a), 51–57.

Nyman, J. S.; Yeh, O. C.; Hazelwood, S. J. & Martin, R.: A theoretical analysis of long-term bisphosphonate effects on trabecular bone volume and microdamage. *Bone* **35** (2004b), 296 – 305.

Papazoglou, M. P.: *Web Services: Principles and Technology*. Prentice Hall, Harlow 2008.

Papazoglou, M. P. & Georgakopoulos, D.: Introduction: Service-oriented computing. *Communications of the ACM* **46** (2003), 24–28.

Peterson, M. C. & Riggs, M. M.: A physiologically based mathematical model of integrated calcium homeostasis and bone remodeling. *Bone* **46** (2010), 49–63.

Preziosi, L. & Tosin, A.: Multiphase modelling of tumour growth and extracellular matrix interaction: mathematical tools and applications. *Journal of Mathematical Biology* **58** (2009), 625–656.

Reimann, P.; Reiter, M.; Schwarz, H.; Karastoyanova, D. & Leymann, F.: SIMPL - A Framework for Accessing External Data in Simulation Workflows. In *Datenbanksysteme für Business, Technologie und Web (BTW 2011), 14. Fachtagung des GI-Fachbereichs „Datenbanken und Informationssysteme“(DBIS), Proceedings, 02.-04. März 2011, Kaiserslautern, Germany*, Gesellschaft für Informatik (GI), Lecture Notes in Informatics (LNI) 2011, Vol. 180 of *Series of the Gesellschaft für Informatik (GI)*, ISBN 978-3-88579-274-1, pp. 534–553.

Ricken, T. & Bluhm, J.: Evolutional growth and remodeling in multiphase living tissue. *Computational Materials Science* **45** (2009), 806–811.

Rubin, C. T. & Lanyon, L. E.: Regulation of bone formation by applied dynamic loads. *The Journal of Bone and Joint Surgery* **66** (1984), 397–402.

Rupp, T.; Karajan, N.; Ehlers, W. & Syn: Calculation of internal loads in the spine using a full human multi-body model: methodological approach towards the validation of fem boundary conditions. In *Proceedings of SimTech 2011: International Conference of Simulation Technology*, Stuttgart 2011.

Sambrook, P. & Cooper, C.: Osteoporosis. *The Lancet* **367** (2006), 2010–2018.

Schneeweiß, R.: *Moderne C++ Programmierung*. Xpert.press, Springer-Verlag Berlin 2012.

Schwachöfer, J. H. M.; Hoogenhout, J. & Kal, H. B.: Three-dimensional culture of human tumor cells under standardized medium conditions. *Cytotechnology* **5** (1991), 265–271.

Simo, J. C. & Taylor, R. L.: Consistent tangent operators for rate-independent elastoplasticity. *Computer Methods in Applied Mechanics and Engineering* **48** (1985), 101–118.

Steeb, H. & Diebels, S.: A thermodynamic-consistent model describing growth and remodeling phenomena. *Computational Materials Science* **28** (2003), 597–607.

Stroustrup, B.: *Die C++ Programmiersprache*, 4th Edition. Addison-Wesley, Munich 2000.

Taber, L. A.: Biomechanics of growth, remodeling, and morphogenesis. *Applied Mechanics Reviews* **48** (1995), 487–545.

Taylor, I.; Shields, M.; Deelman, E. & Gannon, D.: *Workflows for e-Science - Scientific Workflows for Grids*. Springer, London 2007.

Truesdell, C.: *Rational Thermodynamics*. McGraw-Hill, New York 1969.

Truesdell, C. & Toupin, R. A.: The classical field theories. In Flügge, S. (ed.) *Handbuch der Physik*, Vol III/1, Springer-Verlag, Berlin 1960.

Unnikrishnan, G. U.; Unnikrishnan, V. U.; Reddy, J. N. & Lim, C. T.: Review on the constitutive models of tumor tissue for computational analysis. *Applied Mechanics Reviews* **63** (2010), 040801.

Van Sint Jan, S.; Crudele, M.; Gashegu, J.; Feipel, V.; Poulet, P.; Salvia, P.; Hilal, I.; Sholukha, V.; Louryan, S. & Rooze, M.: Development of multimedia learning modules for teaching human anatomy: Application to osteology and functional anatomy. *The Anatomical Record Part B: The New Anatomist* **272B** (2003), 98–106.

Wang, X.; Erickson, A. M.; Allen, M. R.; Burr, D. B.; Martin, R. B. & Hazelwood, S. J.: Theoretical analysis of alendronate and risedronate effects on canine vertebral remodeling and microdamage. *Journal of Biomechanics* **42** (2009), 938–944.

Webster, D. & Müller, R.: In silico models of bone remodeling from macro to nano – from organ to cell. *Wiley Interdisciplinary Reviews: Systems Biology and Medicine* **3** (2011), 241–251.

Weerawarana, S.; Curbera, F.; Leymann, F.; Storey, T. & Ferguson, D. F.: *Web Services Platform Architecture: SOAP, WSDL, WS-Policy, WS-Addressing, WS-BPEL, WS-Reliable Messaging, and More*. Prentice Hall, Upper Saddle River 2005.

Weinans, H.; Huiskes, R. & Grootenboer, H. J.: Effects of fit and bonding characteristics of femoral stems on adaptive bone remodeling. *Journal of Biomechanical Engineering* **116** (1994), 393–400.

Wolff, J.: *Das Gesetz der Knochentransformation*. Hirschwald, Berlin 1892.

Zeppenfeld, K. & Finger, P.: *SOA und WebServices*. Informatik im Fokus, Springer, Dordrecht 2009.

Zienkiewicz, O. C. & Taylor, R. L.: *The Finite Element Method*, Vol. 1., 4th Edition McGraw-Hill Book Company, London 1989a.

Zienkiewicz, O. C. & Taylor, R. L.: *The Finite Element Method*, Vol. 2., 4th Edition McGraw-Hill Book Company, London 1989b.

Curriculum vitae

Personal data

Name	Robert Friedrich Krause
Date of birth	28 December 1983
Place of birth	Bietigheim-Bissingen (Germany)
Nationality	German

Employment

11/2008-10/2013	**Research associate**, *Institut of Applied Mechanics (CE)*, University of Stuttgart Reasearch project: Growth, modellierung and remodelling of biological tissue
10/2004-10/2008	**Undergraduate research assistant**, *Institute of Applied Mechanics (CE)*, University of Stuttgart

Education

since 11/2008	**University of Stuttgart**, *Stuttgart (Germany)*, Ph. D. student at the "Research Centre for Simulation Technology" Research project: Growth, Modelling and Remodelling of Biological Tissue
10/2003-10/2008	**University of Stuttgart**, *Stuttgart (Germany)*, Civil Engineering, (Dipl.-Ing.), major subject: modelling and simulation methods Title of diploma's thesis: Continuum mechanical description of avascular tumours
9/1990-7/2003	**Elementary and secondary school**, *Bietigheim-Bissingen (Germany)*, Allgemeine Hochschulreife (high school diploma)

Released report series:

II-1 Gernot Eipper: *Theorie und Numerik finiter elastischer Deformationen in fluidgesättigten porösen Festkörpern*, 1998.

II-2 Wolfram Volk: *Untersuchung des Lokalisierungsverhaltens mikropolarer poröser Medien mit Hilfe der Cosserat-Theorie*, 1999.

II-3 Peter Ellsiepen: *Zeit- und ortsadaptive Verfahren angewandt auf Mehrphasenprobleme poröser Medien*, 1999.

II-4 Stefan Diebels: *Mikropolare Zweiphasenmodelle: Formulierung auf der Basis der Theorie Poröser Medien*, 2000.

II-5 Dirk Mahnkopf: *Lokalisierung fluidgesättigter poröser Festkörper bei finiten elastoplastischen Deformationen*, 2000.

II-6 Heiner Müllerschön: *Spannungs-Verformungsverhalten granularer Materialien am Beispiel von Berliner Sand*, 2000.

II-7 Stefan Diebels (Ed.): *Zur Beschreibung komplexen Materialverhaltens: Beiträge anläßlich des 50. Geburtstages von Herrn Prof. Dr.-Ing. Wolfgang Ehlers*, 2001.

II-8 Jack Widjajakusuma: *Quantitative Prediction of Effective Material Parameters of Heterogeneous Materials*, 2002.

II-9 Alexander Droste: *Beschreibung und Anwendung eines elastisch-plastischen Materialmodells mit Schädigung für hochporöse Metallschäume*, 2002.

II-10 Peter Blome: *Ein Mehrphasen-Stoffmodell für Böden mit Übergang auf Interface-Gesetze*, 2003.

II-11 Martin Ammann: *Parallel Finite Element Simulations of Localization Phenomena in Porous Media*, 2005.

II-12 Bernd Markert: *Porous Media Viscoelasticity with Application to Polymeric Foams*, 2005.

II-13 Saeed Reza Ghadiani: *A Multiphasic Continuum Mechanical Model for Design Investigations of an Effusion-Cooled Rocket Thrust Chamber*, 2005.

II-14 Wolfgang Ehlers & Bernd Markert (Eds.): *Proceedings of the 1st GAMM Seminar on Continuum Biomechanics*, 2005.

II-15 Bernd Scholz: *Application of a Micropolar Model to the Localization Phenomena in Granular Materials: General Model, Sensitivity Analysis and Parameter Optimization*, 2007.

II-16 Wolfgang Ehlers & Nils Karajan (Eds.): *Proceedings of the 2nd GAMM Seminar on Continuum Biomechanics*, 2007.

II-17 Tobias Graf: *Multiphasic Flow Processes in Deformable Porous Media under Consideration of Fluid Phase Transitions*, 2008.

II-18 Ayhan Acartürk: *Simulation of Charged Hydrated Porous Materials*, 2009.

II-19 Nils Karajan: *An Extended Biphasic Description of the Inhomogeneous and Anisotropic Intervertebral Disc*, 2009.

II-20 Bernd Markert: *Weak and Strong – On Coupled Problems in Continuum Mechanics*, 2009.

II-21 Wolfgang Ehlers & Bernd Markert (Eds.): *Proceedings of the 3rd GAMM Seminar on Continuum Biomechanics*, 2012.

II-22 Wolfgang Ehlers: *Poröse Medien – ein kontinuumsmechanisches Modell auf Basis der Mischungstheorie*, 2012. Nachdruck der Habilitationsschrift aus dem Jahr 1989 (Forschungsberichte aus dem Fachbereich Bauwesen der Universität-GH-Essen **47**, Essen 1989)

II-23 Hans-Uwe Rempler: *Damage in multi-phasic Materials Computed with the Extended Finite-Element Method*, 2012.

II-24 Irina Komarova: *Carbon-Dioxide Storage in the Subsurface: A Fully Coupled Analysis of Transport Phenomena and Solid Deformation*, 2012.

II-25 Yousef Heider: *Saturated Porous Media Dynamics with Application to Earthquake Engineering*, 2012.

II-26 Okan Avci: *Coupled Deformation and Flow Processes of Partial Saturated Soil: Experiments, Model Validation and Numerical Investigations*, 2013.

II-27 Arndt Wagner: *Extended Modelling of the Multiphasic Human Brain Tissue with Application to Drug-Infusion Processes*, 2014.

II-28 Joffrey Mabuma: *Multi-Field Modelling of the Human Hip Joint*, 2014.

II-29 Robert Krause: *Growth, Modelling and Remodelling of Biological Tissue*, 2014.

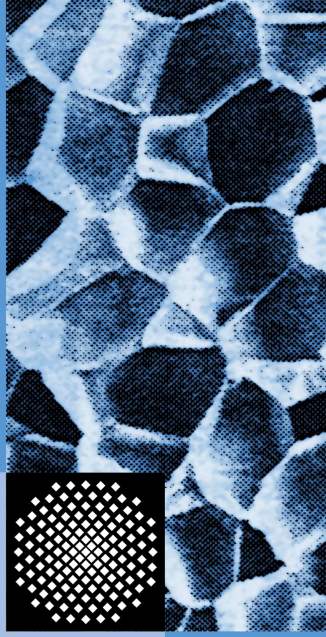

ISBN 978–3–937399–29–1
(D 93 – Dissertation, Universität Stuttgart)